



Universiteit
Leiden
The Netherlands

Cryo electron tomography studies of bacterial chemosensory arrays

Yang W.

Citation

Cryo electron tomography studies of bacterial chemosensory arrays. (2020, November 4).
Cryo electron tomography studies of bacterial chemosensory arrays. Retrieved from
<https://hdl.handle.net/1887/138131>

Version: Publisher's Version

License: [Licence agreement concerning inclusion of doctoral thesis in the Institutional Repository of the University of Leiden](#)

Downloaded from: <https://hdl.handle.net/1887/138131>

Note: To cite this publication please use the final published version (if applicable).

Cover Page



Universiteit Leiden



The handle <http://hdl.handle.net/1887/138131> holds various files of this Leiden University dissertation.

Author: Yang, W.

Title: Cryo electron tomography studies of bacterial chemosensory arrays

Issue Date: 2020-11-04

Cryo Electron Tomography Studies of Bacterial Chemosensory Arrays

PhD Thesis, Leiden University, 2020.

Cover design and layout by Wen Yang

Printed by Ridderprint | www.ridderprint.nl

Cryo Electron Tomography Studies of Bacterial Chemosensory Arrays

Proefschrift

ter verkrijging van

de graad van Doctor aan de Universiteit Leiden,
op gezag van Rector Magnificus prof. mr. C.J.J.M. Stolker,
volgens besluit van het College voor Promoties
te verdedigen op woensdag 4 November 2020
klokke 15.00 uur

door

Wen Yang

geboren te Fuzhou, China
in 1987

Promotiecommissie

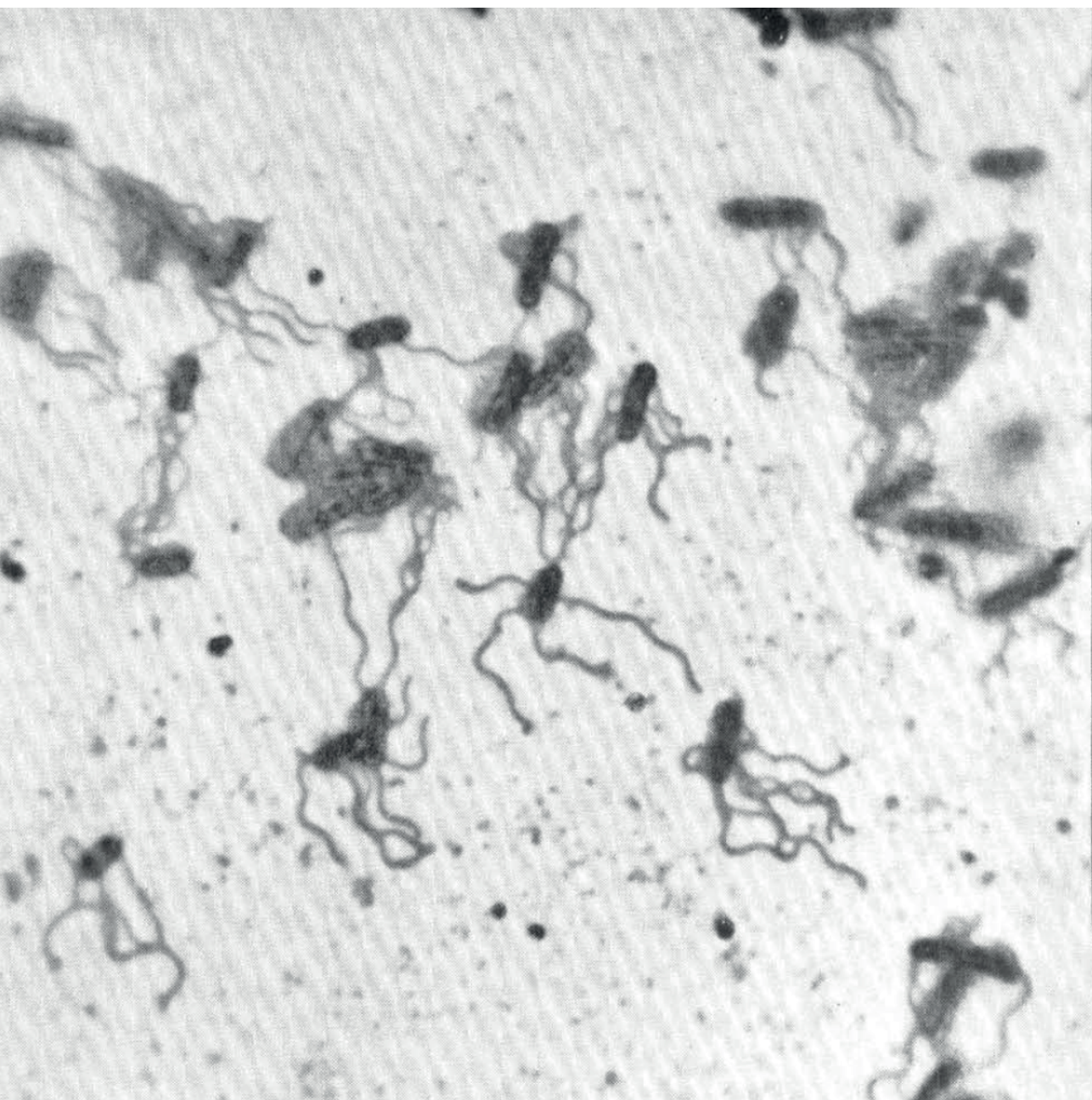
Promotoren: Prof. dr. A. Briegel
 Prof. dr. G. P. van Wezel

Overige leden: Prof. dr. A. H. Meijer
 Prof. dr. H. P. Spaink
 Prof. dr. T. S. Shimizu
 Dr. T. H. Sharp
 Dr. S. I. van Kasteren

Contents

Chapter 1	General Introduction	6
Chapter 2	Diversity of bacterial chemosensory arrays	16
Chapter 3	Baseplate variability of chemosensory arrays in <i>Vibrio cholerae</i>	32
Chapter 4	Kinase distribution in <i>Vibrio cholerae</i> F6 chemotaxis arrays	54
Chapter 5	<i>In situ</i> conformational changes of the <i>Escherichia coli</i> serine chemoreceptor in different signaling states	66
Chapter 6	Use cryo electron tomography to study the structure of chemoreceptor arrays <i>in situ</i>	88
Chapter 7	General Discussion	100
	Nederlandse Samenvatting	110
	References	114
	Curriculum Vitae	134
	Publications	135

CHAPTER 1



General Introduction

Across all domains of life, seeking favorable environmental conditions is a common behavior. Even the simplest life forms, such as motile bacteria, are capable of detecting the chemicals in their immediate surroundings. They are able to control their movement toward increasing concentrations of beneficial attractants and away from deleterious toxins. This behavior, termed bacterial chemotaxis, has been intensively studied ever since it was first reported back in the late 19th century (1). Chemotaxis was first observed in the organism *Escherichia coli* (*E. coli*). The cells formed visible bands in capillary tubes or rings on agar plates to follow a concentration gradient of nutrients and oxygen (2-4) (Fig. 1). This observation begged the question of how the cells are able to perform this behavior. Decades of extensive research on this topic made the chemotaxis system the best-understood signaling pathway in biology today.

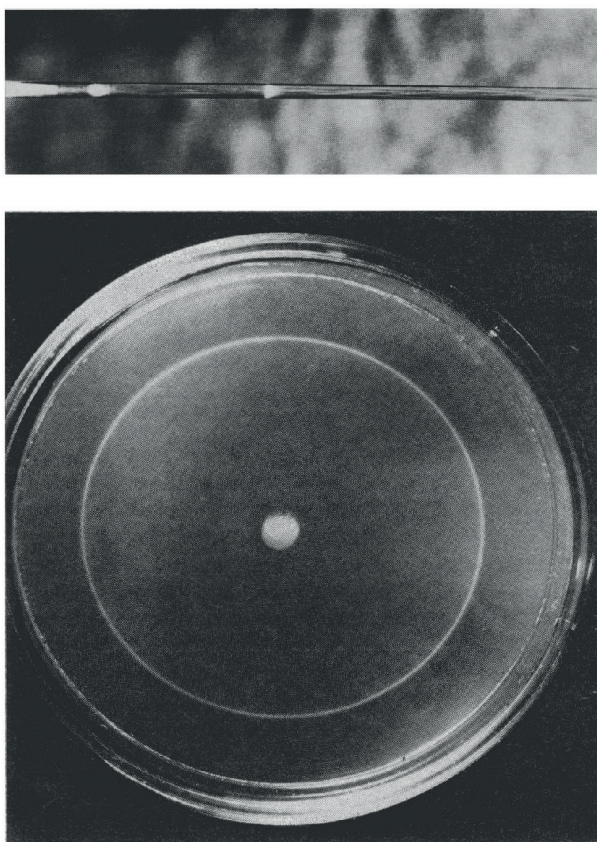


Figure 1. Chemotaxis behavior discovered in *E. coli*. Top panel shows a capillary tube filled with liquid medium. *E. coli* inoculated at the left end prorogate toward the right end and clustered into the bands shown in the capillary tube. Such clustering on a galactose agar plate with *E. coli* inoculated at the center develops as ring pattern shown in the bottom panel. Both pictures are taken from reference (2) .

Chemotaxis allows motile bacteria to modulate their swimming trajectory, which was documented in light microscopy studies in the '70s (5). The swimming trajectory of *E. coli* in an isotropic chemical environment is a random walk consisting of smooth swimming (termed "runs") and intervals (termed "tumbles") where the cells pause and change the direction of swimming. Such random walks can be readily biased by the presence of chemical gradients, in which case the runs lengthen and the tumbles become less frequent. Numerous studies over the past fifty years, gradually unraveled a sophisticated system that is capable of recognizing and responding to certain chemical compounds (6). Indeed, *E. coli* cells are necessarily equipped with complex macromolecular machinery specifically evolved for such a chemotaxis system to function. A detailed introduction to chemotaxis and the intricacies of the chemotaxis system can be found in **Chapter 2**.

In *E. coli*, the chemosensory pathway controls the flagella, which are long filaments that extend outside the cell. They are readily observed and their motor apparatus was first described in the early '70s (11) (Fig. 2A). Additional flagellar components, such as the hook and basal body complexes that anchor the flagellum to the cell wall envelope were also observed in purified samples (8, 9, 12) (Fig. 2B,C). Structural, biochemical and behavior studies collectively reveal that flagellar rotation is powered by a rotary motor (13-15). The 3D structural depiction of intact flagella motors was later achieved via single particle cryo-electron microscopy (cryo-EM) analysis (Fig. 2D) (10, 16, 17). Even today, the flagellar motor remains one of the most popular subjects for structural studies in cryo-EM (18-21).

In contrast, the sensing part of chemotaxis, which was believed to happen inside the cell, remained only accessible for probing through genetic and biochemical assays. The location and appearance of a chemosensory apparatus had remained elusive for a long time. In fact, the idea that a macromolecular machine underlies the chemotaxis system was not hypothesized until the '90s (22), after the polar clustering of chemotaxis proteins was first confirmed by immune electron microscopy in *E. coli* (23).

Despite the lack of direct structural information, the understanding of the molecular mechanism of chemosensory in *E. coli* progressed rapidly. The attractants and repellents that *E. coli* is capable of sensing in the environment were identified (24-26). Subsequently, mutant strains with chemotactic deficiency were used to identify the *che* (chemotaxis) genes and their respective Che proteins (27-29). Shortly after, the sensing capabilities of specific chemoreceptors, called methyl-accepting chemotaxis proteins (MCPs), were identified (6, 30, 31). The methylation state of the MCPs was then shown to provide a means for modulating the sensitivity towards the ligands, which is termed sensory adaptation, to keep a temporal record of ligand concentration (32-34). A decade later, phosphorylation of a messenger protein was identified as the signaling

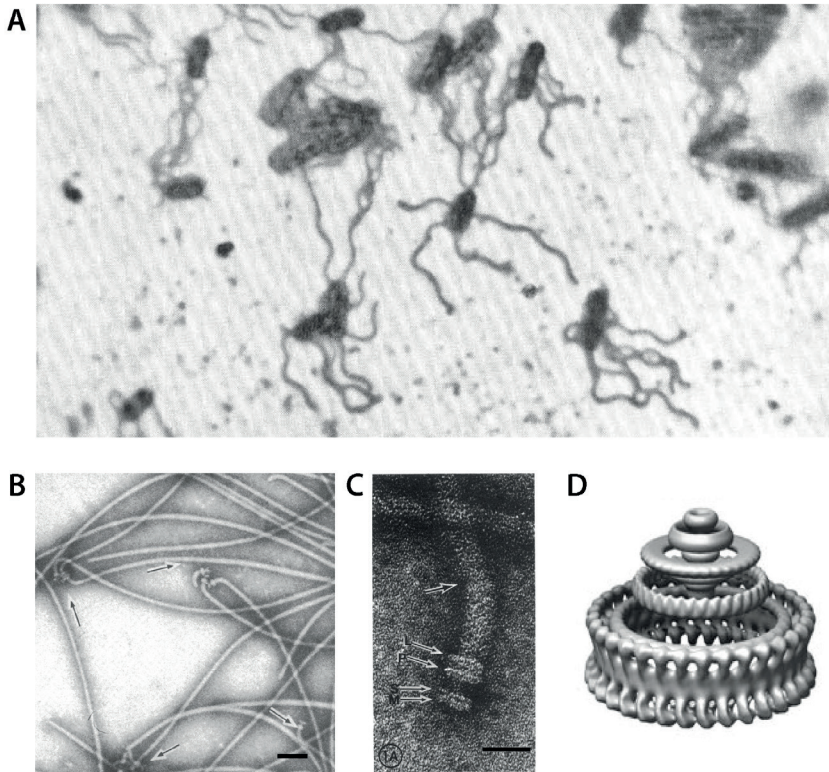


Figure 2. Bacterial flagellum and flagellar motors depicted through electron microscopy studies. (A) A negative stain image of *E. coli* cells. Image is adapted from (7). (B) A negative stain image of flagella purified from *E. coli*. Arrows point at hook-basal bodies. Scale bar is 100 nm. Image is adapted from (8). (C) A close-up negative stain image of the basal end of flagellum from *E. coli*. Arrows point to the location of rings. Scale bar is 30 nm. Panel is adapted from (9). (D) A 3D reconstruction of the isolated flagellar rotor from *Salmonella typhimurium* where the rings are resolved in detail. Image is adapted from (10).

mechanism that facilitates the communication between the chemoreceptors and the flagellar motor (35-38). In 1992, based on protein interaction studies *in vitro*, Gegner *et al.* proposed the initial model of the sensory apparatus which is a ternary protein complex consisting of MCPs, the histidine kinase CheA, and the adaptor protein CheW which physically couples the MCPs to CheA (39) (Fig. 3A). This model implied that the formation of a ternary protein complex is instrumental for proper chemotaxis.

Visualizing the chemosensory complex became necessary in order to understand the molecular mechanism underlying the system. Although it was clear where the chemotaxis proteins were located (cell poles) and what proteins comprise the system (ternary complex form by MCPs/CheW/CheA), few techniques allowed direct visualization of protein complexes inside living bacterial cells. Nevertheless, atomic-

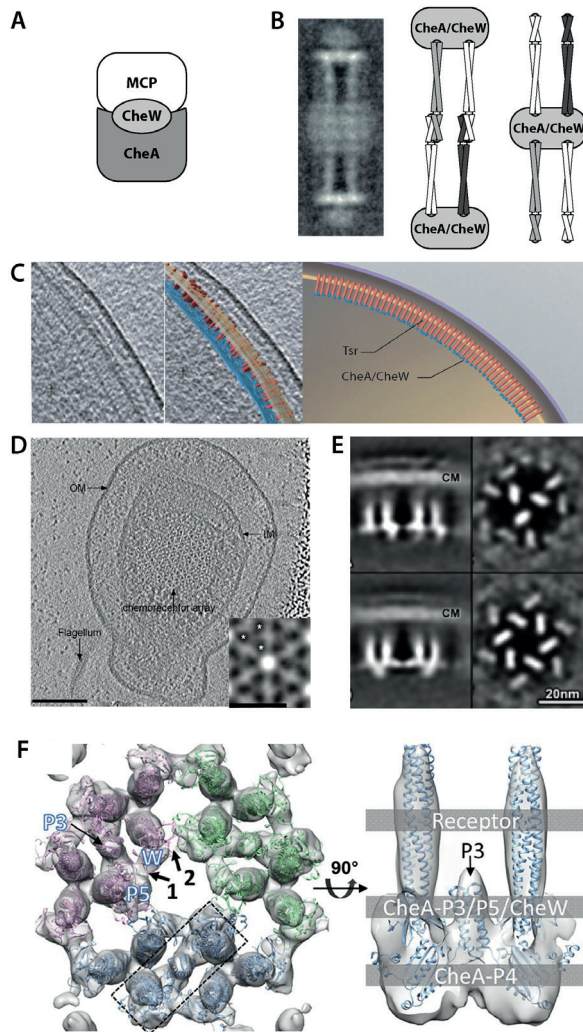


Figure 3. Models proposed for the ternary chemosensory complexes. (A) An early model proposed for receptor/CheW/CheA complex in chemotaxis pathway in reference (39). (B) Cryo-electron microscopy image of chemoreceptor-kinase complex and two different schemes describing potential molecular arrangements. Image modified from (40, 41). (C) Cryo-tomographic image of the cell pole of intact wild-type *E. coli* (left panel) and a segmented representation (middle panel) of the image, and a schematic representation of the arrays structure (right panel). Images are adapted from (42). (D) A tomographic slice of a *Salmonella enterica* minicell showing the native order of the chemoreceptor arrays in the top-view (Scale bar is 100 nm), and an inset shows the subtomogram average of the arrays (Scale bar is 12 nm). Images are adapted from (43). (E) Side-view (left column) and the top-view (right column) of subtomogram averaging results of two different kinase CheA arrangements (one in each row) of the chemosensory arrays in *E. coli*. Images are adapted from (44). (F) Density map (translucent gray) with molecular models fit within the density, with three core signaling complexes colored differently. Images are adapted from (45).

1
level structural information of the individual chemotaxis proteins gradually became available by X-ray crystallography (46-48). In the meanwhile, a significant amount of effort was invested into visualizing the recombinant protein complexes *in vitro* through cryo-EM (40, 41, 49). Due to limited image quality and means for analysis, the molecular architecture of the complex remained largely unknown. In fact, almost completely opposing interpretations could be derived from the same *in vitro* preparation of the ternary complex (Fig. 3B) (40, 41, 49).

The molecular arrangement of the chemosensory complex was eventually revealed by cryo-electron tomography (cryo-ET) (42, 50). This technique allows a three dimensional view of the chemosensory complexes *in vivo* preserved in a near-native state. The EM images revealed large patches of chemotaxis arrays at the cell poles. The receptors are oriented perpendicularly to the inner membrane. Their sensing domains were visible in the periplasmic space, while their other end in the cytoplasm is clearly associated with the CheA/CheW proteins that form a dense layer parallel to the inner membrane (Fig. 3C). With ever-improving resolution limits and image processing methods such as subtomogram averaging, both the hexagonal packing order of the receptors and the ordered arrangement of CheA and CheW underneath the chemoreceptor lattice were revealed (43, 44, 51, 52) (Fig. 3 D,E). Combined with atomic models from X-ray crystallography data, the molecular architecture of the chemotaxis arrays was finally solved for *E. coli*: Here, two receptor trimers-of-dimers, two monomeric CheWs, and one dimeric CheA form the signaling core unit that has also been shown to be the minimal structural unit for full modulation of CheA activity (45, 53) (Fig. 3F).

Cryo-ET provided crucial structural information for resolving the molecular architecture of chemosensory arrays. It has further provided insight to understanding the structure and function of the arrays (54). Studies of chemosensory systems in a wide variety of bacteria and archaea revealed a universal hexagonal packing order of the receptors (51, 55). Cryo-ET continues to provide new structural insights and continuously contributes to our understanding of the array assembly process and the conformational dynamics of both the receptors and the kinase CheA (54, 56-59). Cryo-ET has been an essential method to visualize this macromolecular machinery *in situ*. New developments in microscopy hardware and imaging processing software will produce even higher quality structural data and will continue to provide new insights into understanding the molecular mechanism of signal transduction and kinase activation in bacterial chemosensory (60).

Thesis outline

This thesis comprises several studies where I used cryo-ET to gain insight into the architecture and function of the chemosensory arrays. In **Chapter 2**, an in-depth review covers the basics of chemotaxis behavior, the chemotaxis signaling pathway, the chemotaxis proteins, and their arrangement in chemosensory arrays. Substantial emphasis is given to the fact that chemosensory arrays are an ingenious structure that manifests highly conservative structural features while simultaneously exhibiting a great tolerance for compositional diversity. Most strikingly, the chemoreceptors arrays observed thus far, even across far evolutionary distance, are hexagonally packed trimers-of-dimers with conserved lattice spacing. Still, great variability of chemosensory arrays exists in terms of the exact protein composition and stoichiometry, molecular architecture in the baseplate (where the receptors bind the kinase CheA and coupling proteins), the cellular localization, and the physiological relevance. More importantly, as prompted in this review, little is known about such diversified systems beyond the model organism *E. coli*, which has only one simplified chemotaxis pathway. Despite the wealth of information available today, several outstanding questions and challenges remain regarding the structure and function of the chemosensory arrays.

To gain insights into the architecture of chemosensory arrays in different bacteria, **Chapter 3** describes a study that reveals the compositional variability of chemosensory arrays in *Vibrio cholerae*. Arrays in *V. cholerae* have the potential to tailor their chemoreceptor composition in order to sense different targets. The chemotaxis proteins in the baseplate also exhibit a high degree of compositional variability, which potentially facilitates the incorporation of new receptors into the already existing chemosensory arrays. This high variability of chemosensory arrays is proposed for bacteria with a larger repertoire of chemoreceptors, more extensive auxiliary chemotaxis proteins, and multiple chemotaxis pathways. These attributes are distinctively divergent from the chemotaxis paradigm driven by studies in *E. coli*.

Aside from the compositional variability determined in **Chapter 3**, I further examined the molecular architecture of the chemosensory array baseplate in *V. cholerae* in **Chapter 4**. The hexagonal packing order of the receptor trimers-of-dimers are conserved among different species as reported previously, but the molecular composition and the architectural arrangement of chemotaxis protein in the baseplate is now considered species-specific. In *V. cholerae*, the histidine CheA exhibits an even distribution across the baseplate but without any distinctive order. Such a kinase distribution is expected to reduce the rigidity of the arrays and facilitate a more dynamic variability of chemoreceptors and baseplate components. It also raises intriguing questions about

how proper functionality of arrays and high cooperativity can be achieved when many of the receptor trimers-of-dimer units are not in direct contact with the kinase.

Chapter 5 presents a study carried out in the model organism *E. coli*. Here I explored the molecular mechanism of chemotaxis within chemosensory signaling core units, the minimal structural and functional repeats of the arrays. Through careful design and engineering, modified signaling core units are biased into either a kinase-on or kinase-off output state. The conformational dynamics of the serine chemoreceptors is visualized on a trimers-of-dimers level, and the corresponding conformational changes in CheA are observed. Such observations suggest that chemoreceptors achieve kinase control through changing its packing compactness of the receptor trimers-of-dimers. This result echoes several classic theories proposed for describing the signaling mechanism in chemoreceptors. The results further suggest why the trimers-of-dimers arrangement of the receptors may be necessary for carrying out its function in the chemosensory arrays.

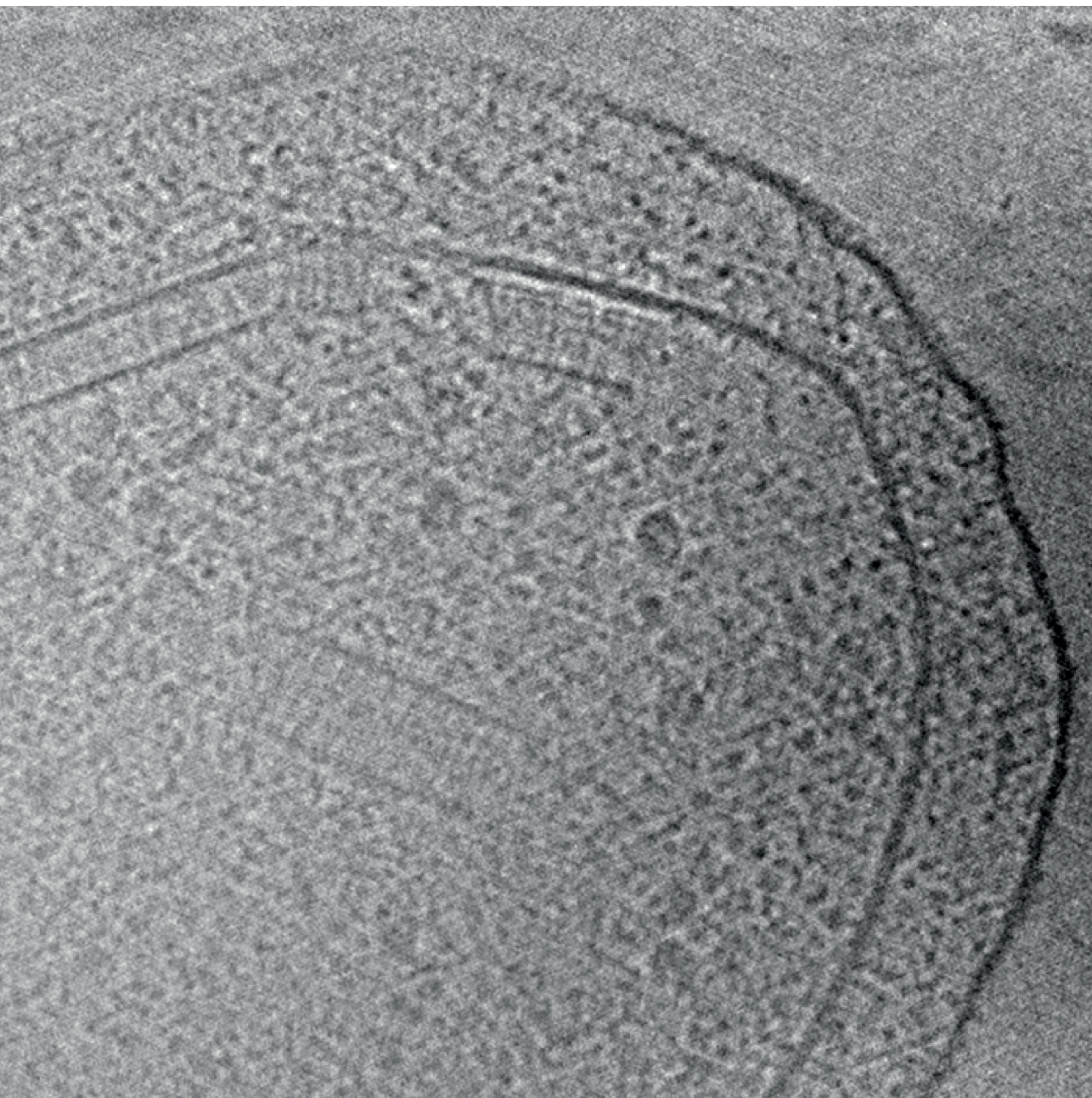
The chapters listed above are constructed with a focus on the scientific subject of this thesis, namely, the structural and functional studies of chemosensory arrays.

Chapter 6 shifts the focus to the primary scientific technique used throughout the studies included in this thesis, cryo-ET, which is currently the only method that permits high-resolution structural studies of extended arrays in its near-native condition. This chapter provides an overview of how to practice cryo-ET to visualize chemosensory arrays *in situ* using transmission electron microscopy in cryogenic conditions. A brief introduction of cryo-ET is included in this chapter, as well as a step-by-step description of the standard workflow including cryo specimen preparation; 2D tilt-series image acquisition, and 3D tomographic data reconstruction.

The key findings included in this thesis and their implications in a broader context are discussed in each chapter. **Chapter 7** discusses the cryo-ET technique. Particularly, the specific limitations of this technique when applied to studies of bacterial chemosensory arrays, and how improvements of this technique can lead towards an even better understanding of bacterial chemotaxis.

Overall, the studies presented in this thesis were made possible by recent technical advances in both hard- and software that increased data collection speed and achievable resolution of the cryo electron microscopy. This allowed me to achieve two major advances in our understanding of bacterial chemotaxis. While the arrangement of the chemoreceptors in highly ordered hexagonal arrays was already known, insight into the structural changes accompanying a change in receptor activation state inside the arrays had so far been lacking. Furthermore, the detailed architecture of array core components in species other than *E. coli* remained also unknown. In this thesis, I combined cryo-ET and subtomogram averaging methods to investigate the chemotaxis arrays both in the model system of *E. coli* as well as other, less well-understood systems such as *Vibrio cholerae*. This allowed me, for the first time, to determine conformational dynamics of the *E. coli* chemoreceptors correlated to the signaling states in situ. This study further gave insight on how the receptors function in a trimers-of-dimers packing arrangement. This discovery contributes to a fundamental understanding of why the hexagonal packing order is universal across all investigated species so far. Equally important for the chemotaxis field were the discovery of a different stoichiometry of chemotaxis proteins and a direct visualization of kinases in situ in a non-model organism. These new insights highlight that a structural diversity of chemoreceptor arrays does exist, and that is the norm and not an exception. This so far under-appreciated structural diversity in chemosensory arrays may be essential for adapting the chemotaxis system to the changing environments and may be essential for surviving a special niche or play a crucial role in pathogenicity.

CHAPTER 2



Diversity in bacteria chemosensory arrays

This chapter is published as:

Yang W¹, Briegel A¹ (2020) Trends in Microbiology 28(1):68-80.

1 Institute of Biology, Leiden University, Leiden, The Netherlands

Abstract

Chemotaxis is crucial to the survival of bacteria, and the signaling systems associated with it exhibit a high level of evolutionary conservation. The architecture of the chemosensory array and the signal transduction mechanisms have been extensively studied in *Escherichia coli*. More recent studies have revealed a vast diversity of the chemosensory system among bacteria. Unlike *E. coli*, some bacteria assemble more than one chemosensory array and respond to a broader spectrum of environmental and internal stimuli. These chemosensory arrays exhibit a great variability in terms of protein composition, cellular localization and functional variability. Here, we present recent findings that emphasize the extent of diversity in chemosensory arrays and highlight the importance of studying chemosensory arrays in bacteria other than the common model organisms.

Introduction

For a bacterium to move toward a more-favorable location, the cell must constantly sense its surroundings and respond to nutrient and repellent gradients. The ability of microbes to control their motility in response to their chemical environment is called chemotaxis (61). This behavior was first described, and is best understood, in the model organism *Escherichia coli* (2, 6, 62). *E. coli* possesses a single chemosensory pathway that consists of 11 proteins. Within this pathway, four different membrane-bound chemoreceptors (methyl-accepting chemotaxis proteins (MCPs)) and the redox receptor Aer bind directly to a histidine kinase CheA and a coupling protein CheW (also referred to as scaffolding protein or adaptor protein). Together, these proteins assemble into macromolecular complexes known as chemosensory arrays. Chemosensory arrays perceive environmental stimuli and collectively use them to control the phosphorylation level of receiver proteins (CheY and CheB), which mediate motor control and sensory adaptation, respectively (63). Because of their simplicity, chemosensory arrays in *E. coli* have long been the paradigm for understanding the molecular mechanisms of signaling transduction (63, 64) and the architecture of the arrays (43, 44).

Chemotaxis in *Escherichia coli*

Chemotaxis enables *E. coli* to migrate toward attractants and away from repellents. *E. coli* has multiple petrichous flagella powered by flagellar motors in the cytoplasm (65, 66). By default, the flagellar motors rotate counter-clockwise (CCW) and the left-handed helical filaments form a bundle that propels the cell in a more-or-less straight swim (run). When the flagellar motors switch their rotation direction from CCW to clockwise (CW), the flagellar bundle disassembles and the cell tumbles (13). In the presence of a stimulus, runs are lengthened and tumbles occur less frequently (Fig. 1A).

E. coli possesses a single chemotaxis pathway that consists of five different membrane-bound chemoreceptors and six cytoplasmic chemotaxis proteins (Fig. 1B) (61). Attractants and repellents bind to the ligand-binding domain of the MCPs either directly or via periplasmic binding proteins (67, 68). With the assistance of the coupling protein CheW, a stimulus is transmitted to the histidine kinase (CheA) (64). Upon a negative stimulus, such as repellents binding to the chemoreceptors, CheA autophosphorylates the response regulator CheY. Phosphorylated CheY (CheY-P) diffuses through the cytoplasm and binds to the flagellar motors to bias their rotation from the default CCW direction to CW, resulting in tumbling. CheY-P is quickly dephosphorylated by the phosphatase CheZ, which keeps the overall CheY-P level closely synchronized with the CheA activity. CheA also phosphorylates the methylesterase, CheB, to activate it.

Together with the methyltransferase CheR, CheB reversibly modifies the methylation state of the chemoreceptors in order to maintain an adapted sensitivity (63).

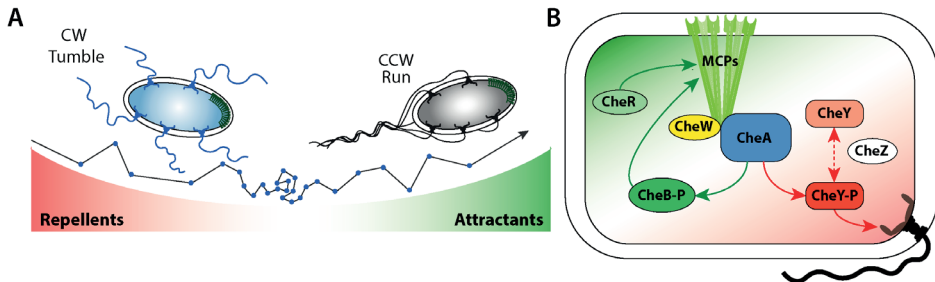


Figure 1. Chemotaxis and chemosensory pathway in *Escherichia coli*. (A) Chemotaxis enables *E. coli* to swim toward favorable environments through a combination of smooth runs when flagellar motors rotate counter-clockwise (black lines) and tumbles when flagellar motor rotate close wise (blue dots). The duration and frequency of the runs and tumbles are regulated by the chemosensory arrays (green patches of pillars at the cell poles) (13-15, 69). (B) Chemosensory pathway mediates both the flagellar motor control (red arrows) and the chemoreceptor sensory adaptation (green arrows).

Chemosensory array architecture in *E. coli*

The chemoreceptor homodimers readily form trimers-of-dimers through the interaction at their cytoplasmic tips (46). To form the signaling core units, receptor trimers bind both the kinase and coupling protein following a strict stoichiometry of 6 receptor trimers-of-dimers: 1 dimeric CheA: 2 monomeric CheWs (Fig. 2A) (46, 94-96). Among the five domains of the kinase CheA, the P5 domain directly binds to the receptor trimers (97-99). The P5 domain topologically resembles two tandem SH3 domains (47). Similarly, CheW is composed of two β -barrels sandwiching a hydrophobic core (100). CheW and P5 bind each other in an alternating order and form pseudo 6-fold symmetric rings that links core units together (Fig. 2B). Within the individual signaling core unit, CheW and P5 establish interface 1 (101); among the signaling core units, CheW and P5 form interface 2 which is crucial for forming the extended array lattice (92).

Through the networks of CheAs and CheWs, the receptor trimers-of-dimers are arranged into a rigid hexagonal pattern with a spacing of ~ 12 nm. This characteristic hexagonal packing order has become the hallmark for recognizing the arrays and for assessing the structural integrity of the array architecture (Fig. 2C)(51). In the side view, arrays are distinguishable as a continuous layer parallel to the inner membrane (Fig. 2D). The chemoreceptors can be seen as pillar-like densities that extend between the baseplate and the membrane. The side view reveals the length of the cytoplasmic fraction of the receptors that co-exist in the arrays and gives important insight into which receptors make up the specific array (51).

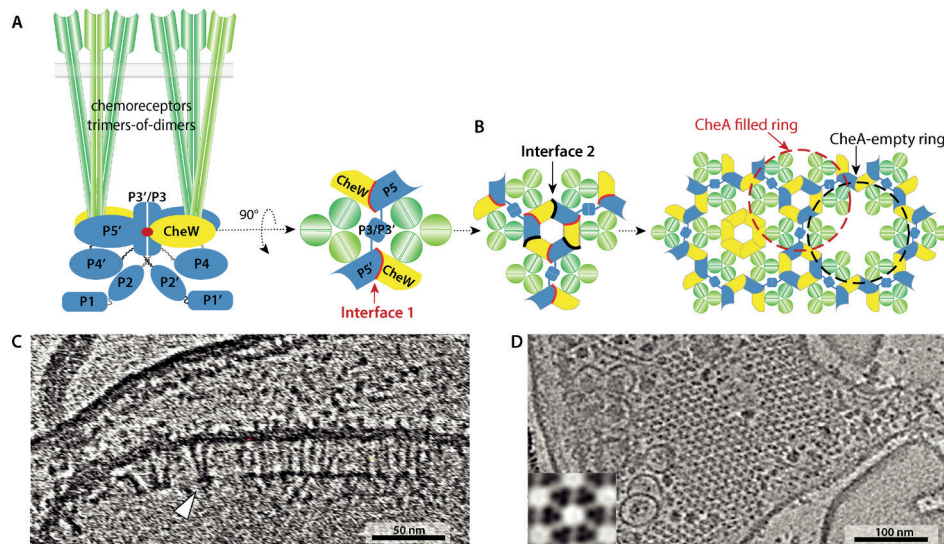


Figure 2. Architecture of chemosensory arrays in *E. coli*. (A) The side view and the top-down view of a signaling core unit is depicted in cartoon. The interface 1 within the core unit is marked with a red line. (B) Repeats of the signaling core units assemble into arrays through interface 2 marked in black lines. Red and black circles in dash lines show CheA filled and CheA-empty rings in baseplate, respectively. (C) Tomographic image of the chemosensory arrays in the side view near a flagellar motor in a lysed *E. coli* cell. The picture is modified from (102). (D) Cryo-electron tomography (cryo-ET) image of chemosensory arrays in the top view in a lysed *E. coli* cell. The insert panel shows subtomogram averaging of the hexagonally packed receptor trimers-of-dimers. The picture is adapted from (58).

Beyond the bacterial chemotaxis paradigm

More than half of all motile bacteria have multiple chemotaxis systems (70). In those bacteria, it appears that at least one chemotaxis pathway is dedicated to the control of the flagella, whereas other chemotaxis pathways may be involved in the regulation of a wide range of programmed cellular events (71). In the past decade, the field of chemotaxis research has broadened its focus to include bacterial species with more-complex chemotaxis systems. These studies have given insight into, among other things, the role of chemotaxis in the infectivity of pathogenic bacteria (71-78). Additionally, we have gained new insights into the adaptability of chemosensory arrays. Bacteria that experience stress conditions and/or transition to a sessile lifestyle remodel their chemotaxis arrays. For example, the expression of specific chemoreceptors are up-regulated in order to respond appropriately to new metabolic needs and environmental conditions (79-83). Moreover, the chemotaxis system in the archaea likely originated via horizontal gene transfer from bacteria and then further adapted to form a unique system that controls the archaellum (55). These studies highlight the great diversity of

chemotaxis systems and the role of chemosensory arrays beyond the paradigm found in *E. coli* (84, 85). However, the physiological relevance of many chemotaxis pathways that diverge from the *E. coli* system remains unclear.

The signaling mechanism of chemosensory arrays in *E. coli* has been described in great detail (61, 63, 64). In this review, we focus on novel aspects of chemosensory arrays that have recently been discovered. There is a great diversity in composition and cellular localization among prokaryotic chemosensory arrays. The co-existence of multiple arrays within a single species raises new questions about the possibility of crosstalk between chemotaxis systems and about how these systems are structurally and functionally separated at the level of chemosensory arrays. We will first describe our current understanding of the array architecture in *E. coli*, followed by an overview of the variability of chemosensory arrays among prokaryotes. We highlight the capability of array structures to tolerate compositional variability and speculate that this ability may facilitate quick adaptation to a broad repertoire of sensory inputs.

Chemosensory arrays appear structurally similar despite diverse composition

E. coli has a single chemotaxis pathway with five chemoreceptors that collectively sense the environment and control cellular motility. An “average” bacterial genome contains 14 chemoreceptor genes (86), but this number is highly variable and not proportional to the genome size. Bacteria that periodically encounter stress conditions or need to adapt to multiple or changing ecological niches tend to possess more receptor genes (85). For instance, *Magnetospirillum magnetotacticum*, which is capable of magnetotaxis, has 59 different MCPs (87, 88). A large structural and functional diversity exists among MCPs, especially in the ligand-binding domains that are responsible for sensing attractants and repellents (Fig. 3A). Genomic analysis of known MCP sequences predicts nearly one hundred distinct types of ligand-binding domains that provide an extremely broad sensory spectrum (Fig. 3B) (89, 90). The cytoplasmic signaling domains of the chemoreceptors are less diverse. Based on the number and organization of the seven-residue heptad repeats in the signaling domain, seven different major classes can be distinguished for MCPs (Fig. 3C)(91).

Many bacteria also possess additional cytoplasmic chemotaxis proteins that do not have counterparts in *E. coli*. These bring extra functional complexity to the signaling pathways. Furthermore, more than half of motile bacteria have several chemotaxis gene clusters in their genome, presumably representing separate chemotaxis systems. Based on a classification using a systems-level phylogenomics approach, 19 distinctive chemotaxis systems are currently characterized (70).

Despite the compositional diversity of arrays discussed above, a hexagonal packing order of chemoreceptors in the chemosensory array is conserved across all chemotactic prokaryotes examined thus far (51, 55). These analyses strongly suggest that the chemosensory array is an evolutionarily optimized structure with unique advantages to facilitate the cellular responses. The array serves as a platform to accommodate inputs from a variety of receptors simultaneously that ensures effective communication with the cytoplasmic components of the chemotaxis pathway. Furthermore, the conserved array architecture is thought to provide the structural basis for chemotactic cooperativity and signal amplification via allosteric interactions within the arrays (92, 93).

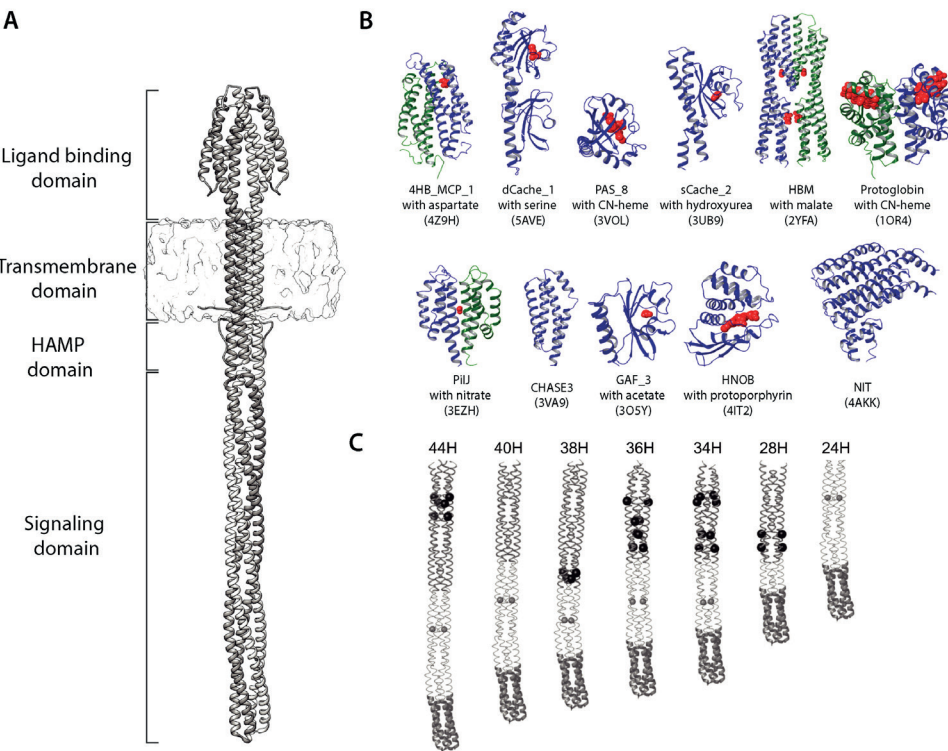


Figure 3. Structural diversity of chemoreceptors. (A) Model of the homodimer of Tsr serine receptor in *E. coli* with different functional modules marked. (B) The structural diversity of the ligand-binding domains. Ligands are colored in red. Ligand-binding domains known to be dimeric are depicted in green and blue for the different chains. Panel B is adapted from (89) with permission. (C) Models of different signaling domain classes. Within the signaling domain, the sensory adaptation subdomain, flexible bundle subdomain and the hairpin sub domain are colored in light gray, white and dark gray, respectively. Methylation sites are highlighted with black spheres to show the different patterns of methylation for chemoreceptor classes displaying different heptad numbers. Gray spheres show the conserved glycine residues located in the center of flexible bundle. Figure is adapted from (91).

Alternative architectures of array assembly

The molecular arrangement of the chemosensory arrays is best understood in *E. coli* [9,10]. Assembly of chemosensory arrays depends on the stringent regulation of the stoichiometric ratio of receptors, kinases and coupling proteins. Overexpression of one component can lead to the formation of alternative protein complexes (58). For example, when there are no baseplate components present, the cytoplasmic tips of the receptors trimers can associate with each other and result in “zipper,” or micelle-like structures (Fig. 4A-B). Together with the coupling protein and kinase, truncated chemoreceptors lacking transmembrane regions are capable of forming an array “sandwich” *in vitro* in the presence of crowding agents (Fig. 4C)(58, 103).

This “sandwich” structure is very similar to the entirely cytosolic chemosensory arrays observed in *Vibrio cholerae*, *Rhodobacter sphaeroides* and the archaeon *Methanoregula formicica* (55, 105). Approximately 14% of all chemoreceptors are predicted to be cytoplasmic (106). The native structure of cytoplasmic arrays observed so far show that two hexagonal lattices of receptor trimers-of-dimers interact head-to-head and sandwich between two CheA : CheW baseplates (Fig. 4D). The cytoplasmic arrays in *V. cholerae* display significant rigidity and are nearly flat, unlike membrane-bound arrays that follow the curvature of the inner membrane, or the flexible cytoplasmic arrays found in *R. sphaeroides* and *M. formicica*. This rigidity is likely due to the presence of the protein DosM that connects the baseplates to stabilize the arrays (104).

Multiple coupling proteins can coexist in the baseplate

As stated previously, chemotaxis proteins, including components that are directly integrated into the chemosensory arrays, exhibit a great diversity among bacteria (107). In addition to CheW, the protein CheV is encoded in 60% of all chemotactic prokaryotes (70). CheV is a chimeric protein consisting of a CheW-like adaptor domain and CheY-like response regulator domain. CheV can integrate into the baseplate and interact directly with receptors and CheA (108). Additionally, CheV can be phosphorylated by CheA, a process that is necessary for sensory adaption in *Bacillus subtilis* (109). A recent study reveals that genomes that contain CheV typically encode about four times more MCPs than genomes without CheVs (110). CheV has been proposed to co-evolve with a subpopulation of MCPs in order to preserve the protein interaction interfaces that are crucial for the incorporation and function of these MCPs in the arrays. This hypothesis was experimentally confirmed in *Campylobacter jejuni* (111).

In *V. cholerae*, the protein ParP also integrates into the baseplate to promote array formation and localization (Fig. 5A)(112). ParP contains a SH3-like domain with a similar topological architecture as the P5 domain of CheA and CheW, which enables it to integrate into the baseplate. In addition to promoting array formation, ParP also

facilitates array localization near the flagellar pole with the assistance of the ParC protein (113). This control of array positioning may allow a tighter control of the single polar motor of *V. cholerae*, which may be particularly important for bacteria that rely on a highly localized population of CheY molecules for chemotaxis (114). Therefore, certain components of the baseplate can actively regulate array positioning in addition to being part of the baseplate scaffold.

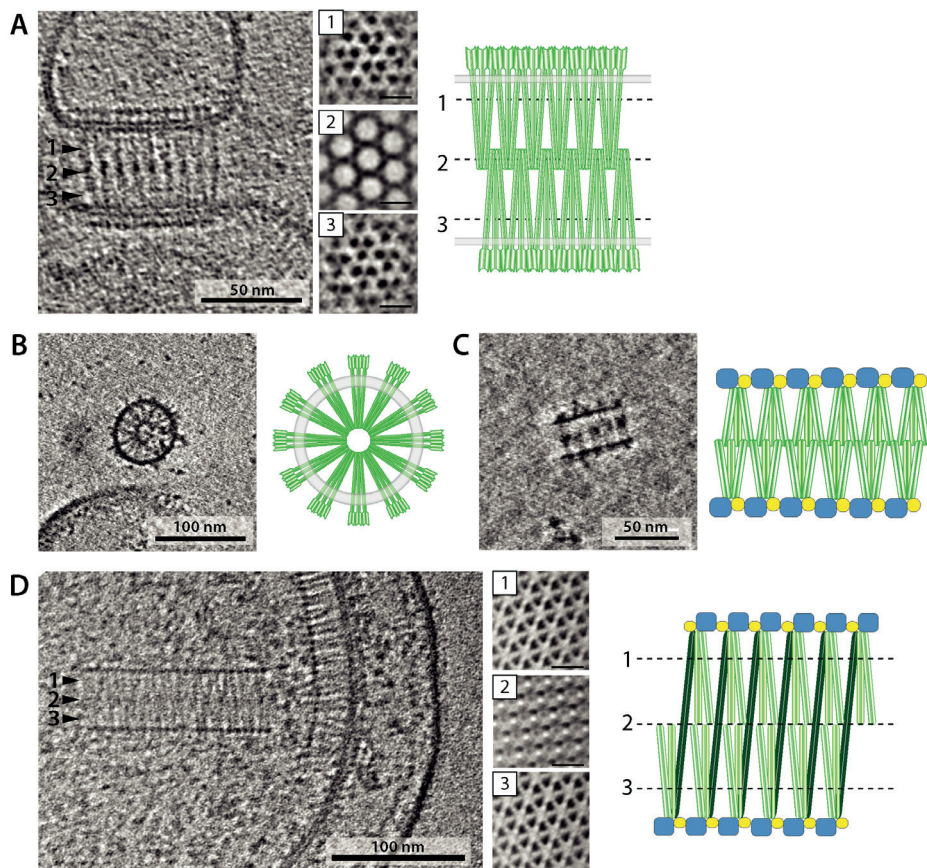


Figure 4. Chemoreceptor arrays in vitro and alternative chemosensory arrays in vitro and in vivo. In the absence of other chemotaxis proteins, membrane-bound chemoreceptors form “zipper” like arrays (A) or micelle-like structures (B) observed in cryo-ET images. Cryo-ET images are adapted from (58). (C) In vitro, truncated Tar receptors form “sandwich” structures consisting of two layers of arrays flanked by CheA and CheW. Image adapted from (103). (D) The native cytoplasmic chemosensory arrays in a *V. cholerae* cell shown in tomographic image. Cryo-ET image is adapted from (104). Insets 1-3, in both panel A and C, show the subtomogram averaging results corresponding to the cross sections of the arrays indicated in the tomographic image and the cartoon. The scale bars for insets 1-3 in panel A are 10 nm; the scale bars for insets 1-3 in panel D are 20 nm. For all cartoon illustrations, receptors are colored in green; kinases are in blue; the coupling proteins are in yellow and the membrane are depicted in gray. The DosM receptor in panel D is highlighted in dark green.

Compositional variability in the baseplate

The variety of baseplate components raises the interesting question of how bacteria utilize the diverse coupling proteins. For example, *V. cholerae* is capable of increasing CheV abundance in the baseplate to compensate for the absence of CheA in the F6 arrays (102). Fluorescence microscopy revealed that, under standard growth conditions, only the CheV2 protein encoded within the F6 gene cluster form localized foci at the cell pole. However, in the absence of CheA, CheV1 and CheV4 also form foci at the cell pole (Fig. 5B), demonstrating that the baseplate composition is adaptable. CheV3 remains diffuse in the cytoplasmic regardless of the abundance of CheA. This could mean that CheV3 interacts specifically with a particular MCP that is not expressed under the conditions tested (110) and is therefore not incorporated into the baseplate. This variability in structure is likely explained by the presence of SH3-like domains that differ in the coupling proteins, which allows for the dynamic swapping of the coupling proteins, allowing the incorporation of their specific MCPs. Thus, by adjusting the baseplate elements, bacteria can rapidly regulate the sensory functions of the chemosensory arrays to better suit the current environment.

Different baseplate stoichiometry

The stoichiometry of array components has been determined in *E. coli* (94). The baseplate has a ratio of monomeric CheA and monomeric CheW that fluctuates between 1: 1 and 1: 2. The latter ratio is in agreement with the extreme scenario where all CheA-empty rings are fully occupied with CheW hexamers. An increased abundance of CheW hexamers can be promoted *in vitro* by addition of excess CheW (45). In comparison to other bacteria, *E. coli* appears to have an unusually high ratio of CheA in the baseplate. In *B. subtilis*, the ratio of the baseplate components for CheA : CheW : CheV is 1:1:3 (115). In the F6 arrays of *V. cholerae*, there is even fewer CheA, with a CheA : CheW : CheV stoichiometry of 1:7:2 (102). Additionally, in *V. cholerae*, a small number of ParP molecules also integrate into the baseplate, suggesting that the baseplate consists of more coupling proteins than kinases. In *B. subtilis*, the ratio between receptor dimers and dimeric CheA was determined as 23 to 1, which is about four times higher than the ratio in *E. coli*, where the ratio is 6 to 1. Thus, in *B. subtilis* and *V. cholerae*, many receptors in the array bind solely to the coupling proteins.

The low abundance of kinase in the arrays of some species raises the question of whether the concept of core unit consisting of two receptor trimers-of-dimers, one CheA dimer, and two CheWs is applicable for those bacteria. In order to include a variety of baseplate components, Alvarado *et al.* proposed a variety of possible core unit schemes for the F6 arrays in *V. cholerae* (112). Alternatively, the core unit may be specific to *E. coli* arrays because of its high kinase abundance, whereas in most arrays receptor trimers-of-dimers are capable of integrating into the arrays as long as the

appropriate coupling protein is attached to its hairpin tips.

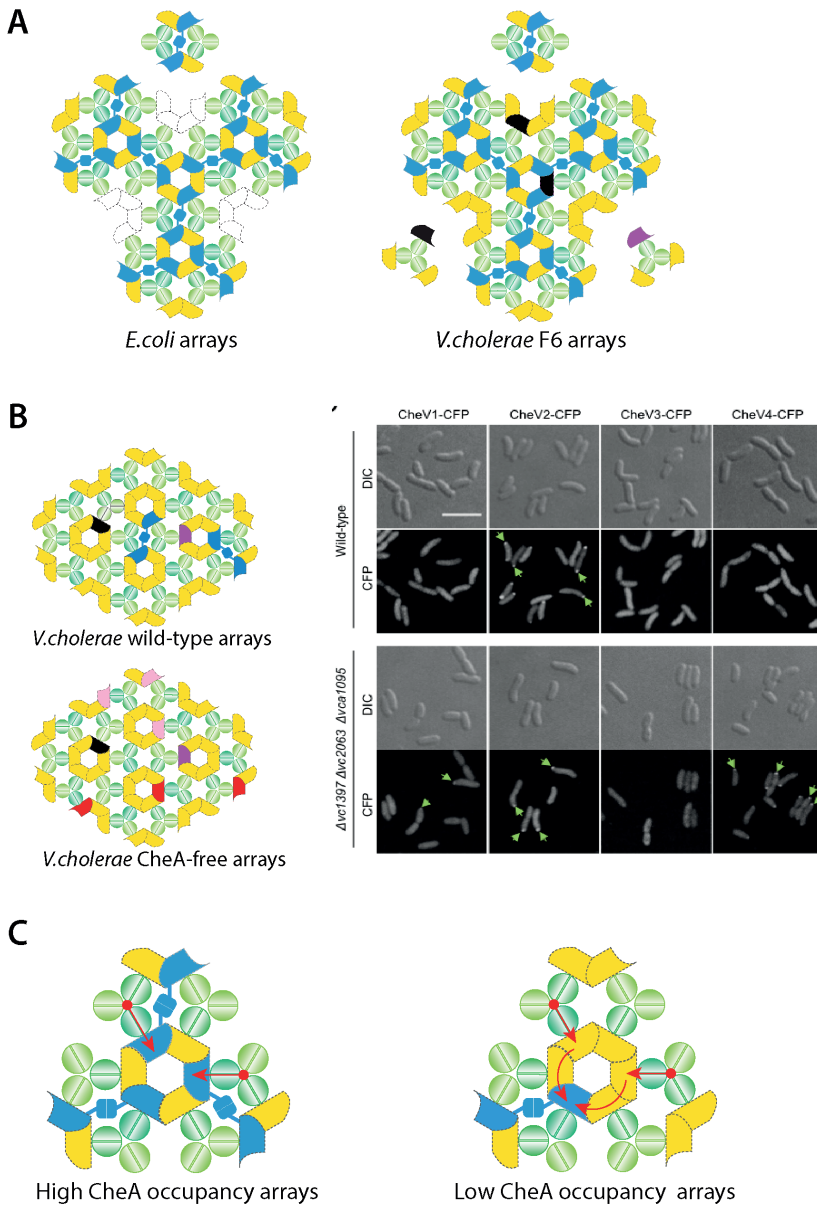


Figure 5. The baseplate variability of chemosensory arrays. (A) Comparison between chemosensory arrays in *E. coli* arrays (left) and the F6 arrays in *V. cholerae* (right). In *V. cholerae*, both ParP (black) and CheV (magenta) can directly integrate into the baseplate bringing in receptor trimer-of-dimers. (B) Cartoons (left) illustrates that more CheV proteins intergrate into the F6 arrays in *V. cholerae* when CheA is absent. Fluorescence microscopy images (right) show that in wild-type arrays (top 2 rows) only CFP-tagged CheV2 foci were observed at the cell poles. The foci of CFP-tagged CheV1 and CheV4 emerged at cell poles only when CheA

is absent (bottom 2 rows). The image is adapted from (102). CheV1, CheV2 and CheV4 are colored in red, magenta and pink, respectively, for the cartoons. (C) Arrays with low CheA occupancy (right) potentially encourage a higher cooperativity compared to arrays with a high CheA occupancy (left). Red dots represent receptors sensing a stimulus; red arrows indicate the possible direction of signal propagation in the baseplate.

A higher cooperativity among the receptors may also be required for species with a low abundance of kinase in chemosensory arrays. In *E. coli*, every CheA is directly in contact with a receptor trimers-of-dimers. In contrast, a single CheA in *V. cholerae* is assigned to an average of 6 receptor trimers-of-dimers, based on the stoichiometry data (102). Therefore, in *V. cholerae*, the signaling state of the receptors is likely to propagate horizontally through one or multiple multiple interfaces 2 before it can reach the nearest CheA (Fig. 5C). As interface 2 is considered to facilitate signal amplification and cooperativity, a long-range horizontal signaling propagation is potentially crucial for integration of diverse signaling inputs from a collection of various receptors and the proper kinase control. In arrays with a low kinase abundance and a high diversity in chemoreceptors, a higher signaling cooperativity is expected to facilitate the large repertoire of sensory inputs.

Chemoreceptor clustering depends on receptor length

The arrays undergo stochastic self-assembly and spontaneously nucleate new clusters that tend to collide and fuse with the cluster already localized at the cell pole (116). This often results in large polar chemosensory arrays and multiple small lateral clusters (117). However, not all receptors are expected to cluster into a single array. For membrane-bound arrays, the physical length of receptors predicts whether receptors can incorporate into the same chemotaxis array (51, 91). The intracellular length of chemoreceptors is influenced by the presence of several components, including the number of heptad repeats in the signaling domain, the number of the HAMP domains, the presence or absence of the PAS domains, and additional linker regions (118-120). In *E. coli*, all five chemoreceptors share a 36H signaling domain and possess the same physical length, and they indeed cluster together into a single array. Experiments have shown that the wild-type and artificially shortened receptors in *E. coli* cluster into separate arrays in a length-dependent manner and function separately (121). In *V. cholerae* and other bacteria, polarly positioned but distinctively separate arrays exist naturally, as shown in the tomographic image in Figure 6 (122). The short and long membrane-associated arrays are assigned as F6 and F7 arrays, respectively. The F6 arrays contain 40H receptors whose ligand-binding domains can be recognized in the periplasm. In contrast, the F7 arrays do not have discernible periplasmic domains, consistent with the absence of periplasmic and transmembrane regions in the known F7 chemoreceptors. How the F7 chemoreceptor array is anchored to the membrane is

unknown. The F7 arrays also contain distinctive additional density layers between the baseplate and the inner membrane, which is proposed to correlate with the presence of PAS and HAMP domains.

The requirement that receptors that coexist in single arrays must be of the same length appears to be stricter in the case of membrane-bound arrays compared to the cytoplasmic arrays. One special case is the cytoplasmic array in *V. cholerae* (104, 105). In this case, the DosM receptor (44H) forms arrays together with other, much shorter cytoplasmic receptors (20H). This unusual DosM receptor contains 2 signaling domains and interacts with both base plates in the array to serve as a structural scaffold.

What is the advantage of multiple arrays?

The explanation for why bacteria presenting multiple membrane-bound arrays at the same cell pole remains elusive. The spatial isolation of the two arrays suggests that the chemosensory pathways benefit from segregation of the receptors by preventing possible crosstalk. However, crosstalk among different pathways is reported in the bacterium *Comamonas testosteroni* (123). Here, the kinase of the motility control pathway can directly phosphorylate not only the response regulator within the same pathway, but also the response regulator from the pathway that regulates biofilm formation. Similarly, crosstalk between pathways has also been proposed in other bacteria, and it might be common in bacteria that are capable of multiple forms of motility (124-127).

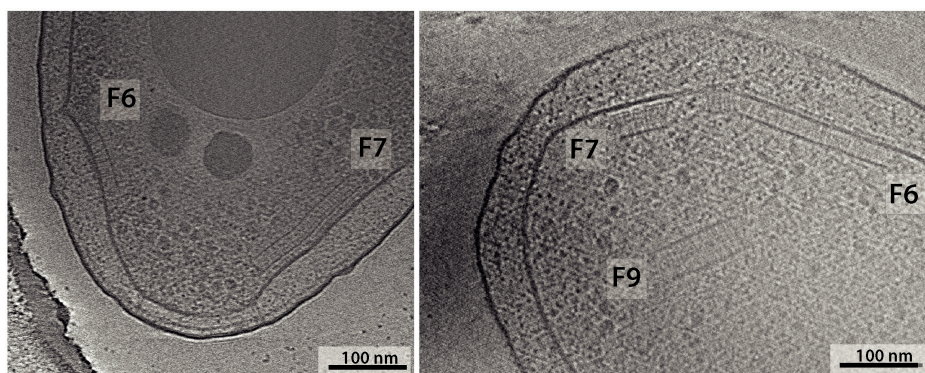


Figure 6. Co-existence of different chemosensory arrays shown in tomographic images of *P. aeruginosa* (left) and *V. cholerae* (right). The F6, F7 and F9 represent different chemotaxis systems classified on the basis of evolutionary history (70). Images are adapted from (122).

Understanding the functional specificity of chemosensory arrays for bacteria with multiple chemotaxis pathways is particularly challenging (128). Even assigning receptors to a certain pathway is not trivial. The difficulty is that the receptors and

cytoplasmic components of the same pathways are not always localized within the same operon. *P. aeruginosa* has five chemotaxis gene clusters comprising four different pathways. However, 22 of the 26 receptors encoded in the genome are located outside of the five gene clusters. Shown in a recent study, genetic analysis of the MCP-CheA, MCP-CheW binding regions identified the pathway-specific motifs of the receptors, which assisted the assignment of all receptors to the four pathways with known function (129, 130). For *Myxococcus xanthus*, the receptor phylogenetic distribution, genomic organization and subcellular localization analysis in combine revealed the distribution of 21 chemoreceptors in 8 chemotaxis pathways (127).

Conclusions and future perspectives

The physiological relevance of chemotaxis pathways depends on the specificities of the receptors displayed in the chemosensory arrays. However, our current understanding of what each chemoreceptor can sense is still rather limited. We find a vast diversity of MCPs in sequenced genomes, but the lack of a structure-function correlation in the ligand-binding domains prevents a reliable prediction of what a specific receptor may be able to sense (89). The growing insight into the immense diversity of bacterial chemotaxis presages the challenges ahead to determine the functional specificity of receptors, chemosensory arrays and chemotaxis pathways.

A fascinating characteristic of the chemosensory arrays is that, despite its highly conserved architecture, it has an incredibly high tolerance to its compositional variability. The increasing number of studies reporting a variety of chemosensory arrays found in various bacteria is truly exciting. However, the correlation between the architecture of the arrays and the stage in the life cycle of the cell or the presence of particular environmental cues is still elusive in most cases. Understanding and appreciating the variability of chemosensory arrays require two things: 1) case studies that illustrate how chemosensory in a single model organism functions; and 2) general cross-species studies that can reveal generally applicable trends.

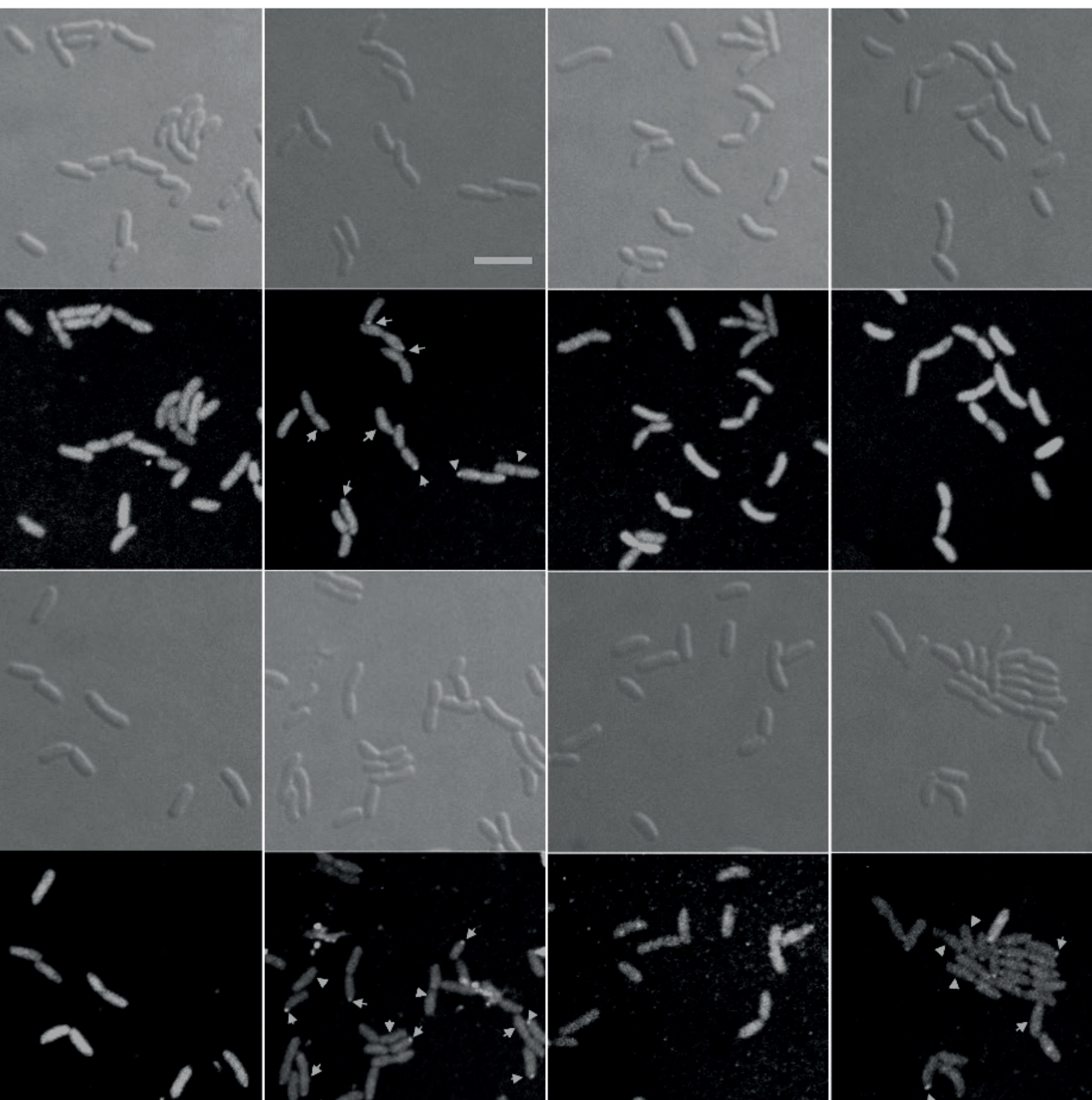
To gain new insights into the diversity of chemotaxis systems and their function, a combination of approaches will be necessary. For instance, we need to study chemotaxis under culture conditions that mimic the native environment or that reflect specific environmental niches instead of standard laboratory cultures. This need is highlighted by a recent study in which proteomic analysis was combined with cryo-electron tomography (cryo-ET) to study viable but non-culturable *V. cholerae* found in natural water samples (83). This study revealed distinctive changes in receptor composition of the F6 array, and the presence of the additional chemotaxis system (F9) in the non-

2

culturable state. Cryo-ET provides a direct visualization of the chemosensory arrays *in situ* in three dimensions. It is a powerful tool that can give insight into the native packing order of the receptors and even the overall architecture of the arrays at the molecular level (60, 131). However, this method is limited by the absence of detectable labels to identify proteins of interest. This limitation can be overcome by the use of fluorescence light microscopy for protein-specific targeting correlated (52), which can detect the localization and identification of the chemosensory arrays (105). In addition, electron microscopy can also provide valuable high-resolution structural information about either isolated array components or recombinant sensory complexes (132). Another powerful tool to study chemosensory arrays is fluorescence microscopy. This method is widely used for studying the clustering of chemotaxis proteins and their dynamics *in vivo* (102, 112). With an ever-improving resolution, for example using photoactivated localization microscopy (PALM) or stochastic optical reconstruction microscopy (STORM), fluorescence microscopy can potentially reveal the clustering of chemotaxis proteins and array segregation at the macromolecular level in living cells (133-137).

Besides imaging techniques, genomics-driven bioinformatics studies have greatly contributed to the tremendous progress in unraveling the diversity of chemotaxis pathways and their evolutionary plasticity. The classification scheme based on evolutionary history of signal transduction systems established by Wuichet and Zhulin has set up 19 classes for assigning chemotaxis clusters in unstudied species (70). Evolutionary genomics studies can also focus on common features of chemotaxis components and predict their function based on combination of phylogenetic profiling and comparative protein sequence analysis (110). Within a single species, comparative sequences analysis has revealed the specificity of the conservative motif of receptor/kinase and receptor/coupling protein interfaces and has assigned the receptors to different chemotaxis pathways (129). Undoubtedly, with more genomes sequenced, bioinformatics analysis will continue to provide valuable insights to direct experiments to test various hypotheses that are potentially applicable to a broader set of subjects.

CHAPTER 3



Baseplate variability of chemosensory arrays in *Vibrio cholerae*

This chapter is published as:

Yang W^{*1}, Alvarado A^{*2}, Glatter T³, Ringgaard S², Briegel A¹ (2018) Proceedings of the National Academy of Sciences 115(52):13365-13370.

- 1 Institute of Biology, Leiden University, Leiden, The Netherlands
 - 2 Department of Ecophysiology, Max Planck Insitute for Terrestrial Microbiology, Marburg, Germany
 - 3 Core Facility of Mass Spectrometry and Proteomics, Max Plankc Insitute for Terrestrial Microbiology, Marburg, Germany
- * These authors contribute equally to this work

Abstract

The chemoreceptor array, a remarkably ordered supramolecular complex, is composed of hexagonally packed trimers-of-receptor-dimers networked by a histidine kinase and one or more coupling proteins. Even though the receptor packing is universal among chemotactic bacteria and archaea, the array architecture has only been extensively studied in selected model organisms. Here, we show that even in the complete absence of the kinase, the cluster II arrays in *Vibrio cholerae* retain their native spatial localization and the iconic hexagonal packing of the receptors with 12 nm spacing. Our results demonstrate that the chemotaxis array is versatile in composition, a property that allows auxiliary chemotaxis proteins, such as ParP and CheV, to integrate directly into the assembly. Along with its compositional variability, cluster II arrays exhibit a low degree of structural stability compared to the ultrastable arrays in *E. coli*. We propose that the variability in chemoreceptor arrays is an important mechanism that enables the incorporation of chemotaxis proteins based on their availability.

Introduction

Chemotactic bacteria constantly assess their environment and compare their current situation with that of the recent past in order to bias their movements towards favorable surroundings. Changes in their environment are typically detected by transmembrane receptors known as methyl-accepting chemotaxis proteins (MCPs). Nutrients, toxins and biological signaling molecules bind to the periplasmic domains of the receptors either directly or via periplasmic binding proteins (PBPs) (68, 138, 139). MCPs communicate their binding state through the membrane to a HAMP (histidine kinases, adenylyl cyclases, MCPs, and some phosphatases) domain, which in turn communicates with their cytoplasmic tips to regulate the autophosphorylation of a histidine kinase, CheA. The kinase transfers phosphoryl groups to a response regulator, CheY, which then diffuses throughout the cell, binds to flagellar motors, and regulates their direction of rotation (140). In *E. coli*, either an increase of attractants or a decrease of repellents will lead to a reduced CheY-P production. In the presence of low CheY-P levels, the flagellar motors rotate counterclockwise, which results in a smooth-swimming motion ("run"). Increase of CheY-P promotes a change of spinning direction to clockwise, resulting in a random re-orientation of the cell ("tumbling"). Adjustments in the length of runs cause cells to follow gradients toward attractants and away from repellents.

The arrangement of chemoreceptors in hexagonal arrays has been shown to be universal in both Bacteria and Archaea (51, 55). In *E. coli*, the chemoreceptors are networked by rings of CheA and CheW into hexagonally packed arrays with a 12 nm spacing (43, 44, 99, 100, 141). Each set of three CheA dimers that link one receptor hexagon together lie at the vertices of a larger hexagonal lattice with a spacing of 21 nm (58). This ordered arrangement results in ultrastable receptor arrays that retain their highly ordered architecture even after cell lysis (43, 54, 58, 95, 142).

V. cholerae contains 3 chemotaxis operons (clusters 1-3), each of which forms its own structurally distinct arrays. Of these, clusters I and III are only expressed under certain growth conditions (low oxygen and as a general stress response, respectively) (80, 143, 144). The proteins from cluster I form cytoplasmic arrays, in which two baseplate layers sandwich cytosolic chemoreceptors and are stabilized by a specialized receptor with two signaling domains (104, 105). Cluster III is structurally not well understood at present. Neither of these systems has been implicated in canonical chemotactic behavior, and their cellular function remains elusive. In contrast, cluster II has been shown to be responsible for chemotactic behavior under all tested conditions so far (82). The arrays formed by cluster II proteins are expressed under standard growth conditions as well as under conditions in which clusters I and III are also expressed

(51, 104). Electron cryotomography (ECT) has previously revealed a typical hexagonal packing with a 12 nm spacing in the cluster II arrays (51). The same hexagonal packing order was also found in both receptor layers in the cytoplasmic cluster I arrays as well (104). *V. cholerae* possesses 43 MCPs genes that are scattered throughout the genome. 38 of these MCPs belong to the 40-heptad class (40H) (91), and this class of receptors integrates into the cluster II array (70). The cluster II arrays are strictly localized to the bacterial cell poles by the ParC/ParP system. ParC acts as a polar determinant that directs localization of arrays to the cell pole via its cognate partner protein ParP. ParP integrates into the array via its C-terminal AIF-domain through interactions with MCPs and CheA. The integration of ParP stimulates array formation and prevents the release of chemotaxis proteins from already-formed arrays (112, 145, 146).

The fact that ParP is not part of the chemotaxis system in *E. coli* reveals a structural variability of the chemotaxis arrays among species. Here, we show that the CheA/CheW-only array, as well as the ultrastability of receptor arrays, is characteristic for the chemotaxis system in *E. coli* rather than a universal feature shared among all chemotactic bacteria and archaea. We further show that, although the hexagonal packing of the chemoreceptors is universal among species, the baseplate that binds the receptor tips differs in its composition. Our studies reveal that the baseplate, as a variable structure, allows for the incorporation of alternative coupling proteins. This feature likely facilitates the exchange of different chemotaxis proteins within existing arrays in response to environmental cues. Our results on *V. cholerae* emphasize the importance of understanding the structure and function of chemoreceptor arrays in non-model organisms, especially in organisms in which highly versatile chemotaxis might be important for pathogenicity.

Results

CheA is not necessary for chemoreceptor array structure and formation

Because the baseplate of the chemoreceptor array of *V. cholerae* is different from the model organism *E. coli* (145), we set out to study the effect of baseplate composition on array formation, structure and stability. Because *V. cholerae* contains 3 chemotaxis operons, with one CheA encoded by each system, we constructed a triple *cheA* deletion mutant ($\Delta vc1397 \Delta vc2063 \Delta vc1095$). We considered it was important to delete the *cheA* gene from each chemotaxis cluster in order to avoid the possibility that CheA proteins of clusters I and III might substitute for CheAII in formation of cluster II arrays. Like the *cheA2* single-deletion mutant, this CheA-free strain was no longer capable of chemotaxis in soft agar assay (Fig.S3.1).

In order to investigate whether the receptors were still able to form ordered hexagonal arrays in the complete absence of all three CheA proteins, we performed electron cryotomography (ECT) analysis of this CheA-free mutant. The data revealed that arrays were still present, but with a 40% reduction in the number of cells with observable arrays compared to the wild-type. This result supports the importance of CheA in normal array formation. Notably, subtomogram averaging showed that, even in the complete absence of CheA, the chemoreceptors were still packed in a hexagonal order with the typical 12 nm spacing and were indistinguishable in structure from the wild-type Cluster II arrays (Fig. 1 A-B).

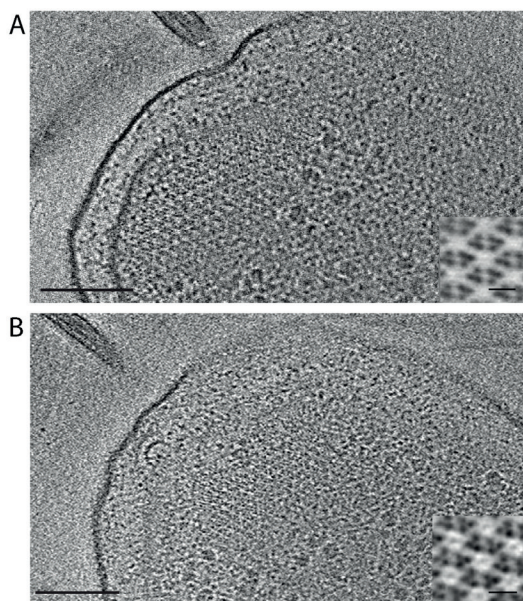


Figure 1. Cluster II chemoreceptor array observed in wild-type and CheA-free *V. cholerae*.

(A) Hexagonally packed chemoreceptor array with 12 nm spacing near the flagellar pole in wild type *V. cholerae*. (B) Hexagonal receptor array with 12 nm spacing in a CheA-free cell. Subtomogram averaging map is shown in the inserts for both stains. The scale bar is 200 nm for both tomoslices and 10 nm for both inserts.

Previous reports, based on fluorescence microscopy (FLM) studies in *E. coli*, suggest that CheW alone might be sufficient for receptor clustering, so that chemoreceptor arrays might still form in the absence of CheA (147). However, to our knowledge, our study is the first substantial proof that the receptors not only cluster together, but that they indeed form the typical ordered arrays in the complete absence of CheA. Thus, even though CheA is indispensable for the chemotactic function of the array, it is not indispensable for array formation or the hexagonal packing of chemoreceptors in *V. cholerae*.

CheA is not necessary for array localization

To study the role of CheA protein in the localization of cluster II arrays, we analyzed array localization in both the wild-type and the triple *cheA* deletion strain using a functional YFP-CheW1 fusion (148) as a marker. Ectopic expression and visualization of YFP-CheW1 revealed, as previously described (112, 148), that in wild-type cells YFP-CheW1 localized as distinct clusters at the bacterial cell poles in a uni- and bi-polar manner (Fig. 2A). Additionally, demographic analysis showed that short cells contained a single uni-polar YFP-CheW1 cluster, whereas longer cells contained a bi-polar localization of YFP-CheW1 clusters (Fig. 2B). Particularly, YFP-CheW1 was uni-polarly localized in 53 % of cells and bi-polarly localized in 44 % of cells (Fig. 2C). YFP-CheW1 showed an identical cell length-dependent polar localization pattern in the triple *cheA* deletion background (Fig. 2A-B) and a similar ratio of cells with uni- (52 %) and bi-polar (42%) localization (Fig. 2C) when compared to wild-type cells. In direct support of the FLM results, all the CheA-free arrays observed by ECT were localized very near the flagellar basal body (Fig. S3.2). Thus, the correct localization of the array lattice does not depend on the presence of CheA. Given that either CheA2 or ParP alone was shown to be sufficient for CheW1 clustering, and thus for array formation (112), we believe ParP is still present in the CheA-free array and effectively assumes the role of CheA2 in facilitating array formation.

CheA does not influence recruitment of new chemotaxis proteins

To further understand the role of CheA in array formation, we performed fluorescence-recovery-after-photo bleaching (FRAP) experiments with YFP-CheW1 in wild-type and the triple *cheA* deletion background. Bleached clusters of YFP-CheW1 recovered their fluorescence intensity in the triple *cheA* deletion strain in the same manner as in the wild-type, demonstrating a continuous recruitment of new CheW1 to the chemotaxis arrays in both strains (Fig. 2D-E). This observation clearly shows that CheW1 does not depend on the presence of CheA to extend the pre-formed array lattice, which indicates that CheA does not play an indispensable role in recruiting new chemotaxis proteins into the existing arrays. Given that the formation of arrays is detected much less frequently in the total absence of CheA proteins, it confirms that CheA is more likely to play a crucial role in the initiation of array formation rather than regulating the incorporation of new baseplate protein in pre-formed arrays.

***V. cholerae* Cluster II arrays are highly unstable**

In order to achieve an improved resolution (2-3.5 nm) of *E. coli* chemoreceptor arrays by ECT, several laboratories have applied cell lysis either by antibiotic treatment or by inducing a phage lysis gene to flatten the cells (54, 55, 58, 142). Both methods resulted in lysed cells with chemoreceptor arrays that clearly retained their architecture (Fig. 3A). In fact, it was reported the architecture of the arrays in lysed cells was indistinguishable

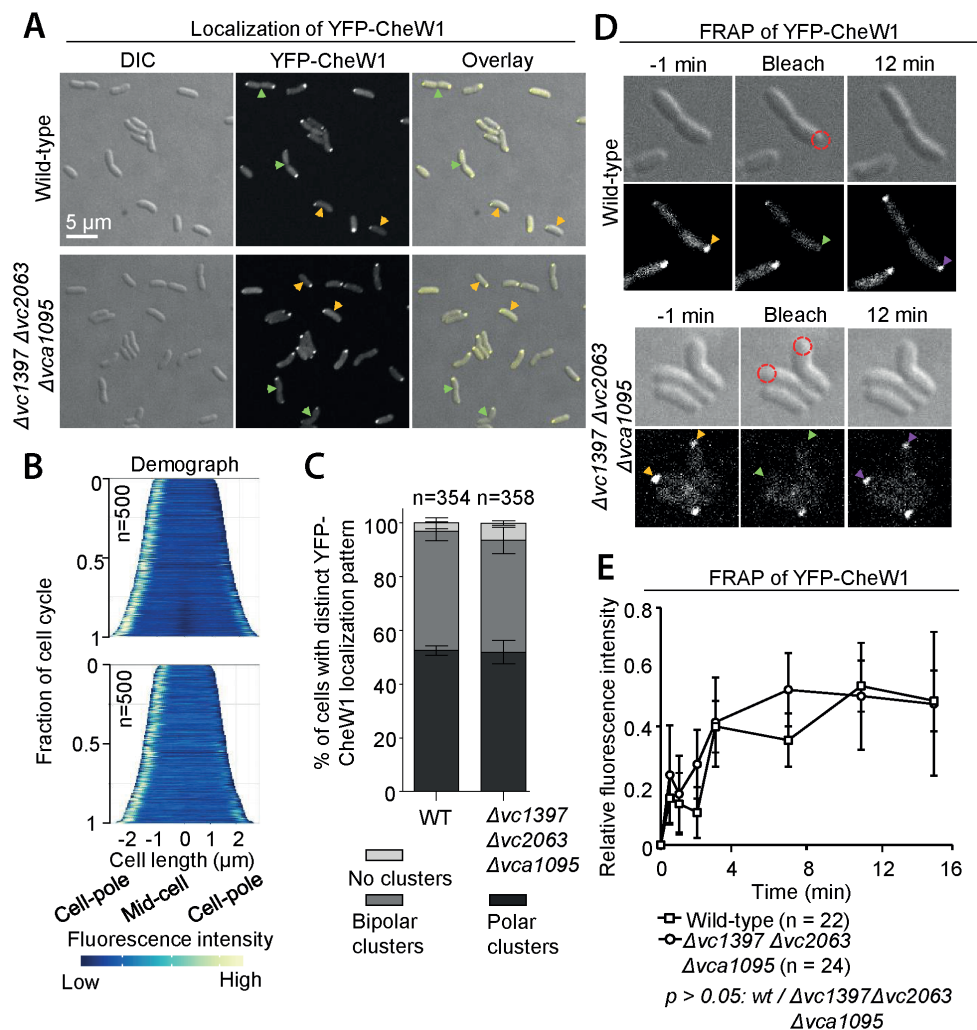


Figure 2. Formation of YFP-CheW1 clusters in the absence of CheA proteins. (A) Fluorescence microscopy images show the intracellular localization of YFP-CheW1 in wild type and the indicated *V. cholerae* mutants. Orange arrows indicate cells with uni-polar localization of YFP-CheW1, and green arrows indicate cells with bi-polar localization of YFP-CheW1. The scale bar represents 5 μ m. (B) Demographs showing the fluorescence intensity of YFP-CheW1 along the cell length in a population of *V. cholerae* cells relative to cell length. The n-value indicates the number of cells analyzed. (C) Bar graph showing the percentage of cells with distinct YFP-CheW1 localization patterns in the indicated *V. cholerae* strains. The n-value indicates the total number of cells analyzed from three independent experiments. (D) Fluorescence- recovery-after-photobleaching (FRAP) experiment of YFP-CheW1 clusters. Clusters recover post-bleaching in wild type and a strain deleted for all CheA proteins. Numbers indicate minutes pre- and post-bleaching. The dashed circle outlines the bleached region. Yellow arrows indicate the pre-bleaching clusters, green arrows indicate the bleached clusters and the purple arrows indicate clusters with a recovered YFP signal. (E) Graph depicting the

fluorescence intensity of YFP-CheW1. The YFP-CheW1 post-bleach signal intensity the cell pole is plotted relative to the initial pre-bleach at the pole intensity normalized to 1. The average fraction recovery is shown. In panels C and E, error bars indicate standard of the error mean (149).

from that of arrays analyzed in intact minicells (43, 44). However, instead of one continuous superlattice, the arrays are more often found in patches in lysed *E. coli*. In contrast, the same antibiotic-induced gentle cell lysis resulted in a quick loss of hexagonal packing in the *V. cholerae* chemoreceptor arrays (Fig. 3B). Even though the receptors clearly remain localized at the cell pole close to the flagellar motor, their ordered packing is almost completely disrupted. Similar to the array side views in lysed *E. coli* (Fig. 3C), as well as side views of cluster II arrays in intact *V. cholerae* (Fig. 3D), the receptors appear to be intact and clustered in lysed *V. cholerae* (Fig. 3E). The baseplate is still visible in the side views, suggesting that the occupancy of receptors' membrane distal end was not completely lost. However, instead of a continuous baseplate layer in intact cells, the density of the baseplate is discontinuous in the lysed *V. cholerae*. Tomographic results from lysed *V. cholerae* cells also revealed micelle-like zipper structures, where the receptors bend the inner membrane through the association of their membrane distal ends (Fig. 3F). Similar structures, which represent a different mode of receptor clustering, were frequently observed in *E. coli* when the chemoreceptors were disproportionally overexpressed relative to CheA and CheW (58, 150). Overall, these observations demonstrate that the cluster II array in *V. cholerae* does not exhibit an ultrastable structural integrity like the arrays in *E. coli*. It is noteworthy that this disruption of receptor packing order is only visible with ECT imaging and cannot be detected by fluorescence light microscopy. As a further support for the baseplate disruption, quantitative analysis of chemotaxis proteins in the membrane fraction of lysed *V. cholerae* cells clearly showed that baseplate components were not co-enriched with the membrane bound MCPs (Fig. S3.3).

The composition of the *V. cholerae* Cluster II array is variable and exhibits a distinct stoichiometry of chemotaxis proteins

To further understand the higher degree of instability of the *V. cholerae* cluster II arrays, we set out to determine the stoichiometry between the baseplate chemotaxis proteins CheW, CheA and ParP using targeted LC-MC proteomics on wild-type *V. cholerae* cells. Initial proteomic analysis was used to determine the synthetic heavy peptides used as standards for quantification of CheW1, CheA2 and ParP ratios. Peptide samples were spiked with identical amounts of the heavy peptides in order to calculate the relative ratio between the identical light peptides from CheW, CheA and ParP. The analysis revealed a stoichiometry between CheW1:CheA2:ParP of 35:5.3:1 (Fig. 4A), showing that CheW1 is highly abundant compared to CheA2 and especially ParP, indicating that

the cluster II baseplate is primarily composed of CheW1, to a lesser extent of CheA2, and with an even lower level of ParP.

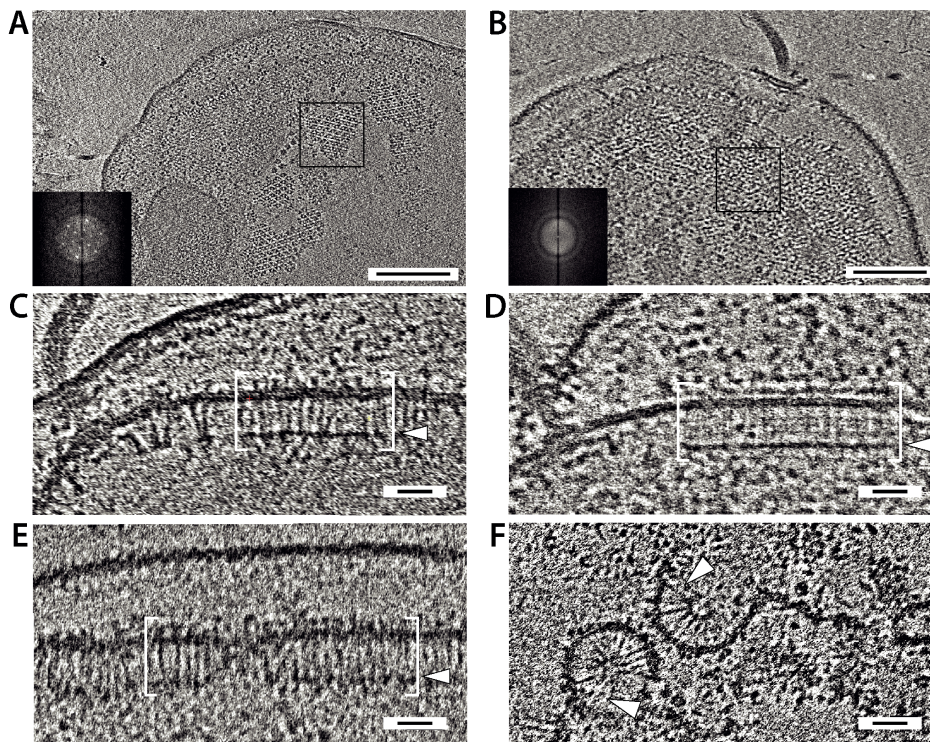


Figure 3. Chemoreceptor arrays in lysed *V. cholerae* and *E. coli*. (A) The hexagonal packing order can be clearly identified in a lysed *E. coli* cell. The insert is the power spectrum that displays a strong diffraction pattern in the boxed region of the receptor array. (B) Lysis disrupts the chemoreceptor array packing order in *V. cholerae*. Strong density representing the receptors is still clustered near the flagellar pole, yet no hexagonal order can be detected in either the tomoslice or the power spectrum (insert). Scale bar for A and B is 100nm. (C) Side view of chemoreceptor array in a lysed *E. coli* cell. (D) Side view of cluster II array in an intact *V. cholerae* cell. (E) Side view of the cluster II array in lysed *V. cholerae* showing a discontinuous occupancy at the baseplate compared to the continuous density shown in panel C and D. White brackets and arrows highlight the receptor array and baseplate, respectively in panels C-E. (F) Tomoslice of a lysed *V. cholerae* cell where receptors associated through their membrane distal ends forming micelle-like structures. White arrows point at the receptors. Scale bar is 20 nm for panels C-F.

V. cholerae also encodes four predicted CheV proteins (VC1602, CheV1; VC2006, CheV2; VC2202, CheV3; and VCA0954, CheV4) in its genome. CheV is a fusion protein between CheW and CheY and integrates into the baseplate similar to CheW (151). Sequence alignment showed that all four CheVs possess the hydrophobic residues that mediate interaction between CheW, CheA-P5 and ParP-A1F, respectively, with the MCP

interaction tip (Fig. S3.4), suggesting that all four CheVs have the potential to integrate into the cluster II array baseplate. In a global proteomic analysis, we were able to detect the presence of all four predicted CheV proteins (Table S3.4), showing that they are all expressed under the conditions assayed. Furthermore, we detected all proteins from cluster II but none from Cluster I and III. This result suggests that CheV proteins are continuously expressed similar to cluster II proteins and thus have the potential to contribute to the structure of the baseplate of the cluster II array and consequently to array formation and/or stability.

We investigated the intracellular localization of all four CheVs by ectopically expressing CFP-tagged versions of each protein individually. Fluorescence microscopy showed that, in wild-type cells, only CheV2-CFP localized in clusters at the cell poles whereas CheV1-CFP, CheV3-CFP and CheV4-CFP were diffusely localized in the cytoplasm (Fig. 4B). Thus, CheV2 is the primary CheV integrated into cluster II arrays in wild-type cells. Targeted LC-MS analysis revealed that the stoichiometry of all the baseplate proteins, CheW1:CheA2:ParP:V1:V2:V3:V4, is 50:7.5:1.4:3.8:1:4.3:4.9 (Fig. 4D). CheW is clearly the most abundant of the baseplate proteins, followed by CheA2. Furthermore, CheV2 was the least abundant of all of the baseplate proteins, even though it appears to be the primary CheV protein in the cluster II arrays. In the absence of all CheA proteins, we observed that not only CheV2-CFP formed polar clusters in ~56% of cells (a level identical to that observed for wild-type cells), but also CheV4-CFP and CheV1-CFP were polarly localized in approximately ~57% and ~25% of the population, respectively (Fig. 4C). Thus, it appears that both CheV1 and CheV4 are able to integrate into the arrays in the absence of CheA proteins. This recruitment of different CheV proteins under certain conditions suggests that the baseplate is a highly variable structure and is capable of adjusting its composition in order to accommodate changes in the dynamic accessibility of different chemotaxis proteins. Indeed, CheVs are predicted to coordinate with certain receptors to integrate into the array and to modulate receptor function (110).

Discussion

The architecture of bacterial chemoreceptor arrays has been predominantly studied in the model organism *E. coli*, in which the structural core of the array is composed of rings formed by alternating P5 domains of CheA and CheW. These rings network the trimers of receptor dimers in the typical hexagonal lattice. The architecture of these arrays, in which six rings of CheA/CheW surround a ring lacking CheA predicts a stoichiometry of 1:1:6 (CheA:CheW:MCPs) in these array, or 1:2:6 if the CheA-less hexagons are not empty but instead filled with CheW only (43). This architecture

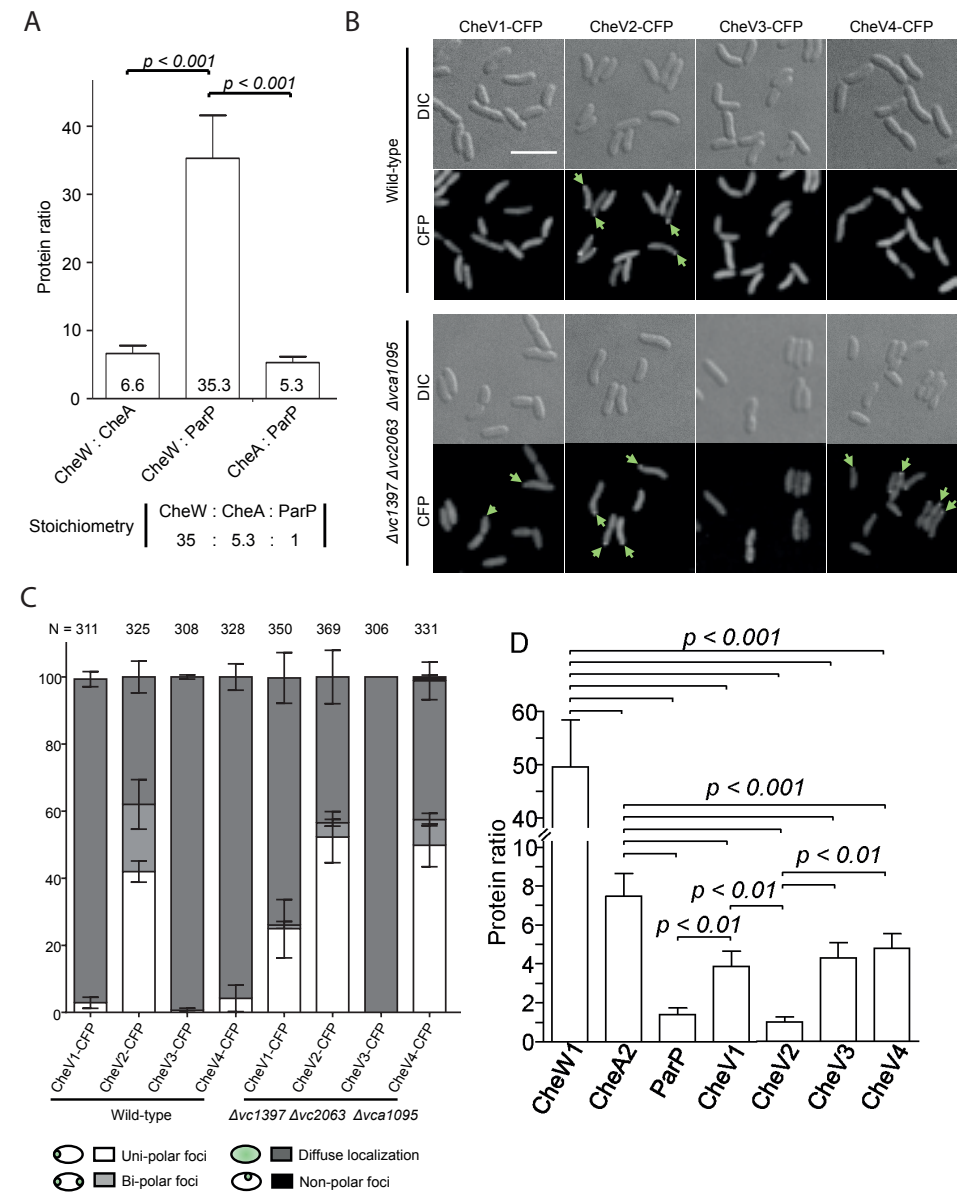


Figure 4. Stoichiometry and variability in the *V. cholerae* baseplate. (A) Bar graph showing the ratio between the chemotaxis proteins CheW1, CheA2 and ParP from cluster II determined by targeted LC-MS. Error bars indicate SEM. (B) Fluorescence microscopy of cells expressing the four CheVs in wild-type *V. cholerae* and a strain deleted for all three cheA genes. Scale bar indicates 5 μ m. Green arrows indicate polar clusters of CheV proteins. (C) Bar graph depicting the percentage of cells with specific localization patterns of the four CheV proteins in wild-type *V. cholerae* and a strain deleted for all three cheA genes. (D) Bar graph showing the ratio between the chemotaxis protein CheW1, CheA2, ParP and CheV1-4 from cluster II array determined by targeted LC-MS. Error bars indicate standard deviation of the mean in panels A, E and F. P values were calculated by Student's t-test.

agrees with the experimentally determined protein ratios that have been published (94, 95, 152). It is possible that because of the flexible stoichiometry among the ternary components, the direct visualization of the CheW-only rings *in vivo* has not yet been reported. Meanwhile, in the recombinant array assembled *in vitro*, the array formation was commonly promoted with CheW in molar excess of CheA, typically at the ratio of 1:2 (103, 141). In those studies, such a high concentration of CheW may strongly favor CheW only rings in the CheA-less hexagons. As a result, ECT studies and subsequent subtomogram averaging indeed revealed CheW-only rings *in vitro* (141). However, it is still unclear whether all rings lacking CheA are filled up with 6 CheW monomers to create a complete ring *in vivo*. Our results with CheA-free *V. cholerae* provided an extreme case in which the majority of the receptor trimers-of-dimers bind to CheW at the baseplate. The baseplate composed predominantly of CheW is clearly sufficient to arrange the receptor in a hexagonal packing (Fig. 5A). This result certainly favors the possibility that CheW-only rings are sufficient to network the receptor trimers into the native hexagonal packing to form a super-lattice.

The observation of CheA-free arrays that we report here does not diminish the structural importance of CheA protein in the array. On the contrary, it highlights the significance of CheA for maintaining the overall structural integrity of chemoreceptor arrays. The CheA homodimer integrates into two neighboring receptor hexagons in the lattice, linked by its P3 dimerization domain (47). Thus, CheA dimerization is crucial for interlinking neighboring CheA/CheW rings and also for establishing the whole allosteric network of the complex (92). In *E. coli*, the ratio of CheA dimer to the total amount of coupling protein is 1:4, assuming that all CheA-free rings are filled with CheW. The high CheA occupancy ensures that each trimer of receptor dimers directly binds to a P5 domain of CheA. Consequently, the hexagonal packing of the receptors is guaranteed regardless of the presence of the CheW-only rings (Fig. 5C). Our stoichiometry data show that the ratio of CheA dimer to other coupling proteins in *V. cholerae* is 1:14, which is dramatically lower than in *E. coli*. Therefore, there are much fewer CheA dimers in the baseplate that can function as “structural staples” to interlink the rings, which are predominantly formed by the coupling protein CheW (Fig. 5B). It is worth mentioning that the low abundance of CheA does not eliminate the existence of complete CheA/CheW rings in cluster II arrays. Yet, this structure is likely to be interspersed in the lattice given the low CheA/CheW ratio, which would not provide an equivalent stability to the array architecture as extensively networked CheA/CheW rings do. Ultrastability of *in vitro* array complexes has been reported previously, which was proposed to arise from the multiple linkages between the individual core complexes (95). ECT studies later provided experimental evidence for the array stability based on the universal appearance of the chemoreceptor array lattice after cell lysis, which has been shown for example in *E. coli*, *B. subtilis* and *T. maritima* (43, 51, 142). The stoichiometry of CheW:

CheA: ParP : CheV in *V. cholerae* provides a plausible explanation for why cluster II arrays are not as stable as those of *E. coli*. We further expect a variance of the chemoreceptor array stability exist among other species in which the stoichiometry of the baseplate components deviates from the stoichiometry established in *E. coli*.

ParP from *V. parahaemolyticus* forms dimers (146) similar to those formed by ParP from *V. cholerae*, as suggested by a bacterial-two-hybrid assay (Fig. S3.5). ParP may also form dimers through the flexible linker between its C-terminal AIF domain and the N-terminal ParC interaction domain. Thus, ParP may substitute for the CheA homodimer in the baseplate instead of competing with CheW monomers. If so, then ParP is potentially capable of contributing to array stability in the same way as CheA dimers despite its comparatively low abundance.

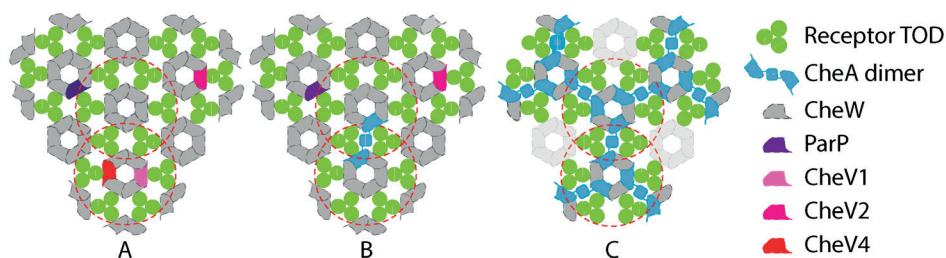


Figure 5. CheA dimer occupancy in different arrays. (A) CheA-free array in *V. cholerae*. Baseplate is predicted to be composed of CheW-only rings with sporadic insertion of ParP, CheV1 and CheV4. (B) Cluster II array in wild-type *V. cholerae*. CheA2 dimers serve as a structural “staple” that interlinks the ring networks in the baseplate. Due to the low occupancy of CheA2 dimer (1:14) compared to the other coupling proteins, only a few neighboring receptor hexagons are structurally interlinked. (C) *E. coli* array. The 1:2 ratio of CheA dimer to CheW result a highly structured packing of receptors and base plate components. The red dashed circles outline individual receptor hexagons in the receptor array super-lattice.

The stoichiometry of the *V. cholerae* cluster II baseplate components reported here suggests a high level of dynamics in baseplate architecture during array formation. Due to a more diverse composition of the baseplate, it is conceivable that the array lattice develops at the cell pole through a dynamic recruitment of receptors that bind CheA, ParP, CheV and predominantly, CheW. This is in direct contrast to *E. coli*, in which the core units are thought to assemble first, and subsequently associate to form the extended receptor arrays with a strict stoichiometry and ordered arrangement of both the receptors and the baseplate protein CheA and CheW (58). This assembly process may reflect the relative simplicity of the *E. coli* chemotaxis system. The compositional diversity of baseplates can also be found in other organisms for which the ratios of chemotaxis proteins ratios have been determined. For example, in *Bacillus subtilis*, the baseplate also contains CheV, and the array stoichiometry was determined to be

1:1:3:23 (CheA:CheW:CheV:MCP) (115). These differences in protein ratios indicate that the protein arrangement in the baseplate varies significantly depending on the organism and perhaps the growth conditions, even though the receptors are packed in the typical hexagonal lattice (43, 51, 55). It seems that the architecture of the baseplate tolerates different levels of baseplate proteins. This conclusion is supported by the loss of ordered CheA distribution in arrays where the array proteins are overexpressed from different plasmids (58).

Taken together, our results emphasize that there are significant differences in the composition and architecture of the chemoreceptor array among species. In the case of *V. cholerae*, the less-stable arrays may be the result of the variable composition of the baseplate proteins. This finding is consistent with the high number of different MCPs encoded by *V. cholerae*. Their integration into the array super-lattice is believed to depend on the presence of specific coupling proteins (110). Additionally, the array variability may enable a swift adaptation by exchange of new chemoreceptors within the existing array lattice during in response to altered environmental conditions. In contrast, the *E. coli* system might have evolved to form ultrastable arrays, which provide a robust generic chemotaxis response without the need for adding or exchanging array components once assembled. Our findings highlight the need to study chemoreceptor array structure and composition in different organisms to properly understand the diversity and biological significance of chemotaxis signaling.

Materials and Methods

Construction of strain AA26

The wild-type strain of *V. cholerae* used was the El Tor clinical isolate C6706 and all mutants are derivatives of this strain. Strain AA26 was constructed by sequential in-frame deletions of vc1397, vc2063 and finally vc1095. To perform deletions, *E. coli* strain SM10λpir was used to transfer DNA into *V. cholerae* cells. Derivatives of suicide vector pCVD442 were employed to construct AA26 by standard allele exchange techniques. Stains and the plasmids and primers used for construction are listed as Table S3.1 - S3.3 in the supplementary information.

Construction of plasmids

Plasmid pAA100. Genomic DNA of *V. cholerae* was used to amplify *vc1602* gene with primers 3039 and 3024. Similarly, *cfp* was amplified from plasmid pMF391 using primers 3025 and 565. Both PCR products were used as template for a third PCR using primers using primers 3039 and 565. The resulting product was digested with enzymes XbaI and SphI and inserted in the corresponding sites of vector pBAD33, resulting in

plasmid pAA100.

Plasmid pAA101. The gene *vc2006* was amplified using genomic DNA as template with primers 3027 and 3028. Using vector pMF391, *cfp* was amplified using primers 3025 and 565. Both PCR products were used as template for a third PCR using primers using primers 3027 and 565. The resulting product was digested with enzymes XbaI and SphI and inserted in the corresponding sites of vector pBAD33, resulting in plasmid pAA101.

Plasmid pAA102. To create this plasmid *vc2202* was amplified from genomic DNA using primers 3029 and 3037. Vector pMF391 was used for template of *cfp* amplified using primers 3025 and 565. Both PCR products were used as template for a third PCR using primers using primers 3029 and 565. The resulting product was digested with enzymes XbaI and SphI and inserted in the corresponding sites of vector pBAD33.

Plasmid pAA102. Similarly, *vca0954* was amplified from genomic DNA with primers 3031 and 3038. Vector pMF391 was used for template of *cfp* amplified using primers 3025 and 565. Both PCR products were used as template for a third PCR using primers using primers 3031 and 565. The resulting product was digested with enzymes XbaI and SphI and inserted in the corresponding sites of vector pBAD33 giving pAA102.

Growth conditions and media

V. cholerae and *E. coli* were grown in LB media or on LB agar plates at 30°C or 37°C containing antibiotics in the following concentrations: streptomycin 200 µg/ml; ampicillin 100 µg/ml; chloramphenicol 20 µg/ml for *E. coli* and 5 µg/ml for *V. cholerae*.

Cell Lysis

For lysis, *V. cholerae* and *E. coli* were first cultured overnight with 200 rpm shaking at 30 °C in LB and TB media, respectively. Overnight cultures were diluted with fresh media at 1:500, then incubated at 30 °C with shaking for another 3 hours. 2000 UI/ml penicillin was added to the culture when OD₆₀₀ was reached. After an additional hour of incubation, cells were harvested by centrifugation. Lysis was monitored under the light microscope.

Fluorescence microscopy

Fluorescence microscopy was performed essentially as described earlier (80). *V. cholerae* cells were grown at 37 °C with shaking in LB medium including chloramphenicol for selection of plasmid pSR1033. Ectopic expression of YFP-CheW1 was induced by addition of L-arabinose to a final concentration of 0.2% v/v when the cell culture reached OD₆₀₀ 0.8-1.0. Subsequently, cell cultures were incubated an additional hour. To collect images, cells were mounted on a 1% agarose pad, which included 10% LB

and 20% PBS. Images were collected using a Nikon eclipse Ti inverted Andor spinning-disc confocal microscope equipped with a 100x lens and an Andor Zyla sCMOS cooled camera. Acquisition settings (exposure time and laser intensity), were kept identical throughout all experiments. Images were analyzed using ImageJ imaging software (<http://rsbweb.nih.gov/ij>) and Metamorph Offline (v 7.7.5.0, Molecular Devices, Union City, CA). When counting the percentage of cells with distinct localization patterns of YFP-CheW1, three biological experiments were performed. Cells were enumerated by hand and for each experiment >100 cells were counted. The mean of the three experiments was then plotted with error bars indicating the standard-error-mean (79). A t-test was performed to calculate the p value. Demographic analyses were performed as previously described (79). Software R studio version 3.0.1 (<http://www.rstudio.com/>) along with ggplot2 version 0.9.3.1 (Hadley Wickham, Department of Statistics, Rice University) were employed. For demographic analysis, the data from three independent biological experiments were pooled. For each experiment >100 cells were analyzed. The total number of cells included in the demograph (n) is mentioned in the figure.

Determination of isotopically labeled reference peptides for CheA, CheW and ParP

Vibrio cholerae C6706 (lacZ-) was grown at 37 °C in liquid LB medium until OD₆₀₀ reached ~0.5-0.7. Cells were pelleted by centrifugation and washed twice with PBS buffer (20%). Sample preparation, LC-MS and data analysis were carried out as described previously (153, 154) with the exception of the proteolytic digest, which was carried out using a tandem LysC/trypsin digest. Following protein solubilization using 2% Sodiumlauroylsarcosinate (SLS) the detergent concentration was diluted to 0.5% with 100 mM Ammoniumbicarbonate. To 50 µg total protein extract, 500 ng LysC (Wako) was added and incubated for 4 hours at 37 °C. Then digest was continued by adding 1 µg trypsin (Promega) for overnight at 30 °C. Detergent depletion and preparation of peptides for LC-MS analysis was carried out as described previously (153).

The peptides were then analyzed using liquid-chromatography-mass spectrometry carried out on a Q-Exactive Plus instrument connected to an Ultimate 3000 RSLC nano and a nanospray flex ion source (all Thermo Scientific). Peptide separation was performed on a reverse phase HPLC column (75 µm x 42 cm) packed in-house with C18 resin (2.4 µm; Dr. Maisch). The following separating gradient was used: 98 % solvent A (0.15 % formic acid) and 2 % solvent B (99.85 % acetonitrile, 0.15 % formic acid) to 32 % solvent B over 90 minutes at a flow rate of 300 nl/min. In order to identify the most suitable peptides for peptide standard synthesis, digests from *Vibrio cholerae* lysates were analyzed using data-dependent acquisition (153). In brief, the MS parameters were set as follows: MS1 resolution of 60 000 (m/z 200), scan range from 375 to 1500 m/z, MS/MS scans of the 10 most intense ions with 17 500 (m/z 200). The ion accumulation

time was set to 50 ms (both MS and MS/MS). The automatic gain control (AGC) was set to 3×10^6 for MS survey scans and 1×10^5 for MS/MS scans. MS raw files were searched using MASCOT (v 2.5, Matrix Science) with the following criteria: semitryptic tryptic specificity; two missed cleavages were allowed; carbamidomethylation (C) was set as a fixed modification; and oxidation (M) and deamidation (N,Q) were set as a variable modification. The mass tolerance was set to 10 ppm for precursor ions and 0.02. Search results were loaded into Scaffold 4 (Proteome software) and peptides were chosen as candidates for peptides synthesis when only fully cleaved and no miscleaved version of this peptide was observed.

3 Targeted Liquid chromatography-mass spectrometry (LC-MS)

Before solid-phase extraction, isotopically labeled reference peptides (TQL, JPT Peptide Technologies) for CheA, CheW and ParP were prepared according to the manufactures' instruction and added to the digested lysate with a concentration of 20 fmol/ μ l. For targeted-MS analysis the mass spectrometer first acquired a full MS-SIM scan with an MS1 resolution of 70,000, ACG target setting of 1e6 and 100 ms max injection time. Then PRM scans were carried out with a MS2 resolution of 35,000, AGC target settings of 2e5, 100 ms and an isolation window of 2 m/z. Normalized collision energy was set to 27%. The analysis was performed unscheduled. For data analysis the results were imported into Skyline (v. 4.1.0.111714) (155).

Electron Cryotomography

Penicillin treated cells were enriched by centrifugation and protein A-treated 10 nm colloidal gold solution (Cell Microscopy Core, Utrecht University, Utrecht, The Netherlands) was added. After vortexing, aliquots of 3 μ l was applied to freshly plasma-cleaned R2/2, 200mesh copper Quantifoil grids (Quantifoil Micro Tools GmbH, Germany). Plunge freezing was carried out in liquid ethane using a Leica EMGP (Leica microsystems, Wetzlar, Germany). Grids were blotted at 20°C and at 95% humidity. Data acquisition was performed on a Titan Krios transmission electron microscope (Thermo Fisher Scientific, OR, USA) operating at 300 kV. Images were recorded with a Gatan K2 Summit direct electron detector (Gatan, Pleasanton, CA) equipped with a GIF-quantum energy filter (Gatan) operating with a slit width of 20eV. Images were taken at a nominal magnification of 42,000 x, which corresponded to a pixel size of 3.513 Å. Tilt series were collected using UCSFtomo with a bidirectional tilt scheme (0° to -60°, followed by 0° to 60°) with a 2° increment. Defocus was set to -8 μ m. The cumulative dosage used was 120 e-/Å² and 80 e-/Å² for unlysed and lysed cells, respectively.

Tomogram Reconstruction and Subtomogram Averaging

Drift correction, bead-tracking based tilt series alignment were done using IMOD (156). CTFplotter was employed for CTF determination and correction (157). Tomograms

were reconstructed using both weighted back-projection and simultaneous iterative reconstruction (SIRT) with iteration number set to 9. Dynamo was used for particle picking and subtomogram averaging (158, 159).

Sample size and analysis

For fluorescence microscopy experiments sample size and demographic analysis was performed as previously described (112). The total number of cells included (n) is mentioned for each experiment and demograph in the respective figures. For global transcriptomics and targeted LC-MC analysis the results are based on a minimum of four independent experiments. The mean was then plotted with error bars representing the standard deviation. The p-value was calculated performing a Student's t-test.

Supplementary Information

Table S3.1. Strain list

Strain ID	Genotype	Reference
<i>V. cholerae</i> C6706	<i>lacZ</i> -	
AA26	Δ vc1397 Δ vc2063 Δ vca1095 <i>lacZ</i> -	This Work

Table S3-2. Plasmid list

Plasmid ID	Description	Reference
pCVD442	Suicide vector for gene deletion	
pAK13	Plasmid to delete <i>vc2063</i>	(112)
pCVD442-VCA1095-flank	Plasmid to delete <i>vca1095</i>	This work
pPM041	Plasmid to delete <i>vc1397</i>	(276)
pMF391	PBAD:: <i>cfp</i>	This work
pBAD33	Arabinose induced expression vector	(277)
pSR1033	PBAD:: <i>yfp-vc2059</i>	(148)
pAA100	PBAD:: <i>vc1602-cfp</i>	This work
pAA101	PBAD:: <i>vc2006-cfp</i>	This work
pAA102	PBAD:: <i>vc2202-cfp</i>	This work
pAA103	PBAD:: <i>vca0954-cfp</i>	This work

Table S3.3. Primer list

Primer ID	Sequence (5'-)
565	CCCCCGCATGCTCACTTGTACAGCTCGTCCATGCC
3024	TCTCGCCCTTGCTCACCAT GAGCTCGAGGATGTC CATATTCAGGATATATTATCCAT
3025	GACATCCTCGAGCTC ATGGTGAGCAAGGGCGAGGA
3027	CCCCC TCTAGA ATGTCAGGTGTTTTGAACACGGTA
3028	TCTCGCCCTTGCTCACCAT GAGCTCGAGGATGTC GGAAAGCACTTCTCGCAATCTT
3029	CCCCC TCTAGA ATGACGGGTATTCTTGATT
3031	CCCCC TCTAGA ATGGCTAAAGTCGTCAGTAA
3037	TCTCGCCCTTGCTCACCAT GAGCTCGAGGATGTC TTTAACTAGCGCAGCTTTAC
3038	TCTCGCCCTTGCTCACCAT GAGCTCGAGGATGTC CGATTTTTGCAAACGCTGCGTCT
3039	CCCCC TCTAGA ATG AGCAACCCAAGCAGTACTA

Table S3.4. Abundance of chemotaxis proteins detected by global LC-MS proteomic analysis.

Presence of chemotaxis proteins in <i>V. cholerae</i>							
			Detection				Detection
Cluster I	VC1394	MCP	No	Cluster III	VCA1088	MCP	No
	VC1395	CheY1	No		VCA1089	CheB3	No
	VC1396	HP	No		VCA1090	CheD	No
	VC1397	CheA1	No		VCA1091	CheR3	No
	VC1398	CheY2	No		VCA1092	MCP	No
	VC1399	CheR1	No		VCA1093	CheW2	No
	VC1400	HP	No		VCA1094	CheW3	No
	VC1401	CheB1	No		VCA1095	CheA3	No
	VC1402	CheW	No		VCA1096	CheY4	No
	VC1403	MCP	No	CheVs	VC1602	CheV1	Yes
	VC1404	HP	No		VC2006	CheV2	Yes
	VC1405	MCP	No		VC2202	CheV3	Yes
	VC1406	MCP	No		VCA0954	CheV4	Yes
Cluster II	VC2059	CheW1	Yes	Others	VC2201	CheR2	No
	VC2060	ParP	Yes				
	VC2061	ParC	Yes				
	VC2062	CheB2	Yes				
	VC2063	CheA2	Yes				
	VC2064	CheZ	Yes				
	VC2065	CheY3	Yes				

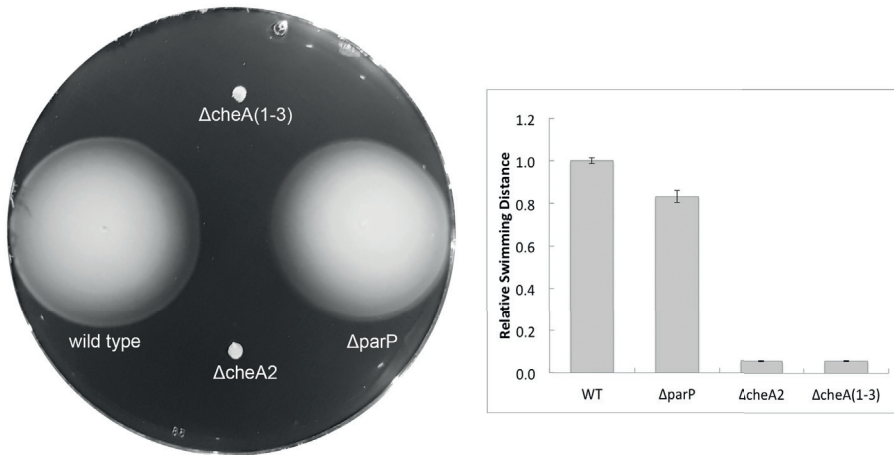


Figure S3.1. Soft agar assay shows chemotactic behavior in *V. cholerae* wild-type and stains with selective chemotaxis protein deletion. ParP deletion had little impact on the chemotaxis ability (N=25). No chemotactic ring was observed for *cheA2* deletion strain or *cheA(1-3)* deletion strain, which suggested the chemotactic behavior in those two strains was largely impaired.

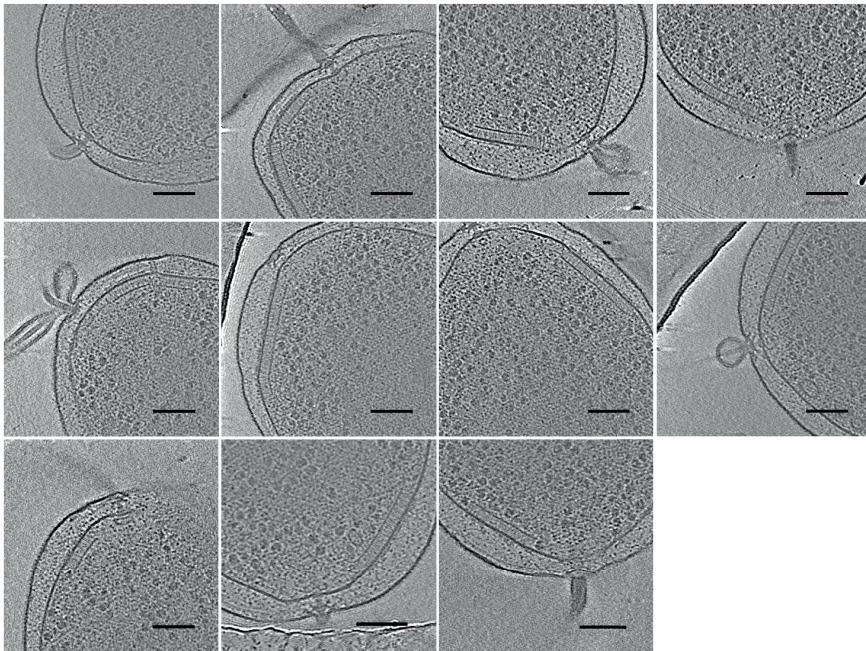


Figure S3.2. Localization of cheA-free cluster II chemoreceptor arrays in *V. cholerae*. Among 27 cell poles examined, all 11 chemoreceptor arrays observed were closely localized to the polar flagellar. Scale bar is 100 nm.

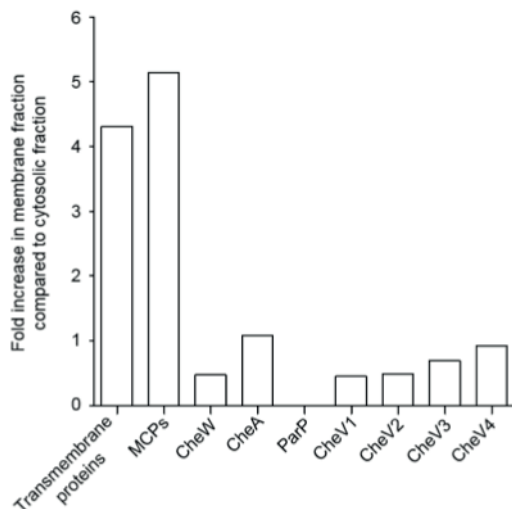


Figure S3.3. Baseplate proteins do not co-fractionate with MCP proteins in membrane fractions. The bar graph shows the average (average of four experiments) fold increase in the membrane fraction compared to the cytosolic fraction of total annotated transmembrane proteins, total detected MCP proteins and the baseplate proteins including CheW, CheA, ParP, CheV1-4. Notably, ParP protein was not detected at all in the membrane fraction.

```

Therm_mari-CheW 1 MKTLADAL-----KEFEVLSFEIDE-----QALAFDNDNIEM
Escher_col-CheW 1 MTGMINVTKLASEP---SGQEFVFTLGD-----EYIGIDILKVQE
V_cholerae-AIF 1 -----QVLYFDVNG-----VTFAPVLDLGG
VC1602-CheV1 1 MTIMSNPSSITLSTESGTNELEIEFHLEKVLDPDGRTKTCYGINVAKVRE
VC2006-CheV2 1 MSGVLNTVDQRINLVGENRLELLLFSLNS-----R-QIFAINVFKVRE
VC2202-CheV3 1 MTGILDSVNQRTQLVQGNRLELLTFRNLG-----R-QRYGINVFKVRE
VCA0954-CheV4 1 MAKVVSKANQ-----SQGMLMFTLSA-----QQQLFAIGTLKVRE

```



```

Therm_mari-CheW 33 VIEKSDITPVPKSRHFVEGVINLRGRIIPVVNLAKILGISF---DEQKM
Escher_col-CheW 39 IRGYDQVTRIANTPAFIKGVINLRGVIVPIVDLRIKFSQVDV--DYNDN
V_cholerae-AIF 22 IHRMTTLNHLIGRPAWYLGQTNRDSQLDVVDIAKWVMAEKLRLDESQKQ
VC1602-CheV1 51 VIRVPETTDYPNAQPHMIGVFSSREILTPLVDLAGNLGVPTS--TDISK
VC2006-CheV2 43 VIKVPLLTMPGSHPHITGVASLRGEPVPFVIDLRSAGIFPPRRV-QDTE
VC2202-CheV3 43 VLQCPKLTSMPLHRLVKGVAHIRGQTVSVIDMSLAVGGRPTT--DVVDK
VCA0954-CheV4 36 IVTVYQPMTIPIYSHHHVIGTVTIRNLTVPFVIDMAAAGFRPIQPSSEYQK

```

Residues important for CheW
interaction with MCPs in *T. maritima*

Arginine in *E. coli* CheW responsible
for modulation of CheA activity

Figure S3.4. Alignment showing the conservation of residues in *V. cholerae*. CheVs, CheW, and ParP-AIF that are required for interaction with MCP proteins. The alignment suggests that all four CheVs should be able to integrate into the chemoreceptor array.

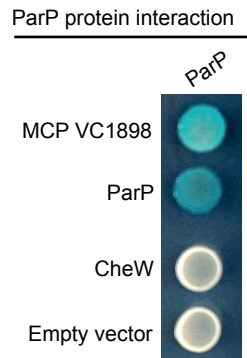
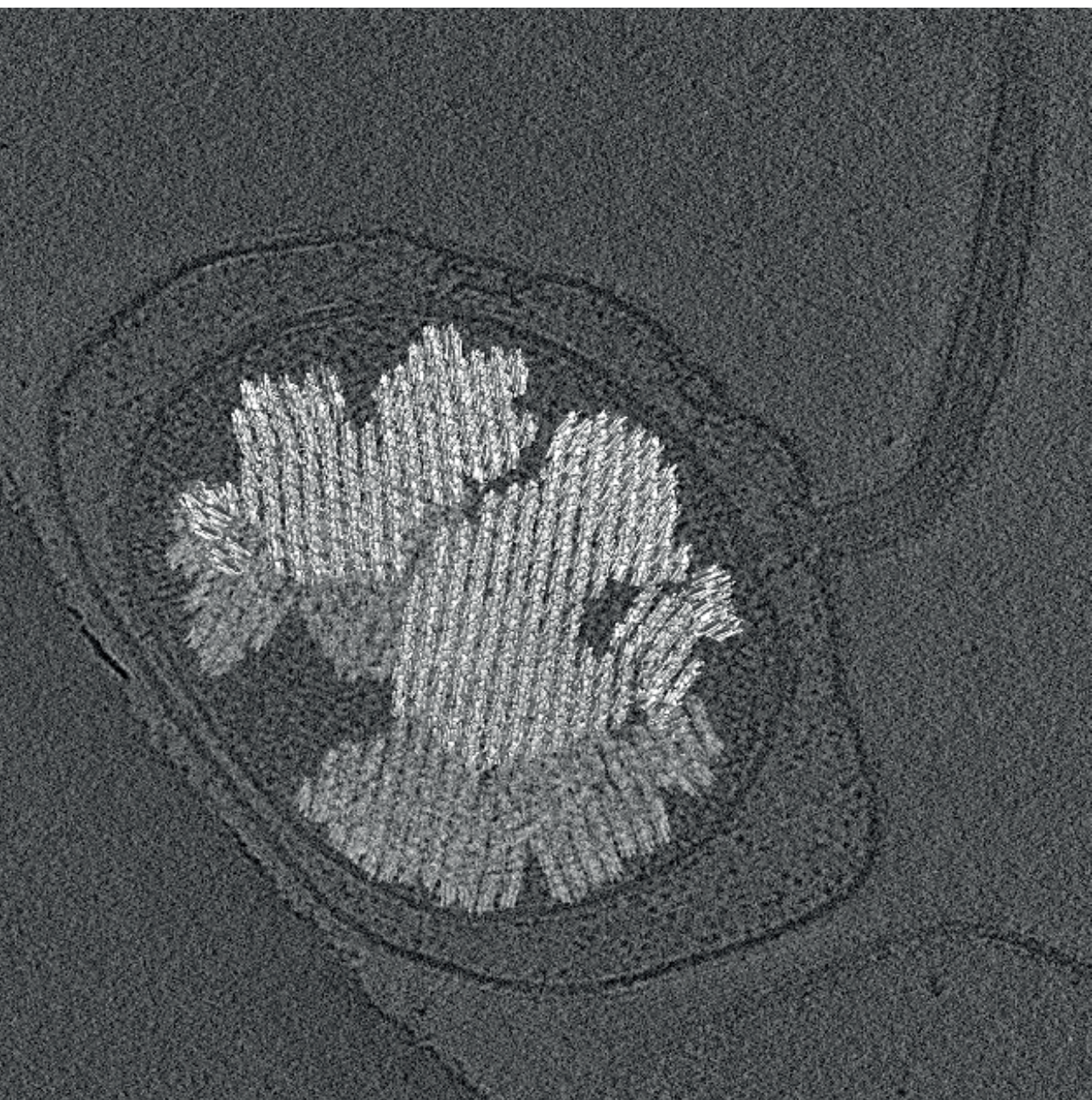


Figure S3.5. Bacterial-two-hybrid assay for screening protein interaction between the *V. cholerae* ParP with MCP VC1898, ParP and CheW. Blue coloration of bacterial colonies indicates an interaction.

CHAPTER 4



Kinase distribution in *Vibrio cholerae* F6 chemotaxis arrays

Abstract

Chemotaxis is a widespread behavior among motile bacteria that allows the cells to sense chemical changes in the environment and modulate their motility accordingly. The signals are sensed by chemoreceptors that arrange in extended ordered arrays and cluster together with other essential chemotaxis proteins, including CheA, the key enzyme in the signaling pathway. The receptor packing in ordered hexagonal arrays is considered universal among all bacteria and archaea. Despite the conserved receptor lattice, here we show that the molecular architecture of the chemotaxis proteins in the baseplate differ in the F6 arrays in *Vibrio cholerae* compared to its F7 counterpart in *Escherichia coli*. Cryo-electron tomography allows the visualization of the CheA positions in intact arrays of *V. cholerae*. The data reveals that CheA proteins are evenly distributed across the baseplate but lack an ordered arrangement. We propose such a variable distribution of CheA reduces the rigidity of the arrays and thus allows for a more dynamic exchange of different chemoreceptors and the baseplate components, which is the structural basis for a proper chemotaxis function with high cooperativity.

Introduction

Chemotaxis is a behavior most motile bacteria employ that allows the cells to sense their environment and direct their movement towards favorable environmental niches for survival. For the human intestinal pathogen *Vibrio cholerae*, the chemotaxis machinery aids the cells' survival during its life cycle, both in its environmental phase and during host infection (160-165). However, it is difficult to pinpoint the exact role of chemotaxis in *V. cholerae* pathogenicity due to contradictory results (166-170). Nevertheless, changes in chemotactic capability and motility may be associated with vastly altered localization in the host intestine (168, 171, 172).

Given the diverse environments where *V. cholerae* thrives, it is not surprising that their chemosensory system is much more complex than the best-understood model system in *E. coli* (63, 64). *V. cholerae* is equipped with 43 chemoreceptor-encoding genes in its genome. Moreover, *V. cholerae* possess 3 chemotaxis gene clusters, each of which comprises an individual chemotaxis pathway and a structurally distinctive chemosensory array (104, 122, 170, 173). The exact functions of Cluster I and Cluster III chemotaxis pathways remain largely elusive (80, 83). CheA-2, the functional homologue of the histidine kinase CheA in *E. coli*, and CheY-3, which is the only CheY that can directly control the rotation of the single polar flagellum, are both encoded by genes in Cluster II (82, 174). Furthermore, Cluster II chemosensory (also referred as F6 arrays classified based on the evolutionary history), is the only system in *V. cholerae* that appears to control motility (70).

In *E. coli*, membrane-bound chemoreceptors form trimers-of-dimers, which are arranged in a hexagonal lattice, networked at their cytoplasmic tips through rings formed by the P5 domain of the kinase CheA and the coupling protein CheW (43, 44, 47). In *V. cholerae*, the membrane-bound F6 arrays are always located at the flagellar pole (113). These arrays were shown to have a high compositional complexity, which is not only due to the number of different chemoreceptors. The Cluster II arrays also contain additional chemotaxis proteins, such as ParP and CheVs, that can integrate directly into the baseplate in addition to CheW and CheA (112, 151). F6 arrays can still self-assemble and retain native packing order of receptors even in the absence of all three CheAs (102). However, recent work implies that in order to compensate for low abundance or even the total lack of CheA, less frequently used coupling proteins are recruited into the baseplate instead. The stoichiometry of chemotaxis proteins based on proteomics data suggests that CheA abundance is naturally much lower in native *V. cholerae* F6 arrays compared to arrays in *E. coli* (102).

Although we speculated about the structural arrangement of CheA in the baseplate in our previous study, we were not able to visualize its distribution. This was largely due to the thickness of intact *V. cholerae* cells, which is prohibitive for high-resolution imaging. In *E. coli*, this thickness limitation was overcome in previous studies by cell lysis to flatten the cells. The arrays in *E. coli* are known to be ultrastable and the arrays withstand lysis without changes to their ultrastructure. In contrast, the F6 arrays *V. cholerae* tend to lose their native packing order upon cell lysis. However, the arrangement of CheA in the F6 arrays, either in an ordered or disordered fashion, may shed important insights into the formation and function of this system.

In this study we use cryo-electron tomography (cryo-ET) to image the F6 arrays in their native state in *V. cholerae* minicells. We applied subtomogram averaging analysis to determine the kinase distribution in the baseplate of intact F6 arrays. Our structural analysis of baseplate components agrees with the determined abundance of CheA based on the proteomics results reported previously. It further supports that the F6 arrays tolerate a high level of variability of chemoreceptors and chemotaxis proteins.

Results

***V. cholerae* minicells are suitable system for imaging F6 arrays**

V. cholerae are comma-shaped gram-negative bacteria with a diameter between 0.5 – 1.0 microns. These dimensions exceed the practical limit of Cryo-ET to reveal fine structural detail. In this study, we use a derivative strain of *V. cholerae* N16961 with *minCD* and *matP* deletions (175). Strains with one or multiple deletions in the *min* gene cluster are capable of releasing minicells from the cell pole of rod-shape bacteria (176). These achromosomal cells often retain some polar collated machinery, which make them an ideal system for studying chemosensory arrays (43, 44, 177). The minicells have a reduced size with an average diameter of 400 nm (52 minicells imaged in total) (Fig. 1A). The smallest minicells imaged are less than 200 nm in diameter. Chemotaxis arrays can be seen in the tomograms either as a hexagonal lattice (top views) or as a density layer parallel to the inner membrane (side views) (Fig. 1 B&C). Chemotaxis arrays were observed in 65% of all flagellated minicells imaged.

Chemoreceptor lattice in F6 arrays are hexagonally packed

Subtomogram averaging of the chemoreceptor arrays revealed that the receptors form a lattice that spans 23 nm between the baseplate and the inner membrane (Fig. 2A). The distance from the cytoplasmic tips of the receptors that are associated to the baseplate components to the periplasmic domains of the receptors is about 33 nm. The receptors are arranged in the typical hexagonal lattice with a spacing of about 12 nm.

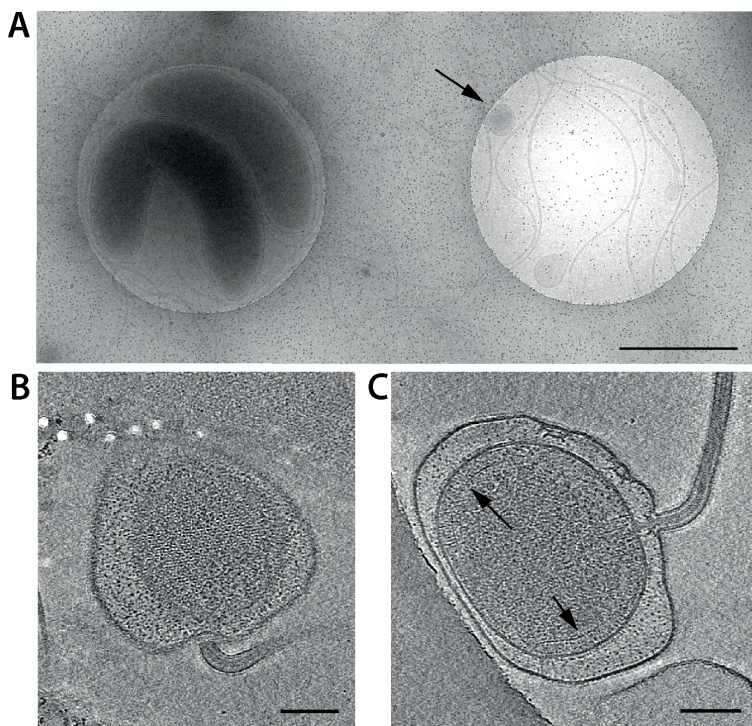


Figure 1. Representatives of *V. cholerae* minicells imaged by cryo-electron microscopy.

(A) Cryo specimen of 2 regular size cells (left) and a minicell (right, indicated by an arrow) on a Quantifoil film patterned with holes. Scale bar is 1 micron. Black dots are gold nanoparticles added as fiducial markers. (B) Tomoslice of a minicell shows the hexagonal lattice. (C) Tomoslice of a minicell shows the baseplate of the chemotaxis arrays (indicated by arrows) in side view. Scale bars for panel B and C are 100 nm.

The hexagonal pattern is apparent in the cytoplasmic region of the receptors, except in regions right beneath the inner-membrane (Fig. 2B&C). The hexagonal pattern in Fig. 2B is formed through the association among receptor trimers-of-dimers. The baseplate also has a hexagonal arrangement, which corresponds to a network assembled by a variety of the chemotaxis proteins (Fig. 2D). As reported before, the receptors exhibit the typical hexagonal lattice formed by trimers-of- dimers (Fig. 2E).

Kinase can be visualized in the baseplate

Straightforward subvolume averaging of receptor hexagons does not reveal a density corresponding to the kinase. Similar to *E. coli*, the CheA in *V. cholerae* also forms homodimers. With a molecular weight of 154 kDa, the CheA dimer should be resolved and distinguishable from the major baseplate scaffolding protein CheW (18kDa monomers). Furthermore, other baseplate components, such as CheV (36kDa) and ParP (42kDa), also structurally differ significantly from CheA due to both size differences and

their sporadic presence predicted for in the wild type F6 arrays.

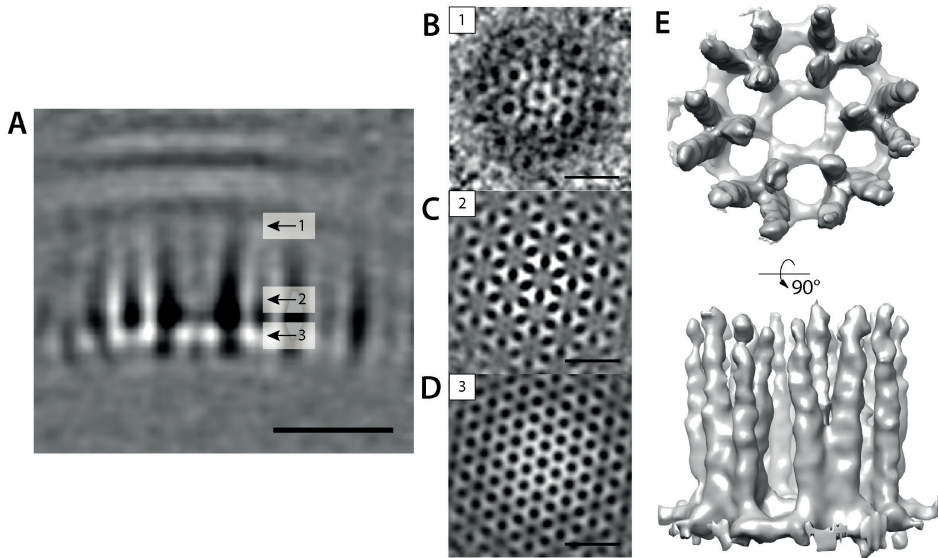


Figure 2. Subtomogram averaging result on the chemoreceptor lattice. (A) A side view of the average of receptor lattice. (B-D) Topview showing the hexagonal pattern of receptor lattice at different regions indicated in panel A. (E) Isosurface rendering of the receptor hexagon average. Scale bars in all panels are 20 nm and the density is shown in white.

Based on previous results, the baseplate of F6 arrays in *V. cholerae* are expected to be different from that found in *E. coli* based on the lower abundance of CheA (102). The stoichiometry based on proteomics analysis predicts a ratio between CheA and all other baseplate proteins combined is roughly 1:6. In order to determine the location of CheA, we used principle component analysis and k-means based classification to categorize the receptor hexagons. However, the classification was not able to reveal the location of CheA. This strongly suggests that, unlike in *E. coli* where there is an alternating CheA-filled and CheA-empty ring pattern in the baseplate, the distribution of CheA in *V. cholerae* is more sporadic.

By using multi reference alignment, the receptor hexagons can be further classified into different classes with different numbers of CheAs attached beneath the receptor hexagons. For each class, the averaged volume exhibits a density that resembles CheA dimers protruding from the baseplate (Fig. 3A). The receptor arrays in *E. coli* contain a maximum of 3 CheAs per receptor hexagon. The number of CheAs in *V. cholerae* can range from 0 to 3. Noticeably, although the averages suggests there could be 3 CheAs in one of the classes, not all CheA-like densities seem to be equally robust (Fig. 3B)

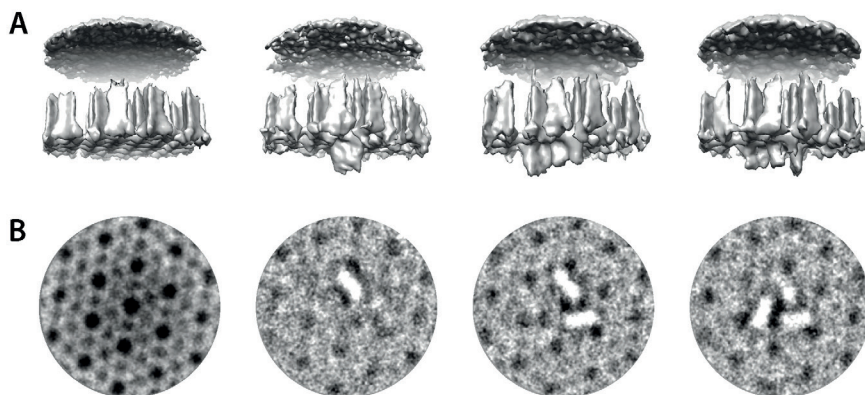


Figure 3. CheAs are visualized in classified averages base on their abundance within the baseplate. (A) Isosurfaces, from left to right, represent four classes showing 0 to 3 CheA-like densities in the bottom of the baseplate. The layer of density on top of each averaged volume corresponds to the inner membrane. (B) 2D images at the baseplate, from left to right, showing the CheA occupancy underneath the receptor hexagons.

Kinase distribute evenly yet without a pattern in baseplate

Even with CheA-like densities shown in the classification results, the individual EM maps are not informative enough to describe where the kinases are located in the context of receptor lattice. In order to visualize the location of kinase in arrays, the averages of receptors and CheAs are plotted back into the original tomograms following the coordinates and orientations derived from the iterative alignment results (Fig. 4A). Such composite volume reveals the CheA locations in the baseplates of native chemosensory arrays (Fig. 4B). Such visualization reveals that CheA is distributed evenly throughout the baseplate but lacks an ordered arrangement. This is in contrast to the highly ordered arrangement found in *E. coli*, where the baseplate is composed of alternating CheA-filled and CheA-empty rings under receptor hexagons. Instead, in the individual hexagons in *V. cholerae*, we find a variety of CheA arrangements, ranging from 0 to 3 per ring (Fig. 4C). Noticeably, in certain regions the CheA-filled and CheA-empty ring structures could still be found. However, such local CheA arrangement appeared to be extremely rare throughout a continuous chemosensory array.

Discussion

In this study, the distribution of the kinase CheA in the baseplate of intact chemotaxis cluster II arrays (F6 arrays) in *V. cholerae* was determined for the first time. We found that the CheA distribution appears evenly across the baseplate of arrays but it lacks any detectable pattern. This kinase distribution is in agreement with the low CheA

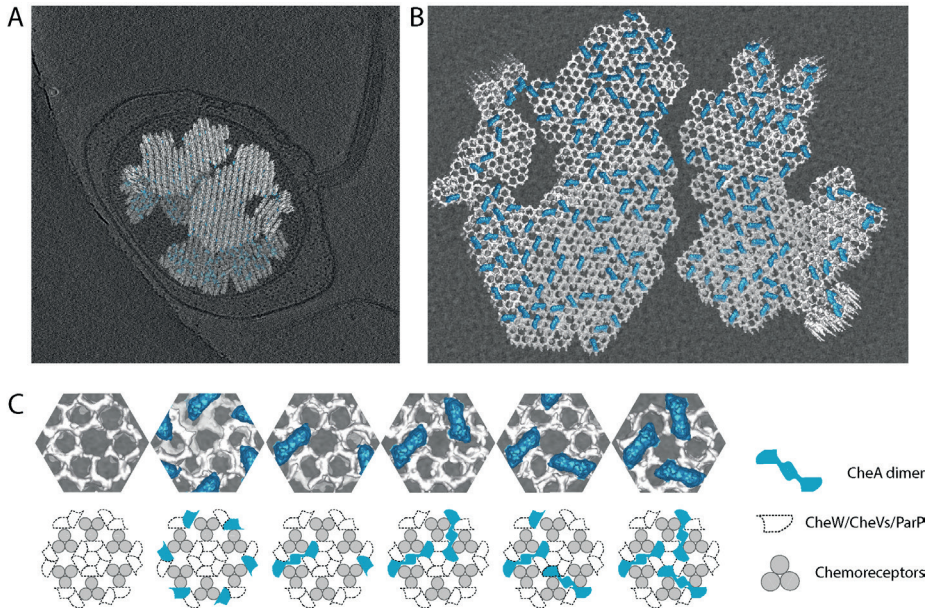


Figure 4. Atlas of a CheA distribution model in the *V. cholerae* F6 arrays. (A) A slice of a *V. cholerae* minicell tomogram where the subtomogram averaging results of chemoreceptors and CheAs are superimposed. (B) An atlas of the baseplate showing the kinase distribution on top of a tomoslice. (C) A selection of receptor hexagons with different CheA occupancies viewed from the bottom (top row), and the corresponding cartoons illustrating the compositions (bottom row).

occupancy and high array component variability determined in a previous proteomic study (102). In our previous study, the exact ratio between baseplate components and the receptors was not studied (102). However, such a ratio can be deduced. Each receptor trimers-of-dimers can provide three possible interfaces at the cytoplasmic tips for binding with any SH3-like domain in the baseplate (47). In *Vibrio*, the baseplate proteins containing SH3-like domain include the P5 domain of CheA, CheW, ParP and CheVs (100, 108, 112). Assuming a 1:1 ratio between receptor dimer and the SH3-like domain candidates, we can estimate the CheA occupancy of the receptor lattice based on the proportion of CheA among the baseplate components. The ratio between CheA-P5 to non-CheA baseplate components was previously reported to be between 1:5 and 1:7(102). This proportion implies that, approximately, one CheA homodimer is expected for two adjacent receptor hexagons. In contrast, three CheA homodimers are present per two adjacent receptor hexagons in *E. coli*.

It is difficult to calculate the exact ratio between receptors and CheAs based on the proportion of different classes after classification result. The receptor trimers-of-dimers naturally form a superlattice in which every two adjacent receptor hexagons

inevitably overlap by sharing two receptor trimers-of-dimers. As a result, a single CheA dimer connecting those two trimers-of-dimers is always shared between two receptor hexagons and thus potentially appears in more than one class in the classification process. Therefore, the percentages of individual classes do not directly reflect the absolute CheA number. In addition, the classification algorithm is not sophisticated enough to categorize all receptor hexagons with all the possible CheA arrangements with an equal certainty. In *E. coli*, receptor hexagons have either 0 or 3 CheA dimers protruding beneath the baseplate. Yet in *V. cholerae*, the receptor hexagons can contain any CheA number between 0 and 3. For the same classification algorithm, it is of lower fidelity distinguishing 3 CheAs and 2 CheAs compared to distinguishing 3 CheAs to no CheA at all. In our analysis, 52% of the receptor hexagons were classified as lacking CheA. This roughly fits with our expectation that at least 1 CheA is shared between 2 neighboring receptor hexagons based on experimentally determined stoichiometry.

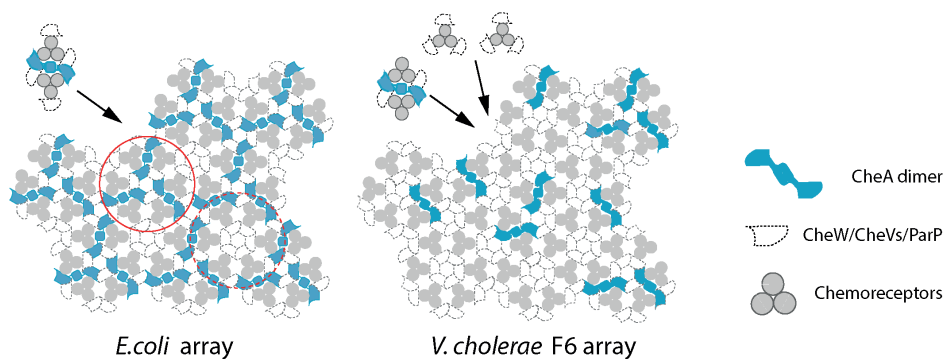


Figure 5. Models of the chemotaxis array assembly between *E. coli* (left) and *V. cholerae* (right). The CheA-filled and CheA-empty rings in *E. coli* are indicated with red circles in solid and dash lines, respectively.

Noticeably, in a few regions of one continuous receptor superlattice, we can see a continuous patch of receptors seemingly lacking CheA completely. However, it is difficult to verify whether this local array patch really completely lacks CheA. Such lack of CheAs is structurally possible, as previous results showed that extensive hexagonally packed receptor arrays could be established even in a total absence of CheA (102). Intriguingly, it is unclear how *V. cholerae* could benefit from recruiting and assembling receptors without assigning sufficient number of kinases for proper chemotaxis function. To our knowledge, CheA is the only known component that is capable of generating the output signal of the chemosensory arrays by converting the signaling information from chemoreceptors into phosphorylation of response regulators. In *E. coli*, the core unit rigidly repeats itself to form an overall ordered receptor lattice and the baseplate in such a way that each receptor trimers-of-dimer always directly communicates with a CheA (Fig. 5). In contrast, in *V. cholerae*, the seemingly random distribution and fewer

number of CheAs in the baseplate means that signals generated by some receptors would have to propagate horizontally in the baseplate for a longer distance before it can reach a nearby kinase (Fig. 5). It is unclear how robust this long distance signaling propagation could be and how it may promote the signaling cooperativity to allow kinase modulation under the collective control of a variety of receptors.

Another possible scenario for CheA-less local regions in the lattice may be due to the fact that certain receptors could prefer to bind to CheVs or ParP and those receptors are under conditional unregulated expression. The attainable resolution by cryo-ET is not sufficient for an unambiguous distinction among CheW, CheV and ParP monomers due to their similar molecular mass. Dimeric ParP (84kDa) has been proposed to integrate in the baseplate to substitute dimeric CheA (112, 146). However, ParP only accounts for 2% of baseplate components according to previous proteomics analysis. Such low abundance means that a substantially larger tomographic dataset would be needed to obtain enough ParPs in order to resolve its dimeric form *in situ*. Additionally, a much-improved resolution would also be needed for visualizing and distinguishing both CheVs and ParPs from CheWs to verify the possible clustering.

Given the universal appearance of the chemoreceptor lattice observed in a wide range of bacteria and archaea so far, the structural diversity in chemosensory arrays could easily be overlooked (51, 55). Yet, we have gradually become aware that different CheA distribution patterns in the baseplate among species is a notable feature of chemosensory arrays. In contrast, the highly conserved structural arrangement of the receptor lattice is present in all motile chemotactic bacteria and archaea examined thus far. Furthermore, *V. cholerae* is capable of assembling three independent chemosensory arrays that all share the same 12 nm spacing hexagonal packing order for the receptor lattice (104, 122). Would the other two arrays (F7 and F9 arrays) share the same kinase distribution pattern as revealed for the F6 arrays in this study? Visualization of CheA in these baseplates might help us understand how different arrays function within one species.

Material and Methods

Strains and cell culture

CheA-free *V. cholerae* was constructed as described previously (102). *V. cholerae* minicell yielding strain was engineered with minCD deletion and the matAB deletion in the genome, which gave a 1 in 20 rate of minicell generation (175). *Vibrio* strains were received as gift from collaborators. For imaging, the *V. cholerae* minicell strain was cultured overnight in LB media at 30° with 200 rpm shaking.

Minicell cryo specimen preparation

Overnight culture of the *V. cholerae* minicells were enriched using sucrose gradient centrifugation. *V. cholerae* culture was first centrifuged at 4,000 rcf for 10 minutes. The pellets were discarded, while the supernatant was further centrifuged at 8,000 rcf for 20 minutes. The supernatant was discarded and the pellets were re-suspended in 2 ml Gelatin Saline Buffer (GSB contains 0.085% NaCl, 0.003% KHPO_4 , 0.006% K_2HPO_4 and 10 $\mu\text{g/ml}$ gelatin at pH 7.7). The cell suspension was then carefully transferred onto 40 ml sucrose gradient (5-30%) GSB. Sucrose gradient was achieved by first dissolving 12 g sucrose in 40m GSB buffer, letting it freeze completely in -20°C and then thaw completely without stirring at 4°C before use. After 45 minutes of spinning at 2,000 rcf, the top 4 ml of cell suspension was collected. The minicell suspension went through another 20 minutes of centrifugation at 21,000 rcf, and the pellets were re-suspended in 20 μl LB media.

Protein A coated, 10-nm gold nanoparticles solution (Utrecht University, The Netherlands) was added into the *V. cholerae* minicells suspension. After brief vortexing, 3 μl aliquots of mixture was transferred onto freshly glow-discharged R2/2, 200 mesh copper Quantifoil grid (Quantifoil Micro Tools). In climate chamber set to 20°C and 95% humidity, the excess liquid was blotted off before the grid was plunge frozen in liquid ethane by Leica EM GP system (Leica Microsystems).

Electron microscopy

Image acquisition was performed on a Titan Krios transmission electron microscope (Thermo Fisher Scientific) operating at 300 kV equipped with a Gatan GIF Quantum K2 Summit detector with a slit width set to 20 eV (Gatan, the United States). Tilt series were collected on minicells showing flagellum clearly attached. SerialEM software package (178) was used for with a bidirectional tilt scheme that covers a tilting range between -60° and 60° starting at 0° with a 2° increment. Defocus was set to a range between -5 to -8 microns. The magnification corresponds to 3.5 \AA/pixel . Images were collected in counted mode with dose fractionation. An accumulative dosage was set to 80 e/\AA^2 for each tilt-series.

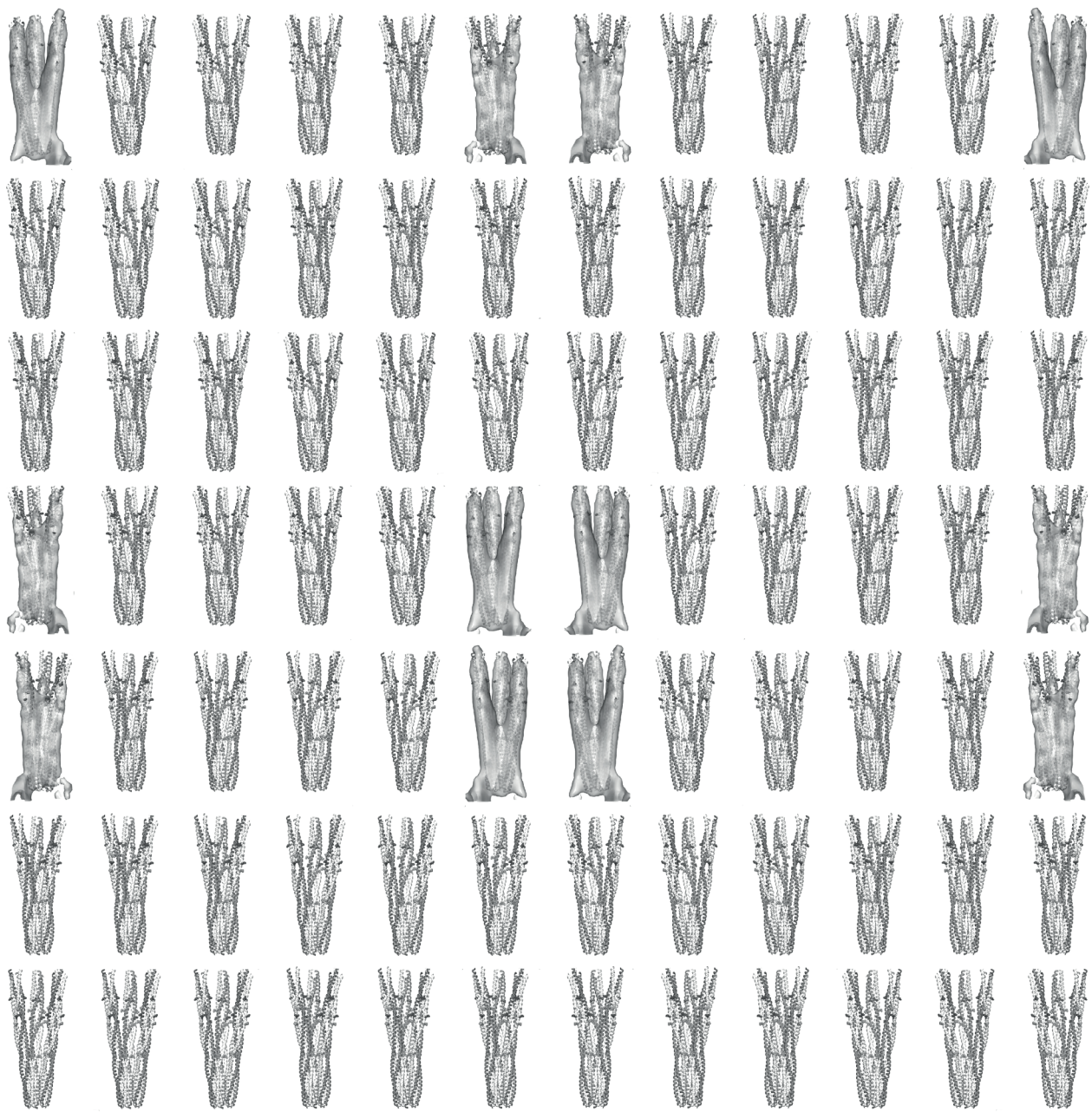
Image processing

Alignframes from IMOD software package (179) was used for motion correction of the frames. Bead-tracking based tilt-series alignment was performed also within IMOD. CTFplotter (157) was used for defocus determination and phase-flip only contrast transfer function correction before tomogram reconstruction. Tomograms were reconstructed with weighted back-projection both with and without using SIRT-like filter of 9 iterations within IMOD, for visualization and subtomogram extraction purpose, respectively.

Dynamo software package was employed for subtomogram alignment averaging and classification analysis of the subtomograms (158, 159, 180). Visual examination first distinguished tomograms that contains *V. cholerae* minicells exhibiting chemosensory arrays. The initial template was generated from manually picked subtomograms from array lattice in the top-view. Then, subtomograms of arrays following the cell curvature and shown in side-view in the tomogram were first modeled as patch of surface and then extracted and aligned to the initial model. After the receptor hexagons were aligned coarsely, multireference alignment was performed for classification purpose with a cylinder mask that loosely enclosed the area beneath the receptor hexagon. While allowing only in-plane rotation, four types of averages were derived from the multireferences alignment representing four different possibilities of CheA distribution in the baseplate.

To visualize the overall kinase distribution beneath the receptor lattice, subboxing centering at CheA was performed for classes exhibiting CheA in the multireference alignment results. The subtomogram containing an individual CheA in the center was further aligned and eliminate duplicates based on their minimum spacing in the lattice. Finally, the isosurfaces of receptor hexagons and the CheAs were separately rendered in 3DMOD and reprojected back into the tomograms with the coordinates and orientation converted from alignment results.

CHAPTER 5



In situ conformational changes of the *Escherichia coli* serine chemoreceptor in different signaling states

This chapter is published as:

Yang W¹, Cassidy CK^{2,3}, Ames P⁴, Diebold CA⁵, Schulten K⁶, Luthey-Schulten Z⁶, Parkinson JS⁴, Briegel A¹ (2019) mBio10(4):e00973-19.

- 1 Institute of Biology, Leiden University, Leiden, The Netherlands
- 2 Department of Biochemistry, University of Oxford, Oxford, United Kingdom
- 3 Department of Physics and Beckman Institute, University of Illinois Urbana-Champaign, Illinois, USA
- 4 School of Biological Sciences, University of Utah, Salt Lake City, Utah, USA
- 5 NeCEN, Leiden University, Leiden The Netherlands
- 6 Department of Chemistry and Center of the Physics of Living Cells, University of Illinois Urbana-Champaign, Urbana, Illinois, USA

Abstract

Tsr, the serine chemoreceptor in *Escherichia coli*, transduces signals from a periplasmic ligand-binding site to its cytoplasmic tip, where it controls the activity of the CheA kinase. To function, Tsr forms trimers-of-homodimers (TODs), which associate *in vivo* with the CheA kinase and CheW coupling protein. Together, these proteins assemble into extended hexagonal arrays. Here, we use cryo-electron tomography (cryo-ET) and molecular dynamics simulation to study Tsr in the context of a near-native array, characterizing its signaling-related conformational changes at both the individual dimer and the trimer level. In particular, we show that individual Tsr dimers within a trimer exhibit asymmetric flexibilities that are a function of the signaling state, highlighting the effect of their different protein interactions at the receptor tips. We further reveal that the dimer compactness of the Tsr trimer changes between signaling states, transitioning at the glycine hinge from a compact conformation in the kinase-OFF state to an expanded conformation in the kinase-ON state. Hence, our results support a crucial role for the glycine hinge: to allow the receptor flexibility necessary to achieve different signaling states while also maintaining structural constraints imposed by the membrane and extended array architecture.

Introduction

Most motile bacteria sense and track chemical gradients in their environment, a behavior called chemotaxis (64, 181). Chemotactic signaling has been extensively studied in the model organism *Escherichia coli* and is especially notable for its high sensitivity, signal amplification, and wide dynamic range (63, 92, 182). Transmembrane chemoreceptors bind ligands in the periplasm and relay signals across the inner membrane to modulate the autophosphorylation activity of the cytoplasmic histidine kinase CheA (38). Attractant stimuli suppress CheA kinase activity, reducing the flux of phosphoryl groups to the cytoplasmic response regulator CheY. Phospho-CheY binds to the flagellar motor and biases its rotation from the default counter-clockwise direction to clockwise. To follow chemoeffector gradients, the chemotaxis system needs to constantly fine-tune its detection sensitivity. Sensory adaptation is made possible by two enzymes: the methyltransferase CheR, which adds methyl groups at specific glutamyl residues in the cytoplasmic portion of chemoreceptors, and the methylesterase CheB, which removes methyl groups from these same sites (183). A fully methylated receptor elicits high CheA activity ("kinase-ON"), while a fully demethylated receptor down-regulates CheA activity ("kinase-OFF") (Fig. 1A).

E. coli chemoreceptor signaling complexes assemble into extended membrane-bound arrays at the cell pole, which integrate signals from thousands of chemoreceptors through a highly ordered baseplate of CheA kinases and CheW coupling proteins. The signaling core unit comprises two receptor trimers-of-dimers (TODs), one CheA homodimer and two CheW proteins (53, 96, 184). This minimal functional unit is also the structural core unit in the array (43, 44, 58). By linking together at specific interfaces between CheA and CheW, core units form a ~12 nm spaced hexagonal array with a receptor trimer at each vertex (Fig. 1B). This hexagonal receptor packing is not only found in *E. coli*, but is likely universal among bacteria and archaea. *E. coli* contains five different chemoreceptors (Tar, Tsr, Tap, Trg and Aer) for sensing a variety of chemicals. Due to their similar physical length and high sequence conservation at their cytoplasmic tips, all five chemoreceptors integrate into a single, continuous receptor array (91, 96, 121, 185).

Tsr, the serine receptor of *E. coli*, is a 551 amino acid protein that spans roughly 31 nm perpendicular to the membrane (44, 46). The receptor homodimers consist of three functional modules that mediate stimulus sensing, input-output control, and kinase control (Fig. 1C) (63, 64). Ligands bind to receptors either directly or indirectly via periplasmic binding proteins (PBPs) at the ligand-binding domain in the periplasm. The signal is then transmitted from the transmembrane domain to the cytoplasmic

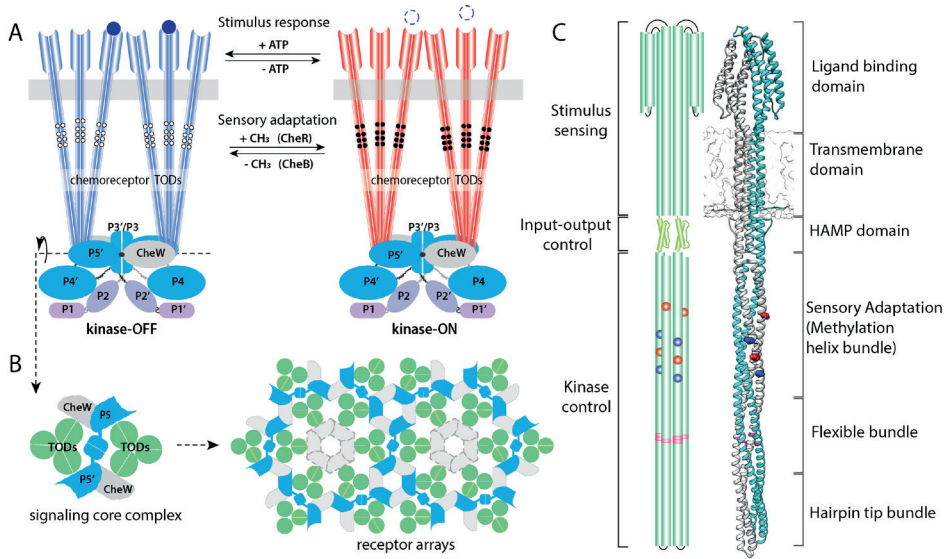


Figure 1. Functional architecture of the *E. coli* chemoreceptor array and the Tsr receptor.

(A) A two-state model of receptor signaling in the core complex, viewed from the side with the cytoplasmic membrane (gray rectangle) near the top. The CheA homodimer and two molecules of CheW bind to the hairpin tips of two receptor trimers. The five CheA domains are designated P1-P5 in one subunit and P1'-P5' in the other. White and black circles indicate the modification states of the receptor methylation sites in the kinase-off (white circles, EEEE sites) and kinase-on (black circles, QQQQ sites) output states. (B) A top-down cross-section through the protein interaction region of the signaling core unit. Core units assemble into an extended receptor array through hexagonal, six membered P5-CheW and CheW-CheW rings. (C) Cartoon and atomic model of the *E. coli* serine receptor (Tsr). The Tsr homodimer consists mainly of alpha-helical segments (cylinders, drawn approximately to scale) organized in four-helix bundles. Four methylation sites are indicated in each subunit, with red indicating glytamy residues (E493 & E304) and blue glutaminy residues (Q297 & Q311) in the wild-type receptor. A fifth Tsr methylation site (E502) is not shown or discussed in the text because it is less critical for sensory adaptation (193). Glycine residues (G340, G341 and G439) located in the middle of the flexible bundle comprise the glycine hinge (highlighted in magenta). Atomic model of the full length Tsr is built based on the structure of HAMP-Tsr fusion (PDB 3ZX6) and the ligand binding domain of Tsr (PDB 3ATP) (194, 195).

portion of the receptor through a five-residue control cable that modulates the HAMP (Histidine, Kinase, Adenylate cyclases, Methyl accepting proteins and Phosphatases) domain (186, 187). The 50-residue HAMP domain forms a parallel four-helix bundle that relays stimulus signals to the kinase control module (119, 188), a continuous anti-parallel, coiled-coil bundle with a hairpin turn at the membrane-distal end. The methylation helix bundle contains the conserved glutamyl residues that are the sites of adaptational modifications by CheR and CheB. In the flexible bundle (91), three conserved glycine residues reside in a plane transecting the coiled-coil axis termed the

‘glycine hinge’ and may enable the bundle to bend (189, 190). The hairpin tip bundle contains the interfaces through which receptor dimers form trimers as well as directly interact with CheA and CheW (91, 99, 191, 192).

Numerous studies have investigated the molecular mechanism of signal transmission in chemoreceptors. A growing body of evidence suggests that kinase activation is likely achieved through dynamic shifts of local conformational alternations in the contiguous helix regions along the receptor (181, 196). The ‘dynamic-bundle model’ suggests the kinase-ON output state corresponds to a dynamic, less tightly packed HAMP domain and a stably packed methylation helix (MH) bundle, while the kinase-OFF output state is characterized by a stable HAMP domain and a dynamic MH bundle (197, 198). In addition, the ‘yin-yang model’ provides a global view on the long-range allosteric interplay of the kinase control module. Here, the kinase-OFF output state is correlated to a loosely packed MH bundle and a tight packing of the proteins in the interaction region at the hairpin tips. In contrast, the kinase-ON output displays a tight, ‘frozen’ packing of the MH bundle and a looser helix packing at the tips (199). Together, these studies suggest that sensory signals are propagated along the receptor through dynamic changes in helix-bundle packing, which toggle the receptor between the kinase-ON and kinase-OFF output states. The receptor coupling to the kinase is likely assisted by one or more specific residues, which are key to the overall stability of the receptor tips as well as for kinase control through receptor-CheA and receptor-CheW interfaces (101, 200, 201).

In this study, we aimed to characterize the signaling conformational changes of Tsr in its near-native cellular context. We combined cryo-electron tomography (cryo-ET) with subtomogram averaging and molecular dynamics simulation to study Tsr in the context of *in vivo* assembled arrays. Our results show that the compactness of receptor dimers within individual receptor trimers changes with signaling state. In the kinase-ON state, receptors in trimers are more splayed than those in kinase-OFF arrays, a feature that is most distinctive around the location of the glycine hinge. We thus propose that the glycine hinge imparts the flexibility necessary for smooth bending in the individual receptors, as well as the changes in compactness at the trimer level. Our results also revealed receptor asymmetry within the trimer that might play a critical role in determining receptor conformational dynamics in the context of the higher-order array lattice.

Results

Improved *E. coli* strains for ECT studies

To maximize homogeneity of receptor arrays, the strains used in this study contained Tsr as their sole chemoreceptor. In addition, all strains lacked the adaptation enzymes CheR and CheB to maintain the Tsr molecules in a uniform modification state. We imaged three Tsr modification variants: Tsr [QQQQ], which mimics the fully methylated, kinase-ON state; Tsr [EEEE], representing a fully unmethylated, kinase-OFF state; and wild-type Tsr [QEQE], which has an intermediate modification and activity state (63). The chemoreceptor arrays in *E. coli* are known to assemble into an ultrastable structure both *in vivo* (54) and *in vitro* (95, 202). This feature has been exploited in previous studies, allowing *in situ* analysis of the assembled array structure in lysed *E. coli* cells, induced either by a phage lysis gene or antibiotic treatment (54, 58, 142). To increase the size and number of chemoreceptor arrays, previous studies overexpressed array components from plasmids (54, 58). Although array sizes increased substantially, the typical native architecture, especially of the baseplate components (CheA and CheW), seemed to be compromised in such strains (58). To increase array sizes in this study, we imaged strains deleted for *flgM*, in which expression of all class III flagellar and chemotaxis genes is de-suppressed about five-fold (203).

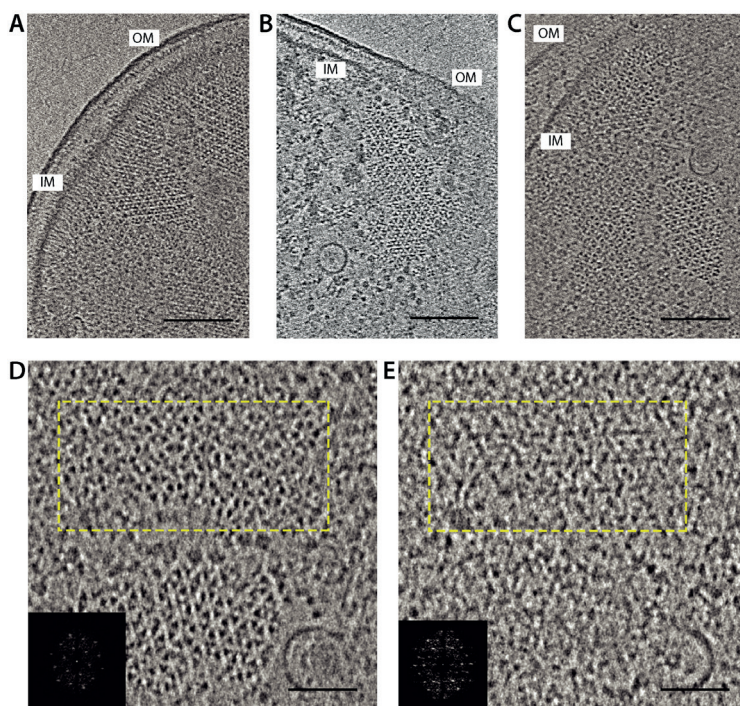


Figure 2. Chemoreceptor arrays imaged by cryo-ET of lysed cells. Panels show 10 nm tomoslices near the cell pole. (A) Tsr-QQQQ (B) Tsr-QEQE (C) Tsr-EEEE. (D) Magnified area of a Tsr-EEEE array (E) Magnified region located 14 nm beneath the array of panel C, showing the ordered CheA distribution in the baseplate. Insets are the power spectra of the regions highlighted by the yellow dashed line in both panels (not to scale). The circular structures in panels B-E are the C-ring of a flagellar motor.

Chemoreceptor arrays maintain native architecture in lysed *E. coli*

Before preserving specimens by vitrification, we treated *E. coli* strains at the early exponential growth phase with penicillin G to induce gentle lysis, thereby releasing cytoplasm and flattening the cells. Tomograms of cell poles containing chemoreceptor arrays revealed average cell thickness under 200 nm compared to unlysed *E. coli* cells that are typically more than 500 nm in width (Fig. S5.1). The receptors retained their well-ordered hexagonal packing, consistent with previous studies (58, 204). However, instead of a single array, we observed several array patches of various sizes, possibly a side effect of lysis treatment on large arrays (Fig. 2A-C). Subtomogram averaging of the receptor hexagons yielded a 12.8 nm regular spacing for arrays in all signaling states. Analysis of the tomographic images also showed that the kinase occupancy at the baseplate was comparable in all strains (Fig. 2 D-E). We conclude that all imaged arrays have the expected native architecture.

Core complex structure in different signaling states

Subtomogram averages were obtained by receptor-based image alignments and subsequent classification based on the occupancy of CheA underneath the receptor hexagons (Fig. 2D & E). We found two major structural classes: receptor hexagons with three CheA dimers bound at their tips and receptor hexagons lacking CheA. We calculated subtomogram averages for the three-CheA hexagon class for each of the Tsr variants. The coupling protein CheW was poorly resolved in all maps due to its relatively small size (18 kDa) and its preferred orientation in the lysed specimens. Nevertheless, the structural information in the receptor region was only slightly affected by the orientation preference (Fig. S5.2). We have, therefore, focused this analysis on structural differences between receptors in different output states, in particular highlighting the EEEE and QQQQ maps. Data for Tsr_QEQE can be found in the supplementary material (Fig. S5.3 & S5.4).

The QQQQ and EEEE receptor hexagon maps were similar in the region near the baseplate (Fig. 3A). In the QQQQ map, the cytoplasmic portion of the receptor from the hairpin tip to just beneath the HAMP domain was clearly visible. In contrast, the HAMP-proximal region of the receptors in the EEEE maps was less well-resolved. These results indicate higher structural stability of the receptor trimers near the baseplate in both ON and OFF output states compared to the membrane-proximal portions of the receptors.

To illustrate state-dependent conformational differences in the core units, we calculated maps for individual core complexes rather than whole hexagons. The resolutions for the core complex maps are 20 Å for QQQQ and 24 Å for EEEE, which are sufficiently similar for tertiary structure comparison (Fig. S5.4). Alignment of the core complexes

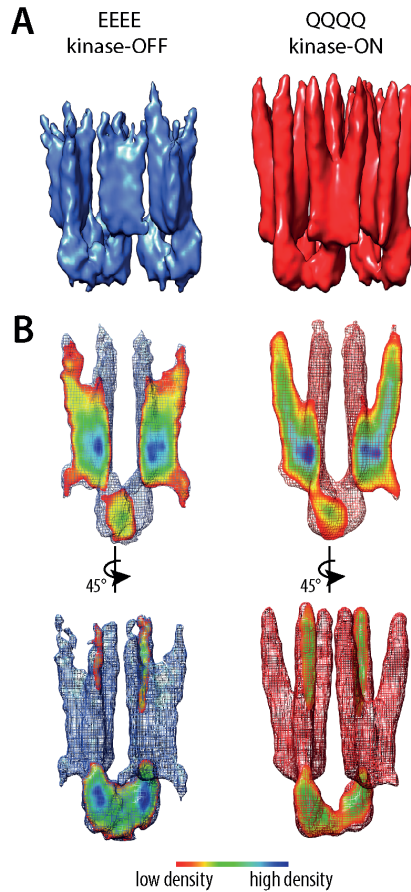


Figure 3. Subtomogram averaging results for Tsr-EEEE and Tsr-QQQQ arrays. (A) Subtomogram average of hexagonal structural units (six Tsr trimers and three CheA dimers). (B) Density maps of chemoreceptor core complexes showing a cross-section through the receptor trimers and the CheA dimer. Mesh surfaces are contoured at 1.5σ . Cross-section colors indicate the volume density. Red corresponds to a low density value, blue to a high density value.

helped to improve alignment of the receptor density, especially for the EEEE map (Fig. 3B). A cross section of the core complex revealed splaying between the receptor dimers in the QQQQ map. The EEEE map also exhibited some receptor splay; however, distinct separation of the individual receptor dimers occurred farther from the hairpin tip. The density distributions of the receptor trimers also exhibited clear differences (Fig. S5.5). The QQQQ maps exhibited strong receptor density extending nearly to the HAMP domain; whereas the EEEE maps exhibited weaker HAMP-proximal density, implying more structural flexibility. The CheA domains P1, P2 and P4 compose a “keel density” protruding beneath the baseplate away from the receptors (54). The size of the keel density appears to be different in the EEEE and QQQQ maps even though the individual

CheA domains were not distinguishable (Fig. 3B). The volume of this keel density was 34% greater in the EEEE map than in the QQQQ map. This difference in keel size is consistent with previously reported results for core complexes with different kinase activities (54). The larger keel of CheA in the kinase-OFF state may be due, at least in part, to an unproductive immobilization of the P1 and P2 domains (205).

Structural differences of receptor trimers

The analysis of the density maps revealed structural differences not only at the core complex level, but also within the receptor trimers. Although receptor dimers interact symmetrically with one another to form a trimer, each receptor molecule also directly interacts with a different component of the base plate (Fig. 4A). Here, we use “AA” to refer to a dimer that interacts with the P5 domain of CheA, “AW” to refer to a dimer that interacts with a CheW bound to CheA-P5, and “WW” to refer to a dimer that interacts with a CheW that has no direct interaction with CheA. We note, however, that in native arrays, not all of the WW dimers may be bound to CheW (141).

The density maps revealed structural asymmetry between the different dimers in a trimer. In the kinase-ON state, the three dimers diverge from the trimer axis at more or less the same location, although the WW dimer diverges a bit closer to the baseplate. The WW dimer also displayed the weakest density of the three dimers. In the kinase-OFF state, the receptors splay farther from the baseplate. We term this observation ‘dimer zipping’ (Fig. 4B) because the dimers form a strong, compact density until they splay apart. After separating from the zipped region, the WW dimer, in particular, shows a decreased density, suggesting a substantial loss of its structural rigidity near the HAMP domain.

The AW and AA dimers also exhibited structural asymmetry in different signaling states. Although a direct, quantitative comparison of the receptor densities in the QQQQ and EEEE maps is challenging, the dimers within each of the maps suggested a subtle structural difference between the AW and AA dimers. In the kinase-ON signaling state, the AA dimer appears to be the most rigid one throughout its full length. In contrast, structural rigidity of the AW dimer seems to extend closer towards the HAMP domain in the kinase-OFF state than in the kinase-ON state. Our data thus reveal signaling-dependent structural or dynamic differences between the members of a receptor trimer of dimers.

Molecular modeling of the Tsr trimer in different signaling states

To gain deeper insight into signaling-related changes in Tsr, we investigated the structural differences observed in our ECT data with molecular modeling. We first assigned atomistic structure to the receptor densities seen in our QQQQ and EEEE

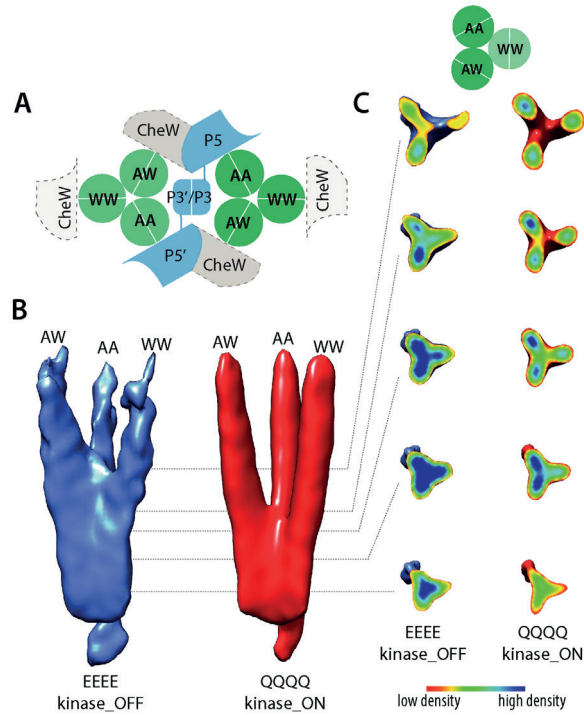


Figure 4. Tsr trimers in different output states. (A) Nomenclature for the three members of a receptor trimer in the signaling core unit. Each Tsr dimer contacts different baseplate components. WW dimers may bind to CheW rings in the array, but are shown in light gray with dashed outlines because their extent of CheW occupancy has not yet been established. (B) Density distribution of the receptor trimer of dimers in kinase-ON and kinase-OFF output states. In both states, the AA and AW dimers exhibit a greater coherence compared to the WW dimer, which exhibited the lowest stability in both maps. (C) The density distribution in different cross-sections of the trimer along the trimer axis, using a color scale from red (low density) to blue (high density).

maps, focusing on a single receptor trimer in each state. Although individual receptor dimers could be clearly distinguished within both maps (Fig. 4), the symmetric nature of the coiled-coil bundles as well as the existence of density corresponding to CheA and CheW prevented the unambiguous docking of lone receptor dimers. Hence, to preserve the known trimer-forming interfaces between receptors during the docking procedure, we first constructed a model of the cytoplasmic portion of the Tsr trimer-of-dimers (residues 259-516) based on existing crystallographic structures (46, 195), using Targeted Molecular Dynamics to reproduce critical inter-receptor contacts at the side-chain level (Fig. S5.6). Next, to extract the regions of density corresponding specifically to the receptor trimers within each map, we docked an existing model of the *Thermotoga maritima* core signaling complex that contains both CheA and CheW (PDB 3JA6) (141). This enabled a reliable interpretation of the baseplate density and

consistent positioning of our Tsr trimer model within each map. We then used Molecular Dynamics Flexible Fitting (MDFF) simulations (131, 206) to refine the conformational overlap between the receptor trimer model and each map. To ensure the robustness of the obtained fits, a total of five MDFF simulations were conducted for each state, giving rise to nearly identical conformations in each case (backbone root-mean-square deviations of 1.23 \pm 0.11 Å for QQQQ and 1.70 \pm 0.10 Å for EEEE).

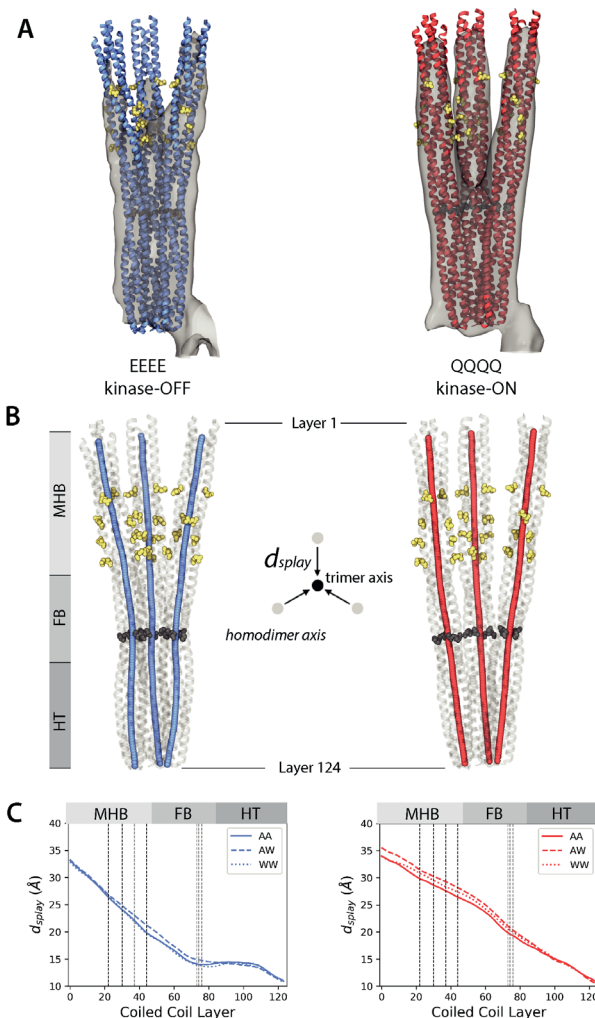


Figure 5. Signal-state differences in trimer compactness. (A) Overlays of the EEEE and QQQQ density maps and representative MDFF-derived Tsr backbone configurations. (B) Central axes of the homodimers in each trimer conformation. Receptor regions are the methylation helix bundle (MHB) and modification sites (yellow atoms), the flexible bundle (FB) and glycine hinge (dark gray atoms) and the hairpin tip (HT). (C) Plots of the distance between the central axis of each homodimer and the symmetry axis of the trimer (d_{splay}). Gray dashed lines denote coiled-coil layers containing the glycine hinge; black dashed lines denote layers containing methylation sites.

Visual inspection of the flexibly-fit conformations confirm that the Tsr trimer is markedly more compact, on average, in the kinase-OFF state than the kinase-ON state (Fig. 5A). To quantify this difference, we decomposed the receptor homodimers from the EEEE and QQQQ trimer models into layers based on coiled-coil packing and computed their central axis along with the symmetry axis of the receptor trimer using TWISTER (Fig. 5B) (207). The layer-by-layer distances between the central axis of each homodimer and the trimer axis reveal a considerable inhomogeneity in the overall splay of the kinase-OFF trimer (Fig 5C, Fig. S5.7). Specifically, whereas the receptors diverge uniformly from the trimer axis uniformly in the kinase-ON state, remaining relatively straight and interacting only at the hairpin tip, they exhibit a pronounced bend in the kinase-OFF state that is centered on the glycine hinge. This bending facilitates the transition from a compact trimer configuration, in which the flexible-bundle regions of the homodimers interact, to one in which they are well separated in the methylation-helix bundle region. Similarly, the comparison of the AA, AW, and WW homodimer axes between states highlights that the overall greatest change in each receptor occurs in the flexible bundle region, with the WW homodimer showing the largest difference of the three (Fig. S5.8). Thus, our simulations provide new molecular insight into Tsr signaling, and highlighting, in particular, the key role of glycine hinge in facilitating the transition between signaling states at the receptor trimer level.

Discussion

Signal state affects stability of the methylation-helix bundle

The present study and numerous previous ECT attempts failed to unveil the structure of full-length chemoreceptors *in situ* (43, 44, 54). Although we were not able to resolve the periplasmic, transmembrane, and HAMP regions of the receptors, we were able to clearly show signaling related conformational differences throughout the kinase control module of Tsr. A particularly distinctive difference was observed in the MH bundle, where the receptors exhibited a more continuous density distribution in the kinase-ON output state compared to the kinase-OFF. This observation agrees with the idea that receptor methylation enhances helix-packing interactions (199, 208). Thus, in our ECT results, receptor density in the MH bundle region was less prominent in the EEEE trimers, suggesting that the adaptation region is structurally more dynamic in the kinase-OFF state. It is worth mentioning that conformational heterogeneity in the kinase-OFF dataset, due to the aforementioned zipping behavior within trimers, may also contribute to the poorly resolved nature of the MH bundle in this state.

Role of the glycine hinge in signal-state switching

We suggest that the state-dependent splayed versus zipped arrangements of

receptors in the flexible bundle region reflect conformational coupling between the MH bundle and the hairpin tip bundle. To our knowledge, these state-dependent structural differences have not been previously observed in imaging studies. Our MDFF analyses show that the flexible bundle region of the receptor exhibits the most dramatic structural differences between signaling states. Glycine residues, located at the center of the flexible bundle region, likely facilitate splaying in the receptor trimer. The functional role of the glycine-hinge in chemoreceptor signaling has been a topic of much speculation and is somewhat controversial. Mutational analyses have shown that sidechain replacements at the glycine hinge residues impair or abrogate chemotaxis ability (189, 209). Moreover, several studies have suggested that the glycine hinge may introduce structural flexibility to the helix bundle, perhaps to allow bending (91, 189). However, previous MD simulations suggested that the glycine hinge did not show a particularly high propensity to bend in receptors out of the array context (200, 210).

A recent cryo-EM study of Tar dimers inserted in nanodiscs showed that receptors bent in two areas under these conditions: just below the HAMP domain and around the glycine hinge (190). That study proposed that bending at the glycine hinge was not related to output state, but instead crucial for facilitating receptor clustering without structural clashes. Yet, that study lacked the structural context of extended arrays, where interactions with CheA and CheW might have substantial effects on receptor structure. Our data indicate that the glycine hinge probably plays a crucial role in facilitating the dimer zipping motions required to mediate the conformational shift between kinase-ON and kinase-OFF output states. Bending at the glycine hinge might, for example, serve to structurally couple changes in helix packing of the MH bundle to signaling changes at the receptor hairpin tip. Further improvements in cryo-EM maps to sub-nanometer resolution should elucidate the mechanism of signal propagation through the glycine hinge.

Stability of the receptor tip in different signaling states

The “yin-yang” hypothesis proposed that dynamic motions of the MH bundle and the protein interaction region at the receptor’s hairpin tip are coupled in opposition (199). Thus, this model predicts that receptor tips might be “frozen” in the OFF state and relatively “molten” in the ON state. Given that the Tsr protein interaction regions appeared quite similar in our kinase-ON and kinase-OFF maps, our ECT data do not support a large dynamic structural difference between the two output states. The tip bundle contains multiple interaction surfaces that maintain the structural integrity of the trimers and the core units. Thus, it seems likely that the tip adopts alternative, stable conformations in both signaling states through structural changes that are small in magnitude. MD simulations of a Tsr dimer proposed a conformational switch at the receptor tip through state-dependent flips in phenylalanine stacking (200). Symmetric

rotations of the dimers about the trimer axis could produce those conformational changes at both the Tsr•P5 and Tsr•CheW interfaces (191). Taking these considerations into account, it is plausible that dimer zipping may promote a reversible twisting motion of receptors at the tip region that triggers a discrete conformational switching between signaling output states.

Effects of receptor signaling state on the kinase

Receptor signaling state influences the mobility of the CheA P1 and P2 domains in core complexes (54). Our data support this conclusion because we found that CheA had a larger keel volume in the kinase-OFF state. In addition, we observed dimer zipping in the baseplate region of receptors in kinase-OFF signaling complexes. Thus, it is plausible that conformational coupling between zipped receptors “freezes” their tightly packed hairpin tips and CheA domains in the kinase-OFF conformational state. In the kinase-ON state, the CheA keel (domains P1, P2 and possibly P4) is less prominent, consistent with a broader range of domain motions. However, we saw no evidence for enhanced mobility of the receptor tips in kinase-ON signaling complexes. We suggest, therefore, that in the kinase-ON state, receptor tips adopt a discrete, structurally stable conformation that frees up CheA domain motions to promote the autophosphorylation reaction. CheA control probably occurs through the receptor/CheW and CheW/CheA. P5 interfaces (101, 191, 201), in turn modulating the CheA•P4 domain (211-213) and possibly the CheA P3/P3’ dimer interface (93).

Our data show that the AW dimer undergoes a change in rigidity between the kinase-ON and OFF state. Asymmetric signaling within receptor trimers has been previously suggested based on the observation that only one dimer within a receptor trimer conveys ligand-binding information to CheA (93). Our results suggest that conformational changes caused by adaptational modification of individual dimers manifest themselves at the level of receptor trimers to modulate kinase control. Thus, although receptor dimers within a trimer undergo asymmetric conformational dynamics depending on their position within signaling complexes, all three dimers play a role in conveying signals to the kinase.

Summary

Despite considerable effort, a complete understanding of the signal transduction events occurring between ligand binding and the regulation of CheA autophosphorylation is still lacking. This can be attributed to the structural complexity of the intact array system, together with the difficulty of analyzing signal transduction events in this context. Our study reveals the conformation dynamics of the *E. coli* Tsr in its native structural context, highlighting global changes in receptor conformation in different signaling states. Our new observations surrounding (1) stability changes in methylation helix

bundle, (2) zipping in flexible bundle region, and (3) asymmetric rigidity changes at the receptor tips collectively reflect that the conformational changes corresponding to signaling states takes place in the whole kinase control module of the receptor rather than a single region. Altogether, our results provide crucial insights into the structural and functional changes in the receptors in the context of native arrays.

Materials and Methods

***E. coli* strains**

E. coli strains used in this study are derivatives of RP437, a wild-type chemotaxis derivative of *E. coli* K12 (214). The strains were previously described (54), which were further modified by introducing a flgM deletion to enhance expression of class III flagellar and chemotaxis genes. Strains are listed as supplementary information table S5.1.

***E. coli* cell lysis and cryo specimen preparation**

E. coli strains were cultured in Tryptone Broth at 30°C with 200 rpm shaking overnight. An overnight culture of *E. coli* was diluted into 50 ml at 1:100 ratio. The diluted culture was then allowed to grow till its OD600 reached 0.2. Then, Penicillin G potassium salt (Carl Ruth, Karlsruhe, Germany) was added to the culture for a working concentration of 2000 UI/ml. After 30 minutes of incubation at 30 degrees, the cells from 1ml culture were collected by centrifugation at 13000 rpm in a 1.5 ml Eppendorf tube. The supernatant was discarded, pellets were resuspended in 10 µl PBS buffer and kept on ice.

The protein A - treated 10nm colloidal gold solution (Cell Microscopy Core, Utrecht University, Utrecht, The Netherlands) was mixed with penicillin treated cells at a 1:10 ratio. After brief vortexing, an aliquot of 3 µl mixture was applied to a freshly plasma-cleaned R2/2, 200mesh copper Quantifoil grids (Quantifoil Micro Tools GmbH, Jena, Germany) and applied to the EM grid in the climate chamber of a Leica EMGP (Leica microsystems, Wetzlar, Germany). The grid was blotted for 1 second from the carbon-facing side of the grid at room temperature (20°C) and 95% humidity. Plunge freezing was carried out in liquid ethane at – 183 °C. Grids were stored in liquid nitrogen until data acquisition.

Cryo-electron tomography

Data acquisition was performed on a Titan Krios transmission electron microscope (Thermo Fisher Scientific (formerly FEI, Hillsboro, OR, USA) operating at 300 kV. Images were recorded with a Gatan K2 Summit direct electron detector (Gatan, Pleasanton, CA) equipped with a GIF-quantum energy filter (Gatan, Pleasanton, CA) operating

with a slit width of 20eV. Images were taken at a nominal magnification of 42,000 x, which corresponded to a pixel size of 3.5Å. The UCSFtomato software package was used for data acquisition with low-dose mode and dose fractionation within a cumulative exposure of 80 e-/Å² (215). All tilt series were collected using a bidirectional tilt scheme which started from 0° to -60° and continued from 0° to 60° tilting with a 2° increment. Defocus was set to -8 µm. A total of 28 tilt series were collected for each strain.

Tomogram reconstruction and subtomogram averaging

IMOD software was used for drift correction and bead-tracking based tilt series alignment (179, 216). CTF estimation and correction were done with CTFPLOTTER and CTFPHASEFLIP implemented in IMOD (157). Tomograms were reconstructed for each tilt series by weighted back projection, both with and without SIRT-like filter equivalent to 9 SIRT iterations. Tomograms reconstructed with the SIRT-like filter provided strong contrast for evaluating array distribution and particle picking and initial template building; while tomograms built by weighted backprojection were used for subtomogram extraction, alignment and averaging.

Subtomogram averaging was done with the Dynamo software package (158, 159, 180). The initial subtomograms were defined as six trimmers of receptor dimers packed in hexagonal order. Subtomograms were manually picked from selected tomograms binned by 2. After coarse alignment based largely on the receptor hexagons, principal component analysis and k-mean based classification was performed based on the CheA occupancy beneath the receptor hexagon. Subtomograms were extracted from tomograms reconstructed by SIRT-like weighted backprojection, since they provided strong contrast for receptor hexagon alignment and CheA-based classification. Each CheA filled hexagon consists of three signaling core units following C3 symmetry. Sub-boxing was carried out to extract the individual core units for further alignment. In addition, an extra round of sub-boxing was done to extract two receptor trimers of dimers from each core unit. For trimer alignment, a soft cylindrical mask was applied to enclose the trimer density. All final maps were calculated from weighted back-projection tomograms. The Fourier shell correlation curves for the core unit maps were calculated with the EMAN2 software package (217). Surface visualization was done using the Chimera software package (218-220). The particle numbers used of averages are listed in supplementary information (Table S5.2).

Model building

A preliminary model of the Tsr trimer-of-dimers was constructed by aligning a copy of PDB 3ZX6 (195), which contains the complete cytoplasmic anti-parallel coiled-coil domain of Tsr (residues 259-516), with the protein-interaction region of each partial homodimer seen in the crystal structure of Tsr trimer of dimers (PDB 1QU7, residues

340-440). Using VMD, the model was then hydrated with TIP3P water molecules and subsequently neutralized and ionized with potassium and chloride ions to a concentration of 150 mM, resulting in a system containing 239,688 atoms. The complete system was then subjected to an energy minimization followed by a 50 ns equilibration simulation in which the protein backbone was harmonically constrained. Targeted Molecular Dynamics was then used to reproduce the inter-homodimer interfaces seen in PDB 1QU7 by minimizing the root-mean-squared-deviation between the backbone and side chain positions in the protein interaction region of the two structures. The resulting model was used as the input structure for subsequent MDFF simulations.

Molecular dynamics simulations

All molecular dynamics simulations were carried out using NAMD 2.12 (221) and the CHARMM36 force field (222). MDFF simulations were performed in the NVT ensemble at 310 K for 20 ns. A scaling factor of 0.15 was used to couple backbone atoms to the MDFF potential. Additional harmonic restraints were applied during fitting to prevent loss of secondary structure. Isothermal conditions were maintained by a Langevin thermostat. The r-RESPA integrator scheme with an integration time step of 2 fs was used along with SHAKE constraints on all hydrogen atoms. Short-range, non-bonded interactions were calculated every 2 fs with a cutoff of 12 Å while long-range electrostatics were evaluated every 6 fs using the particle-mesh-Ewald (PME) method with a grid size of 1 Å.

Accession numbers

The EMDB accession numbers for the subtomogram averages of signaling core unit in different kinase activation level reported in this study are: EMD_4991 (Tsr_EEEE); EMD_4992 (Tsr_QQQQ) and EMD_4993 (Tsr_QEQE).

Supplementary information

Table S5.1. *E. coli* strains used in this study.

Strains	Relevant genotype	Reference
UU2981	(flgM) Δ 494 tsr-QQQQE (tar-cheB) Δ 4346 Δ aer1(trg) Δ 4543	This work
UU2982	(flgM) Δ 494 (tar-cheB) Δ 4346 Δ aer-1(trg) Δ 4543	This work
UU2983	flgM) Δ 494 tsr-EEEE (tar-cheB) Δ 4346 Δ aer-1(trg) Δ 4543	This work

Table S5.1. The particle numbers for calculating the subtomogram averaging results.

	Tsr_QQQQ	Tsr_QEQE	Tsr_EEEE
Receptor hexagon	1251	1011	1118
Signaling core unit	1977	2813	3148
Receptor trimer	3613	5686	6017

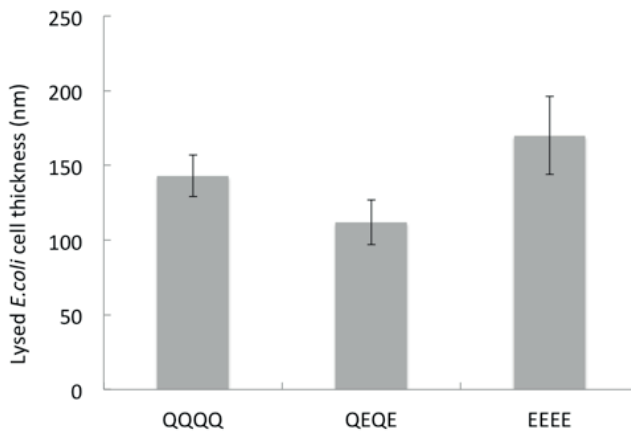


Figure S5.1. The average lysed *E. coli* cell thickness measured from the tomographic data of samples that contained chemoreceptor array. Although in total 30 tomograms were collected for each strain, chemoreceptor complexes for subtomogram averaging were picked from 11, 8 and 7 tomograms for strains expressing Tsr_QQQQ, Tsr_QEQE and Tsr_EEEE, respectively. Student T test ($P < 0.05$) states that cells solely expressing Tsr_QQQQ and Tsr_EEEE are of similar cells thickness after lysed, while cells expressing Tsr_QEQE was on average thinner compared to other groups.

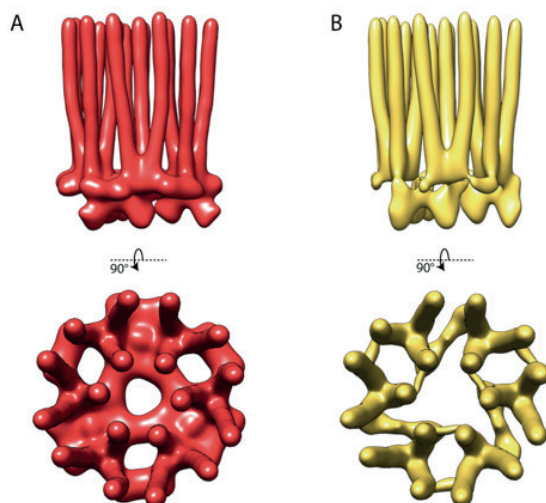


Figure S5.2. Simulation of receptor hexagon maps under impact of a missing cone that corresponds to a -60° to 60° tilt scheme. (A) Density map for the receptor hexagon was built with core compel model (PDF 3JA6). (B) The map of the receptor hexagon with a soft-edged, missing cone shape mask applied in the Fourier space. From both the side and top view, the missing core affect little on the size and shape of the receptor; mainly it causes a severe underrepresentation of the CheWs and a shape distortion in the P4 and P5 domains of CheA.

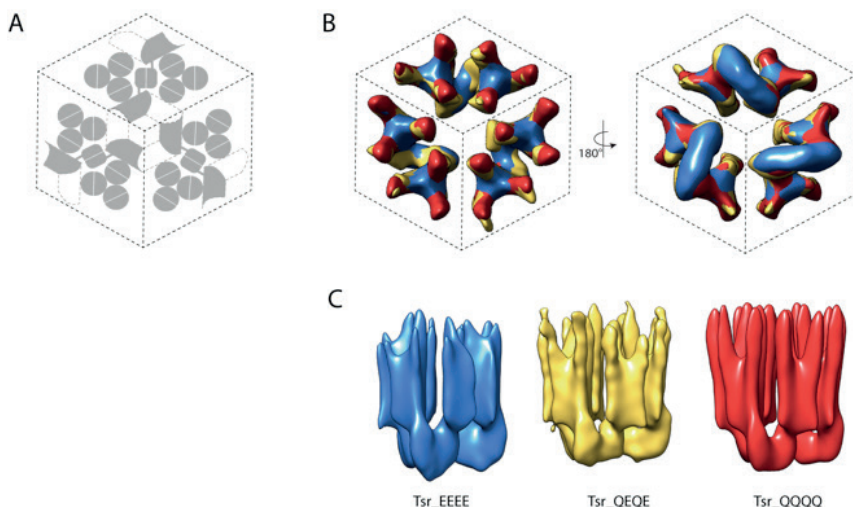


Figure S5.3. Subtomogram averaging of receptors hexagon composed with three dimeric CheA and different receptor variants. (A) Graphic scheme illustrates the native packing order of the ternary complex in the array lattice, in where each hexagon is consisted of three signaling core units. Components in gray, including the receptor trimers and the CheA, are strongly present in the maps; while the coupling protein CheW in the baseplate (color in white) is not resolve due to a combination of its low molecular weight and the

impact from missing cone. (B) Overlay of receptor hexagon for strains containing three Tsr receptor variants show the same native packing order. (C) Averages for three Tsr variants are each low-pass filtered to the same resolution, 25 Å, and present at 1.5 σ level.

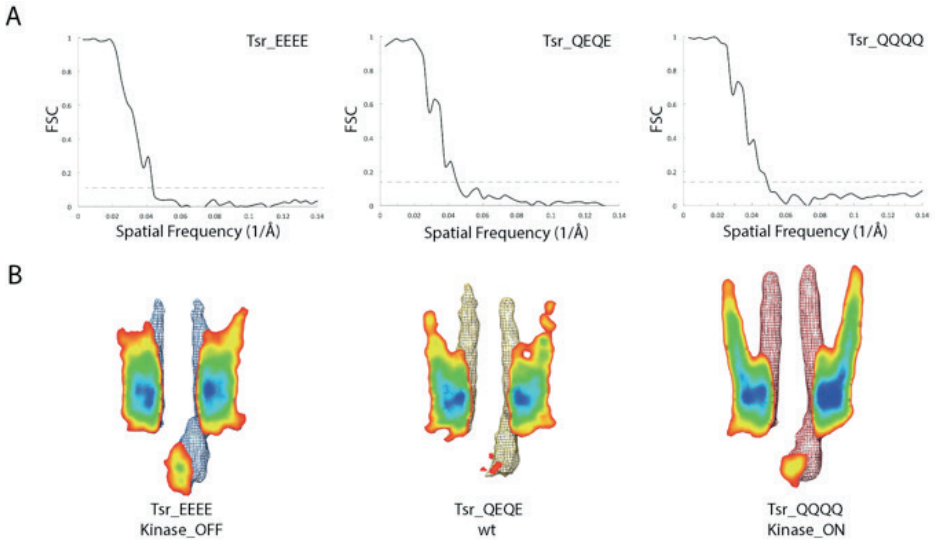


Figure S5.4. The Fourier shell correlation (FSC) curves and the map cross-sections of the signaling core unit averaged for all three selected strains. (A) The FSC curves are plotted for each signaling core unit calculated for the corresponding strains. The dash lines indicate the cutoff at 0.143. All three maps for core units share similar resolutions, which are 20.1 Å, 22.8 Å and 23.6 Å for Tsr_QQQQ, Tsr_QEQE and Tsr_EEEE, respectively. (B) The cross sections of the three maps show the density distribution of the core units. Tsr_QEQE map appears as the intermediate state between the kinase-on and kinase-off biased output states. The surfaces of all maps are rendered at 1.5 σ level in mesh, the cross section is colored according to the volume density value, where the red color correspond to a weaker density than the blue.

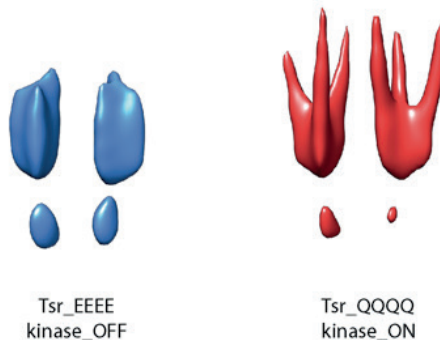


Figure S5.5. The core unit maps for Tsr_EEEE (blue) and Tsr_QQQQ (red) are low-pass filtered to 25 Å and present at 3 σ level. A rigid trimer splay is shown in the kinase-ON state and a zipping in the kinase_OFF state.

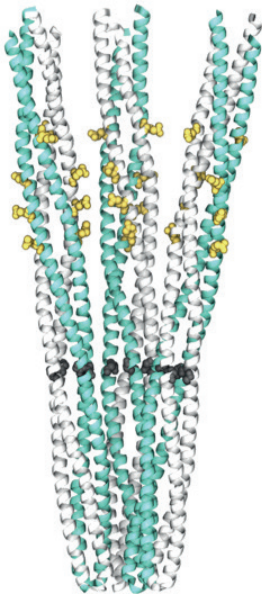


Figure S5.6. Atomistic model of the cytoplasmic Tsr trimer-of-dimers (residues 259-516) used in this study. Individual monomers within each homodimer are colored in teal and white. Methylation sites (residues Q297, E304, Q311, E493) and the glycine hinge (residues G340, G431, G439) are shown with a space-filling representation in yellow and dark-grey, respectively.

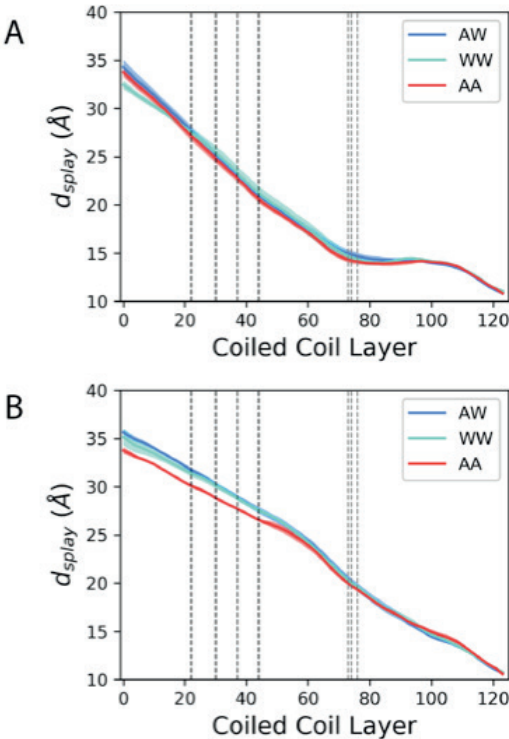


Figure S5.7. (A) Overlay between the central axes of the Tsr_EEEE (red) and Tsr_QQQQ (green) receptor trimer conformations. (B) Plot depicting the distance (Δd) between the central axes of AA, AW, and WW homodimers in the two signaling states, illustrating asymmetry in the individual homodimer fit

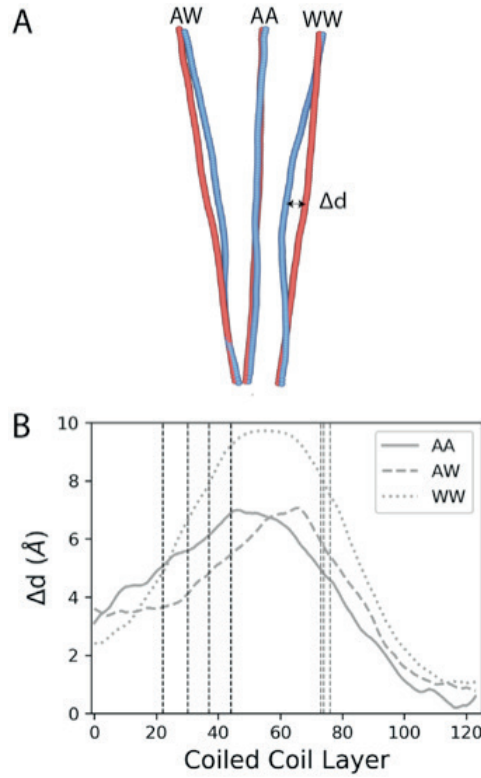
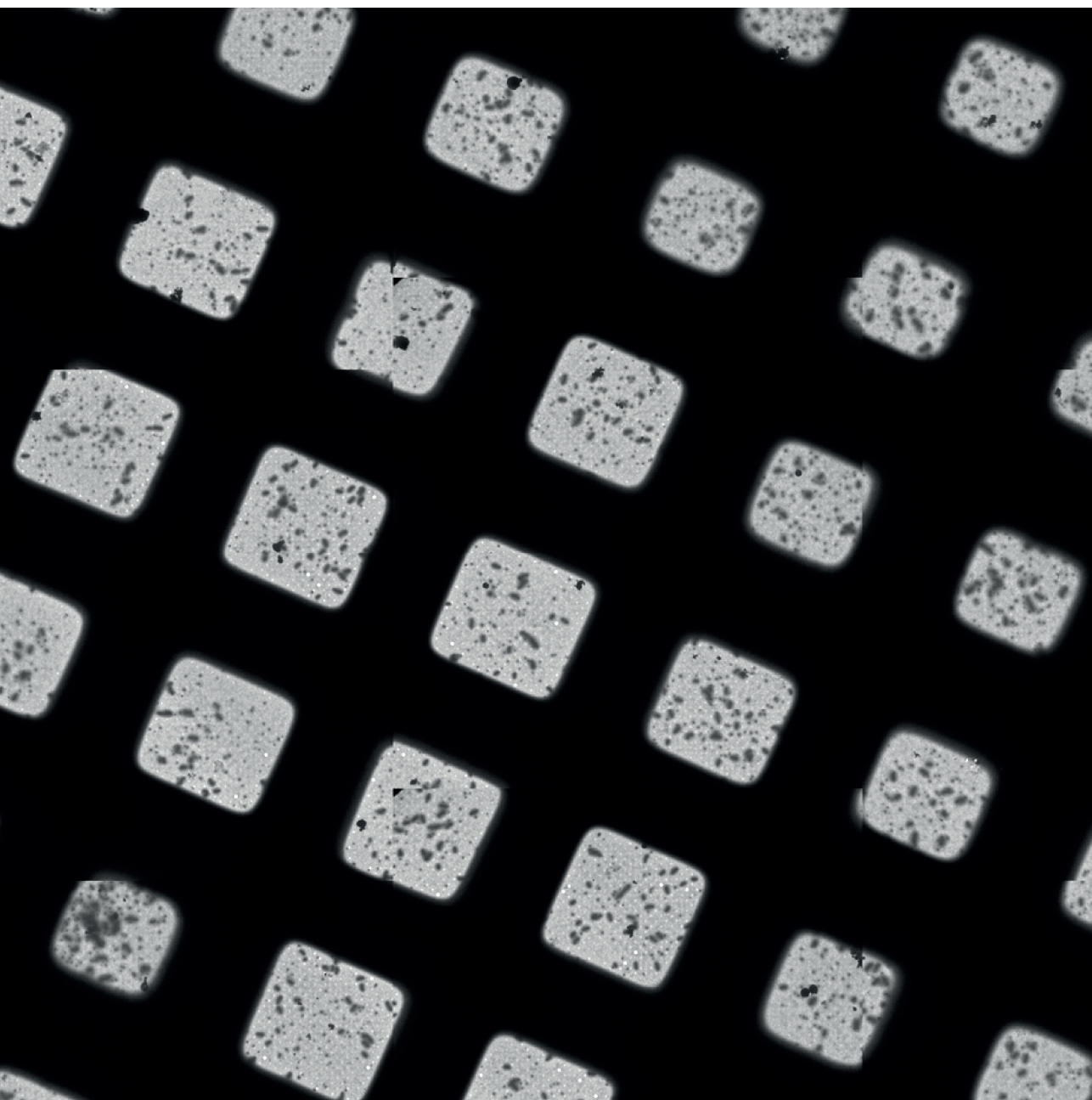


Figure S5.8. (A) Overlay between the central axes of representative EEEE (blue) and QQQQ (red) receptor trimer conformations. The distance (Δd) between each receptor homodimer to the central axis varies for EEEE and QQQQ (Δd). (B) Plot depicting the distance changes (Δd) of the AA, AW, and WW homodimers shown in panel A, which reflects the inhomogeneity of the compactness changes within the receptor trimer.

CHAPTER 6



Use cryo electron microscopy to study the chemo-sensory arrays *in vivo*

This chapter is published as:

Yang W¹, Briegel A¹ (2018) Methods in Molecular Biology 1729:173-185.

1 Institute of Biology, Leiden University, Leiden, The Netherlands

Abstract

Cryo-electron microscopy (cryo-EM) allows the imaging of intact macromolecular complexes in the context of whole cells. The biological samples for cryo-EM are kept in a near-native state by flash freezing, without the need for any additional sample preparation or fixation steps. Since transmission electron microscopy only generates 2-D projections of the samples, the specimen has to be tilted in order to recover its 3-D structural information. This is done by collecting images of the sample with various tilt angles in respect to the electron beam. The acquired tilt series can then be computationally back-projected. This technique is called electron cryotomography (ECT), and has been instrumental to unravel the architecture of chemoreceptor arrays. Here we describe the method of visualizing *in vivo* bacterial chemoreceptor arrays in three main steps: immobilization of bacterial cells on EM grids by plunge-freezing, 2D images acquisition in tilt-series, and 3D tomogram reconstruction.

Introduction

Electron cryotomography (ECT) is a new technique that has recently been used to gain insight into structure and function of macromolecular complexes inside intact cells, such as bacteria, archaea, and even small eukaryotic cells (223, 224). Rapid progress in the development of both hard- and software involved in ECT in the past decade has provided the technological basis necessary for the understanding of structure and function of bacterial chemoreceptor arrays. The arrays were first identified as a cytosolic plate-like structure at cell poles parallel to the membrane, with the perpendicular pillar-like densities of the chemoreceptors spanning into the periplasmic space (42). The plate like density is called the base plate and is comprised of the histidine kinase CheA and the linking protein CheW. Subsequent resolution improvement revealed the hexagonal packing of chemoreceptors above the CheA/CheW base plate with a center-to-center spacing of 12 nm (225). Further improvement was achieved by implementing image correction procedures such as contrast transfer function (CTF) correction and subvolume averaging. This finally revealed the native architecture of the chemoreceptor arrays: they consist of a hexagonally packed lattice of the trimers of receptor dimers networked by rings formed by CheW and the P5 domain of CheA. Neighboring CheA/CheW rings are structurally connected via the dimerization domain P3 of CheA (43, 44). In addition to the abundant structural information, ECT has also provided important insights in understanding the molecular mechanism of receptor signaling and CheA kinase functioning (54, 141).

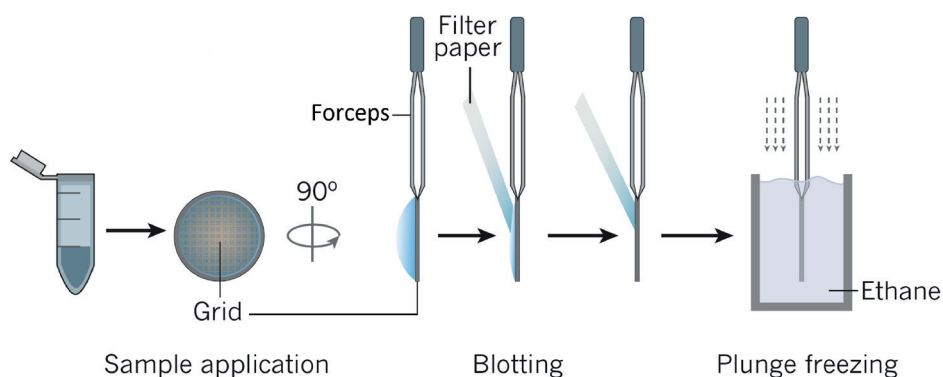


Figure 1. Sample preparation procedure for cryo-EM. A few microliter of bacterial cells suspension mixed with gold nanoparticles is applied to an EM-grid held by forceps. During blotting, filter paper wicks off the excessive liquid and leaves a thin aqueous layer. Plunge freezing fixes this aqueous layer into vitreous ice, while bacterial cells are preserved at their near-native state. Figure is adapted from (226).

ECT allows the study of chemoreceptor arrays in the context of whole cells at near-native state. In order to withstand the high vacuum of the cryogenic electron microscope, the cells have to be embedded in a thin layer of vitreous ice. The most commonly used method to generate thin, vitrified samples is called plunge-freezing (223) (Fig.1). A few microliters of sample (cell culture) is spread out over an EM grid. Excess water is blotted away either manually or automatically with filter paper, and lastly plunged into liquid ethane or ethane/propane mixture that is cooled by liquid nitrogen. This allows freezing of the sample at an extremely high cooling rate (>10000 K/s) and prevents water from crystallizing and instead forms vitreous ice. Thus, cellular structures will be well preserved in a near-native state (227). Vitrified specimens on EM grids need to be transferred and stored below 120 K (-153°C) to maintain the “frozen-hydrated” state (228).

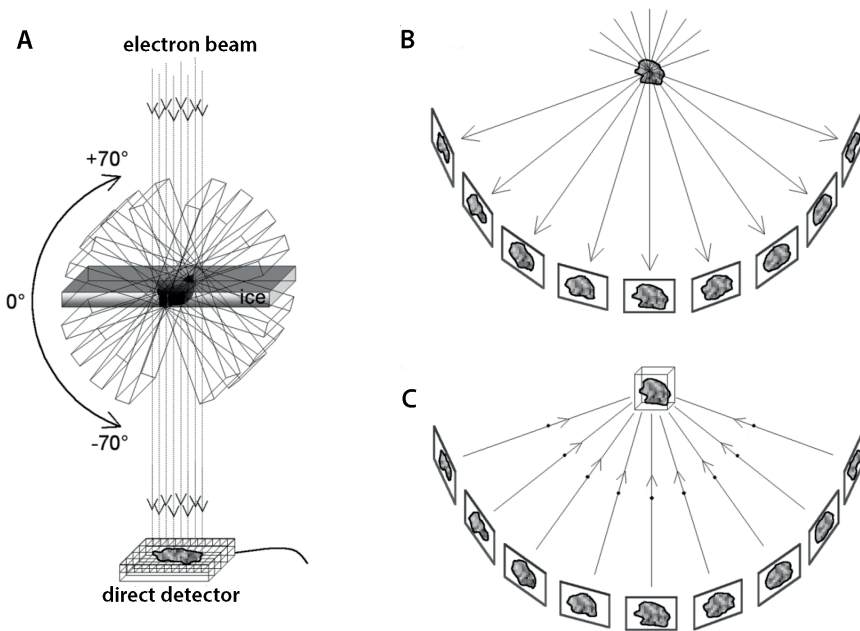


Figure 2. Basic principle of cryotomography. (A) The specimen holder tilts according to the preset tilting scheme around tilting axis perpendicular to the electron beam, and projection images of the same illumination area on the specimen are recorded on the detector. (B) The 2D images captured in a tilt-series correspond to a set of projections of the 3D sample with different tilt angles in respect to the electron beam. (C) After precise alignment, the successive projection images are merged computationally into one density map (referred to as tomogram) correspond to the specimen volume for example by weighted-backprojection (229). Image is adapted from (230).

In order to gain 3D information of the biological specimen, a series of 2D projection images is collected while the sample is incrementally tilted along the axis perpendicular

to the electron beam (Fig. 2) (231). However, this typically requires the acquisition of ~100 or more individual 2D images of the sample. Since the vitrified samples are very electron-dose sensitive, the most critical factor is to limit the total electron dosage in order to allow complete tilt-series acquisition before structures are irreversibly destroyed by radiation damage (232). Based on the type of sample, imaging condition such as total electron dose, magnification, defocus value, tilting range and angular increment, need to be selected carefully for data collection (233, 234).

Once a tilt series of a biological sample is collected, the tomogram (the 3D density map) can be computationally calculated by back-projection of the 2D images into the sample volume. A successful 3D reconstruction relies on precise alignment of the 2D images of the tilt-series. Alignment of the 2D images prior to 3D reconstruction is therefore essential. Instead of cross correlation methods, an alignment based on gold fiducial particles is commonly used, especially in the case of thicker samples such as intact bacterial cells. Here, gold colloidal particles of typically 5-15 nm in diameter are mixed together with the biological sample. These highly electron dense particles are easily visible in the individual 2D images of a tilt series and can be used to align the individual 2D projections (235). Several software packages are available for tomogram reconstruction, either fully automatic or interactive through a graphic user interface. Several different reconstruction schemes are available, such as for example weighted back-projection (229), SIRT (236) or SART (237). In-depth information on these computational methods can be found in the respective publications. Additional data processing steps such as contrast transfer function (CTF) correction (157, 238) and subvolume averaging (239, 240), can also be applied accordingly to obtain higher signal to noise ratio cryo-EM maps to study the structure of chemoreceptor arrays.

While ECT is an important tool for structural studies of molecular machines, the high cost of both, the required specialized equipment as well as the in-depth expertise of the operators, is preventing many laboratories from utilizing this technique. Therefore, this chapter provides methods that focus primarily on cryo-EM sample preparation and evaluation that is essential to generate adequate samples for ECT. The method description below is based on the particular instrument equipped in our lab; adjustment of parameters and condition may be required for alternative instrument setup. Unless your laboratory is a dedicated cryo-EM facility, access to high-end equipment is available at one of several open-access EM facilities worldwide (see note 3). While this chapter provides suggestions for data collection parameters for imaging chemoreceptor arrays, the on-site expert staff of the cryo-EM facility should provide the necessary in-depth advice on proper data acquisition and processing.

Materials

Materials

Quantifoil grids (Cu 200 mesh R2/2; Quantifoil Micro Tools GmbH, Germany)
 Colloidal gold solution (10 nm) (Sigma, St. Louis, MO, USA)
 Bovine Serum Albumin solution (5%) (Sigma, St. Louis, MO, USA)
 Bacterial culture
 Ethane
 Liquid nitrogen

Equipment

Sputter Coater (e.g. Quorum Technologies, UK)
 Leica EM GP immersion freezer (Leica Microsystems, Vienna, Austria) or similar (see Note 1)
 Tecnai Talos G2 (FEI Company, Hillsboro, OR, USA) or similar (see Note 2)
 Cryo-transfer holders (Gatan Inc., Pleasanton, CA, USA)
 Titan Krios (FEI Company, Hillsboro, OR, USA) (see Note 3)

Softwares

FEI Tomography (FEI Company, Hillsboro, OR, USA) (see Note 4)
 IMOD (179, 216) (see Note 5)

Methods

Plunge freezing bacteria cells on EM grids

1. Grow bacteria culture to mid-exponential phase at an OD₆₀₀ above 0.5 (see Note 6).
2. Place EM grids Quantifoil side up, glow discharge under 10⁻² Mbar pressure, at 25 mA current for 45 seconds (see Note 7).
3. For the blotting chamber on Leica freezer, set the temperature to room temperature; set the humidity to 95%; set the temperature of cryogen container to -183 °C.
4. Fill up the liquid nitrogen tank, let the cryogen container cool down to the target temperature; and then fill up cryogen container carefully with ethane (see Note 8).
5. Wait until all parameters set up for the blotting chamber are reached, secure one EM grid with the forceps provided with the plunge freezer and load it into the blotting chamber.
6. Mix 100 µl colloid gold solution with 25 µl 5% BSA solution and vortex briefly; spin down the BSA treated gold nanoparticles at 14,000 rpm for 10 min; discard the supernatant and keep the pellets of colloidal gold for next step.

7. Mix 20 μ l of bacteria culture with the colloidal gold prepared in step 6 briefly on a vortex mixer.
8. Apply 3 μ l cell culture mixture onto the carbon film coated side of the grid.
9. Set blotting time to 1 s and activate auto-plunge; blotting is done on the carbon film side followed by automatic plunging (see Note 9).
10. Transfer the frozen grid from liquid ethane swiftly to a labeled grid box in liquid nitrogen (see Note 10).
11. Screw tight the lid on the grid box and transfer the grid box swiftly to a 50 ml conical tube in nitrogen dewar.
12. Checking the quality of the ice on the grid with the cryogenic microscope operating at 120 kV to evaluate the plunge freezing method (see Note 11) (Fig 3).

Single tilt-series 2D images acquisition

In spite of the fact that different data acquisition softwares have various tilt series set-up schemes, certain parameters are common for visualizing the chemoreceptor arrays.

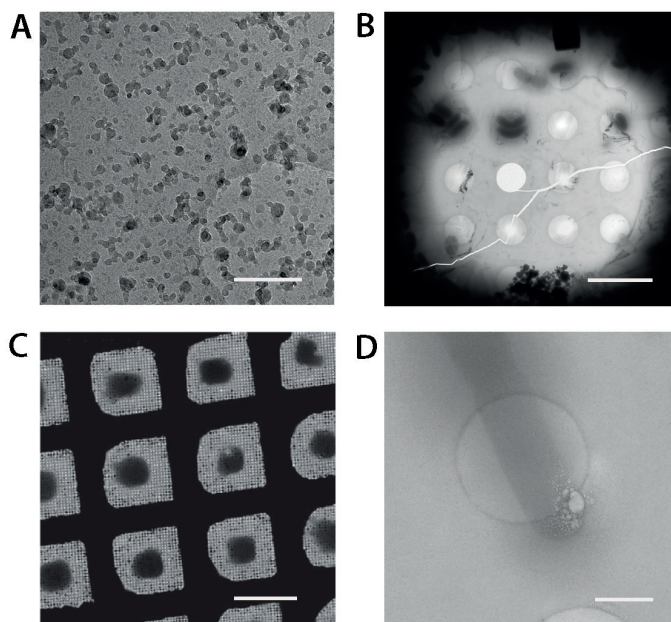


Figure 3. Common problems found on cryo-EM grids due to either contamination, mishandling, glow discharge failure or radiation damage. (A) The dark blobs are usually resulted from contaminants in the liquid ethane. Images is adapted from (241). Scale bar is 250 nm. (B) A mesh square shows a big crack of the carbon film, extensive crystalline ice as indicated by the irregular dark marks and chunks of ice contamination at the bottom of the image. Scale bar is 5 μ m. (C) Failure in proper glow discharging results insufficient hydrophilicity on the grid, which leads to thick ice core in each grid square center. Image is adapted from (242). Scale bar is 100 μ m. (D) The “bubbling” of cellular structures, here for example at an *E. coli* cell pole, is the typical result of radiation damage. Scale bar is 1 μ m.

The general process of acquiring a tilt-series projection is outlined as follow:

1. Examine the loaded grid at low magnification with a low electron dose to find an area with optimal ice thinness; then localize the region of interest. For imaging bacterial chemoreceptors, it is preferred to target cell poles fixed in a hole of the carbon membrane where the sample thickness is minimized (See Note 12) (Fig 4).
2. Set the total electron dosage for single tilt-series as 120 electrons/Å² (See Note 13).
3. Set up the increment, range and imaging scheme for tilting. For chemoreceptor arrays in the context of a native cell, we usually record over an angular range of ±60° with 1° or 2° increment. We typically use a tiling scheme where imaging starts at 0° and continues tilting to one extreme angle, then returns to zero tilt before recording tilting through the other side.
4. Set the defocus to -10 µm.
5. The magnification suitable for imaging chemoreceptor arrays is roughly corresponding to 3.5Å pixel size (see Note 14).
6. Most software for ECT support fully automated tracking and focusing for each tilt angle. For some software, it is important to select an area for tracking and autofocusing along the tilt axis close to the field of view but without overlapping to avoid damaging the data collection area. Depending on the software, camera hardware and the data collection parameters used, it typically takes around 20-60 minutes to collect the data recording for one single-tilt series (see Note 15).

Building tomogram and visualizing chemoreceptor arrays

IMOD is the data processing software package used in our lab. As a widely distributed, well maintained and user-friendly software package, it offers informative description of each program on its website (<http://bio3d.colorado.edu/imod/>). A detailed description on cryo-tilt series data processing is also provided (<http://bio3d.colorado.edu/imod/betaDoc/cryoExample.html>). This open-source software package also allows for CTF correction and provides the option for either SIRT or weighted back-projection to generate the tomographic reconstruction. For subvolume averaging, the PEET software package has been developed by the same research group as IMOD and provides the means to aligning and averaging subvolumes extracted from tomograms (<http://bio3d.colorado.edu/PEET/>). Please note that there are multiple options for tomogram reconstruction and further data processing available (see further examples in Note 5). The tomographic image directly shows the native location and assembly forms of chemoreceptor arrays, and higher resolution cryo EM maps (20-35 Å) can also be obtained with additional data processing (Fig 5).

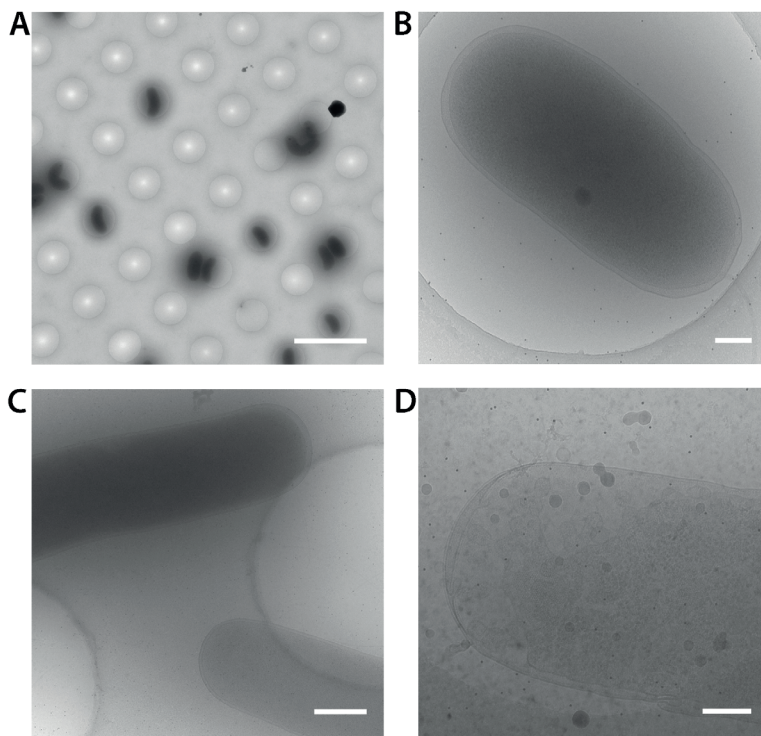


Figure 4. Good cryo-EM specimens for bacteria chemoreceptor arrays study. (A) An ideal ice thickness with abundant *Vibrio cholerae* cells embedded. Scale bar is 5 μm . (B) For small cells ($< 2 \mu\text{m}$ in length) it is easy to find whole cells located in the holes of carbon film. The vitreous ice appears as transparent, and the well-distributed black dots are gold nanoparticles serving as fiducials for images alignment. Scale bar is 200 nm. (C) For large cells, gentle lysis can effectively help to reduce the sample thickness without structurally disturbing the chemoreceptor array. Intact *E. coli* cell on the left appears much darker compared to the lysed cell on the right. Scale bar represents 500 nm. (D) A gently lysed *E. coli* cell in the hole is considerably thinner compared to intact cells, and the ordered pattern of the chemoreceptors can be identified at high magnification. Scale bar is 200 nm.

Notes

1. Other popular choices for commercial automatic plunge freezer include Cryoplunge (Gatan, Inc., Pleasanton, CA, USA) and Vitrobot (FEI Company, Hillsboro, OR, USA). Detailed protocol on how to use the Vitrobot has been described previously (243, 244).
2. A cryo-EM operating at 120 keV and a cryo holder are the basic requirement for assessing the sample quality and visualizing chemoreceptors *in vivo*.
3. Unless your laboratory is a dedicated cryo-EM facility, access to high-end equipment such as TITAN Krios, is available at one of several multi-user EM

- facilities worldwide (245).
4. Automated tilt-series data acquisition schemes for cryo-EM samples have been under fast development, providing the user a wide variety of software packages to choose from. SerialEM (246), TOM (247), UCSF tomography (215), or commercial packages like FEI Tomography (FEI Company, Hillsboro, OR, USA) are a few of the most widely used choices.
 5. There are numerous software packages available for tomogram reconstruction besides of IMOD, such as SPIDER (248), TOM (247), Bsoft (249), Protomo (250), UCSF tomography (215) and Xplore3D (FEI Company, Hillsboro, OR, USA). A complete list of software packages applicable for ECT data collecting and data reconstructing can be found on the website (https://en.wikibooks.org/wiki/Software_Tools_For_Molecular_Microscopy).
 6. One fundamental limitation of this technique is the sample thickness. The vitrified sample has to be thin enough to allow the electrons to pass through the sample. Therefore, samples optimally are less than 500 nm when imaged with 300 keV instrument. Some of the model organisms that are used to study bacterial chemotaxis exceed an ideal cell diameter. Therefore, multiple methods have been developed to effectively reduce the bacterial cells thickness and facilitate the visualization of chemoreceptor arrays. Both antibiotic and lysozyme treatment can lead to cytoplasmic content release with the native structure of arrays preserved (43, 54, 251). Similarly, a phage gene has been engineered into *E. coli*, allowing for controlled inducible lysis to flatten the cells (142). In addition, small and DNA free “minicells” of model organisms are the result of strains with disrupted localization of the cell division machinery. Such cells are ideal candidates for ECT, and were previously used for describing the chemoreceptor array structure (43, 44).
 7. The carbon side of EM grids normally remains hydrophilic within 2 hours after being glow discharged; if grids are not used in time, repeat the glow discharge process.
 8. Wear safety glasses or face shield when using ethane.
 9. 3 μ l cells mixture with 1s blotting time usually yield vitreous ice layer thin enough for imaging; if the volume of the cell mixture is increased, consider extending blotting time accordingly. In addition, sample-specific features like viscosity should also be taken into account for choosing the optimal blotting time in order to achieve ideal ice thickness.
 10. Mishandling of the sample by warming it above 120 K (-153°C) will cause the crystallization of the ice film, which irreversibly damages the specimen; also, exposing the grid to atmospheric moisture results in ice contamination on the surface of the grids.

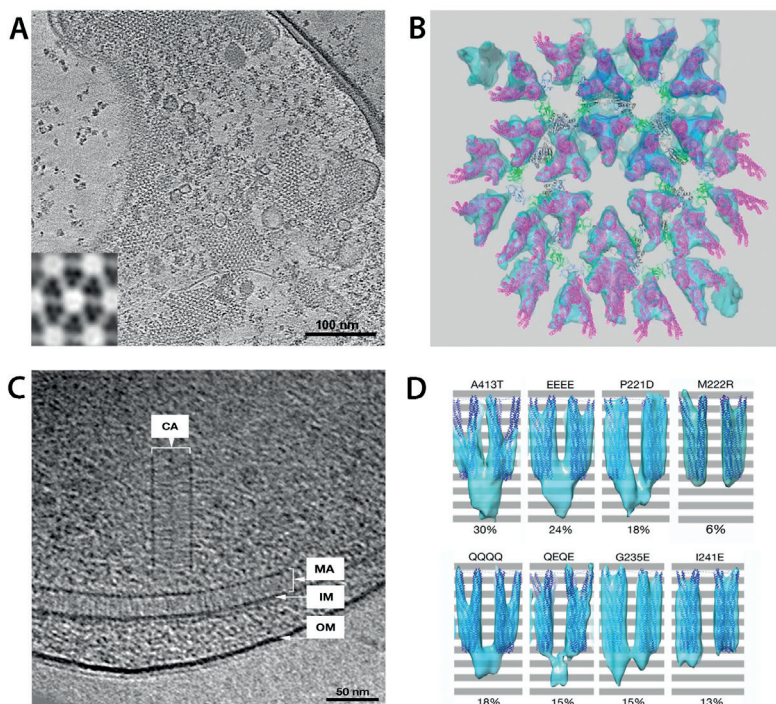


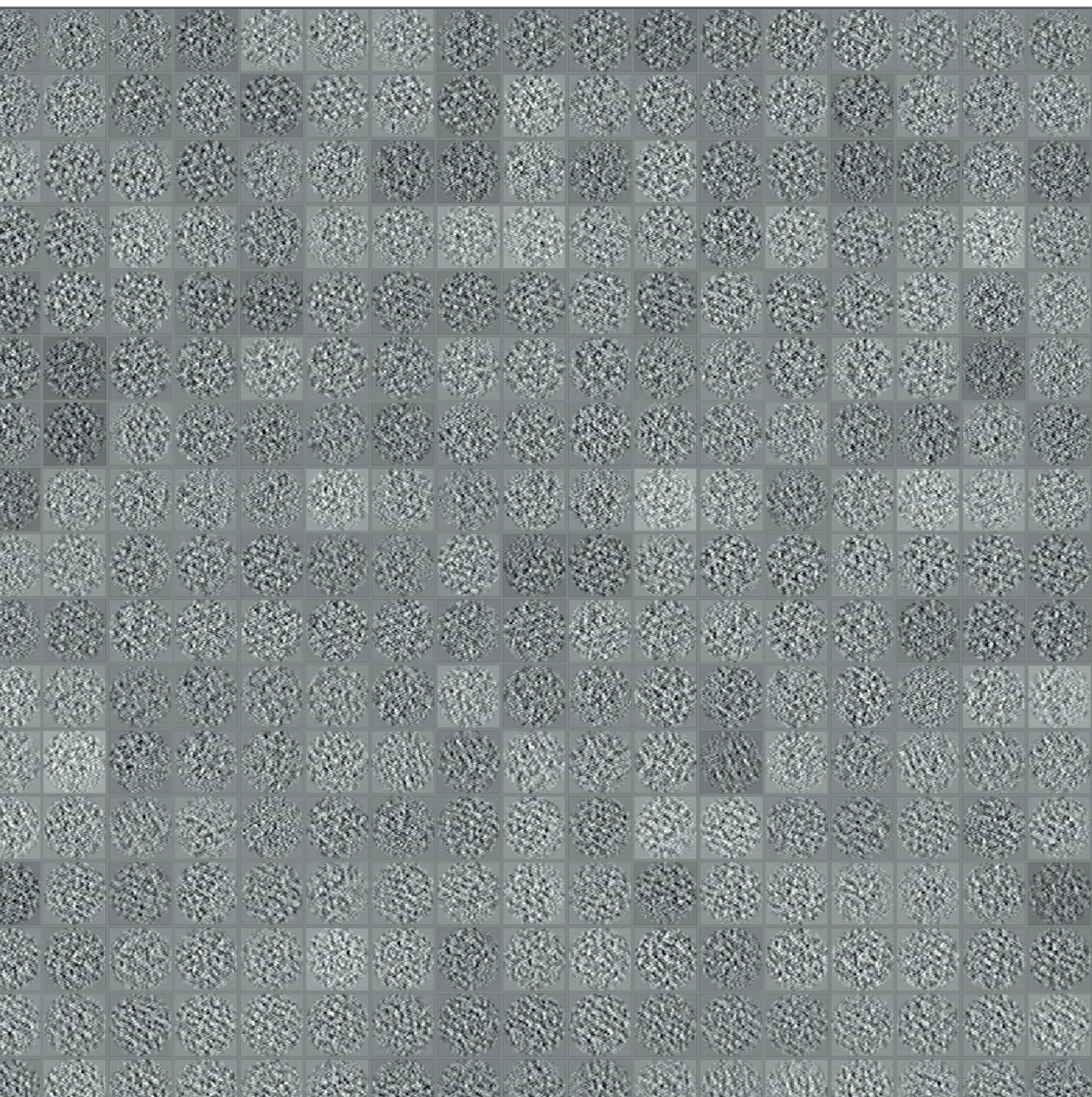
Figure 5. Images generated from cryo-tomography data for chemoreceptor arrays studies. (A) On the left panel, the top view of chemoreceptor arrays is shown in a slice through a tomographic reconstruction of an *E. coli* cell overproducing chemotaxis proteins. Inset shows the hexagonal packing of receptor trimmers. Image is adapted from(58). (B) The cryo-EM map after subvolume averaging allows the docking of the crystal structures of receptors (magenta). The receptors are networked by rings of CheW and CheA (cheW (green), CheA domains P3 (gray), P4 (black) and P5(blue)). Image is adapted from(43). (C) The side view of chemoreceptor arrays can be easily identified in tomograms due to the high electron density “baseplate” structure formed by cheA and cheW. A membrane-bound chemoreceptor array (MA) is parallel to the inner membrane (IM) while a cytoplasmic chemoreceptor array (CA) appears as a “sandwich” structure in *Vibrio Cholerae* with two baseplates on either side. OM: outer membrane. Image is adapted from (105). (D) Subvolume averaging of the tomographic reconstruction of chemoreceptor arrays locked in specific activation states by single point mutations of the receptor reveals that the electron density of the ternary signaling complexes varies in different functioning states. Crystal structures (purple) have been fitted into the EM density map (blue) by Molecular dynamics flexible fitting. Image is adapted from (54).

11. Examination is essential for new specimen; this step is optional for samples where the blotting conditions have been determined previously.
12. Small bacteria, such as *V. cholerae*, can be found lying entirely inside the holes of the carbon film, which is ideal for data collection. Other bacteria can span several holes as well as the carbon film in between due to their extended cell length of several microns or more. Since the chemoreceptor arrays are localized mostly at

the cell pole, pick the cell poles that are trapped in one of the holes.

13. The total dosage depends both on the specimen as well as the desired resolution. Some intact bacterial cell specimens have been shown to tolerate accumulative dosage up to 200 electrons/Å². A more moderate dose of 160 electrons/Å² has been widely used and is a good starting point for initial dose testing. However, these dose values are very high and will impact the finer structural details in your sample. Therefore, when aiming for higher resolution in lysed cell samples, it is suggested to keep the dosage well below 100 electrons/Å².
14. The choice of magnification depends also on the specific detector that is used for data collection.
15. Most software packages support automatic batch tomography for collecting datasets from multiple positions on one grid. In this case, the process of individual tilt-series acquisition remains the same as described previously. In addition, an "atlas" of the whole grid can be recorded at a relatively low magnification for picking target positions for data collection. Batch tomography also requires an additional calibration steps for accurate localization of the targets.

CHAPTER 7



General Discussion

The research field of biology is an ever-growing collection of knowledge built on the observation of what living things look like and how they function. It has been 127 years since bacterial chemotaxis was first described and we are still searching for answers for two questions, A) what do chemosensory arrays look like and B) how does signal transduction and kinase control work (2, 64). Instead of using traditional methods to understand chemotaxis behavior, such as observing “rings on agar plates” and “bands in capillary tubes”, we are now utilizing direct imaging methods to understand the system on a molecular level. Here we apply structural techniques with a high-resolution limit to describe the possible conformational changes in chemoreceptors and the CheA kinase during signal transduction and activation, respectively. The questions about this system have evolved over time, and so have the probes we use to answer them. The studies presented in this thesis, together with numerous other studies published in the past two decades, clearly demonstrate that the method of cryo-electron tomography has provided unprecedented insight into the structure and function of chemoreceptor arrays.

The characterization of biological objects and the understanding of biological events are frequently limited by our ability to see them directly. Cryo-ET is a powerful tool that allows for the visualization of objects in three dimensions in their near-native context (252, 253). Although the basic concept of the 3D reconstruction from 2D projections was established in 1968, the technique has gained exponential popularity in the last two decades after numerous theoretical and experimental limitations in its practical application have been overcome (254-256). Among multiple applications of cryo-ET in life sciences, studies focusing on resolving the molecular architecture of complex macromolecular assemblies have been particularly successful. The bacterial chemosensory array is one such case where cryo-ET studies led to groundbreaking discoveries. Ever since the molecular architecture was discovered in 2012, new insights were continuously gained to produce a better understanding of how chemosensory arrays function on a molecular level and how chemosensory arrays have evolved to generate structural diversity across species (60). All the studies presented in this thesis rely substantially on applying cryo-ET and subtomogram averaging to characterize the chemosensory arrays either in different functional states (**Chapter 5**) or in different bacteria other than the model organism *E. coli* (**Chapter 2-4**). The main scientific observations and conclusions regarding chemosensory arrays have been discussed in the individual chapters. Here, I will discuss the cryo-ET technique itself as well as its shortcomings and limitations that currently pose as obstacles. In turn, this will hopefully help to assess whether cryo-ET can be further exploited and improved for future bacterial chemotaxis studies.

One of the fundamental cryo-ET limitations that hinder visualization of the chemosensory arrays directly at the molecular, or even atomic, level lies in the sample thickness (**Chapter 6**). Even though chemosensory arrays are predicted to commonly exist in motile bacteria, the average cell diameters vary greatly between species. Different cell morphologies such as spherical, rod-shaped or spiral shaped cells differ drastically in diameter and typically range between 0.25 to 2 microns. Among them, only a few bacteria are naturally thin enough to allow cryo-ET imaging for structural analysis of the chemosensory arrays located at the cell pole (42, 50, 51, 55, 225). To overcome the size limitation, various approaches have been applied to make the bacterial cells thinner. For example, several detailed descriptions of the chemosensory arrays at the molecular level were derived from imaging the *E. coli* minicells (43, 44). This approach is still widely used, for example in the latest structural characterization of the chemosensory arrays in *E. coli* (177). An alternative approach to address the thickness issue is to introduce gentle lysis so that after releasing the cytoplasmic content the thickness of cells drastically decreases in the cryo-specimen (54, 58, 59).

Noticeably, reflected in the recent studies, there are a few significant differences between using the lysis treatment and using minicells (**Chapter 4 & 5**). It has been reported that the chemoreceptor lattice in *E. coli* is generally well preserved in lysed cells. However, it has been observed in many studies with the lysis method that instead of one extended receptor lattice per cell, smaller patches of receptor lattice are dominant. In addition, the chemosensory arrays imaged from a severely lysed cell usually shows a loss of packing order towards the membrane-proximal ends of the receptors with no detectable pattern at the periplasmic domains of the receptors. Conversely, in the subtomogram averaging results of arrays from intact minicells, it has been shown that the hexagonal pattern can be detected throughout the full length of the cytoplasmic domain of the receptors and even for the periplasmic domains (177). Together, this implies that although the native architecture of the baseplate is preserved in both ways, the compactness of the receptor lattice is still susceptible to the changes of the geometry of the inner membrane, particularly for the membrane-proximal ends of the arrays. Because of the much-reduced diameter, the inner membrane of a minicell usually exhibits a much more extreme curvature compared to the cell pole of native wild type cells. As a result, it is plausible that the membrane-proximal ends of the receptors splay out more readily and are less likely to have the same level of likelihood to interact with each other. In contrast, lysis treatment is aimed to flatten the cell so that the majority of the inner membrane appears to resemble more or less a 2D sheet. In other words, the curvature of the inner membrane is much reduced so that the possible interaction among the membrane-distal ends of the receptors is encouraged. This geometry difference of the inner membrane is likely to have an impact on the compactness on the membrane-bound chemoreceptor lattice in the averaging results.

Since the receptor lattice is tethered into the hexagonal pattern by the protein network at the baseplate, the compactness of the receptor lattice is likely to exhibit significant changes at its membrane-distal ends. Indeed, the ~ 26 nm distance of the membrane-spanning region of receptor could allow the chemosensory arrays to tolerate a range of packing compactness at the membrane-proximal ends of the receptor lattice. However, such a tolerance of the structural plasticity still depends on baseplate architecture that tethers the receptor lattice in place.

Besides changes to the sample itself, generating minicells or introducing lysis also results in differences in how to process the different data. For the most ideal lysis results, the cell envelope will be completely flattened and preserved as a sheet oriented perpendicular to the electron beam. Due to the limited image sampling range of cryo-ET, this would readily cause the majority of the subtomograms to exhibit a strong preference of the orientation. In contrast, minicells largely preserve the curvature of the membrane and the chemosensory arrays attaching to it. Thus, imaging minicells offers a higher chance of resulting in a homogeneous spatial sampling of the chemosensory arrays compared to imaging the lysed cells. The sampling differences may strongly influence sub-tomogram averaging (STA) data processing and results. An averaged density map generated mainly, if not exclusively, from receptors lattice parallel to the electron beam direction will reflect the incomplete sampling perpendicular to the lattice plane. The most obvious defects in the EM maps from arrays with such preferred orientation is an artificial elongation of the receptors and severely underrepresented baseplate components. This is particularly problematic for resolving the baseplate components in the arrays. Despite this drawback, averages from flat arrays have proven to be most sensitive to capture structural differences in the packing order of the receptor lattice.

The sample thickness is a universal bottleneck for achieving a higher resolution of biological structures *in situ*. The most informative model building for the chemosensory arrays has therefore been based on the cryo-ET studies of a recombinant chemosensory array sample *in vitro* (45). For the vast majority of questions remaining for the chemosensory complex structure, an atomic resolution structural description is urgently needed. For example, we still need to understand how exactly the receptor binds to the kinase and the coupling protein, and how it controls CheA enzymatic activity. With the current imaging and image analysis technique, it is unlikely that minicells or the lysis treatment would be sufficient to offer samples that permit a resolution needed to answer these questions. Instead, single particle analysis would be a more suitable tool to address this issue if ternary complex comprising chemoreceptor trimers-of-dimers, kinase CheA and CheW could be engineered and proven suitable for cryo-EM imaging (205). An atomic-resolution description of the binding interfaces within such a complex, as well as revealing the spatial arrangement of different domains within the

kinase CheA, would undoubtedly be a major milestone towards understanding signal transduction in chemotaxis (257).

In the meantime, cryo-ET has its unparalleled advantages in exploring the diversity of the chemosensory arrays by imaging them *in situ* in a variety of bacteria. This undoubtedly broadens our understanding and appreciation of diversity of the chemosensory system (**Chapter 2**). Given that the chemoreceptor lattice is one of the most frequently observed macromolecular machines in the tomographic database ETDB (<https://etdb.caltech.edu>) of bacterial cells, there is a rich abundance of image data openly available for analyzing the appearance of the chemosensory arrays (258). The current consensus still stands that the hexagonal packing of the receptors in the chemotaxis arrays is universal in bacteria and archae (51, 55). However, a potential structural diversity may have been overlooked so far.

Functional studies have put a substantial amount of effort in illustrating a “vertical” signal transduction mechanism that is proposed occur through conformational changes passing through the receptor and propagating to the kinase and coupling protein. Meanwhile, the “horizontal” signal transduction, which has been less extensively characterized, is proposed to take place across the baseplate through long-distance allosteric dynamics in the coupling protein and kinase networks. This type of horizontal signal transduction is thought to support signal amplification and signal cooperation. This implies that the chemosensory arrays function not only as a nose, but also as a brain that evaluates different input signals to ultimately control swimming trajectory. In order to understand the nature of this horizontal signaling transduction, the kinase distribution and the molecular architecture of the baseplate are crucially relevant. Emerging research suggests that this distribution is likely to be species-dependent. This is in contrast to the packing order of the chemoreceptor lattice that continues to be a universal feature.

Aside from the number and arrangement of kinase proteins in the array, compositional diversity in the baseplate commonly exists in bacteria outside *E. coli*. In this model organism, which represents the most extensively investigated system among all bacteria, the ternary signaling core unit might just be the simplest case (**Chapter 3**). CheV, a hybrid protein containing a CheW-like domain, can substitute for CheW in the chemosensory arrays. Although not as widely distributed as CheW in the known genomes of bacteria and archaea, in some bacterial species it can even function as the only coupling protein in the chemotaxis system (70, 91, 108, 110, 259, 260). Studies in *V. cholerae* have shown that, in addition to CheV, ParP is another alternative coupling protein that is directly involved in chemosensory array formation and localization (112, 146).

Such discoveries of compositional diversity in the baseplate are inspiring for a further illustration of alternative molecular architecture of the chemosensory arrays other than arrays in *E. coli*. Yet, precisely distinguishing the different components in the baseplate can be a formidable task. To identify a structure of interest, particularly a specific protein, has always been a major challenge with cellular tomography. So far, there is not a universally applicable EM-visible tag that can readily serve as an indicator similar to a fluorescent tag for light microscopy. Immunolabelling using gold-conjugated antibodies could work for binding to proteins exposed on the cell surface or restricted to the section surfaces, but such labels could not reliably access the baseplate in the cytoplasm without extensive cell lysis. A few attempts have been made to design cloneable, protein-specific, electron-dense tags, among which is the ion-loaded ferritin-based label that was tested on chemosensory arrays in *E. coli* (261-263). Yet, instead of being fused to any protein component that directly integrates into the chemosensory arrays, the ferritin label was fused to the CheY protein that co-localizes with arrays through association with kinase CheA. Given the relatively large size of the ferritin label (~ 12 nm), it is hard to imagine that the chemosensory arrays can be efficiently or correctly assembled when either CheV or ParP proteins are fused with such a label. On the other hand, tags with a significantly smaller size might not perturb the local cellular environment but might be difficult to recognize in cellular tomograms. Such labeling would eventually suffer from low fidelity and efficiency, in particular if the fused protein (for example ParP) is predicted to be sparse by nature.

In the absence of a reliable tag, an alternative approach for identifying components in supermolecular machinery *in situ* with cellular tomography data is to compare STA maps derived from a set of mutant strains that each has a single component of the structure of interest knocked out. This method has proven to be powerful through numerous studies that revealed for example the molecular architecture of the bacterial secretion system (264, 265). However, this approach would not be equally effective when applied to identify CheV or ParP in the chemosensory arrays. Since CheV, ParP, CheW, and their homologs all share the SH3-domain-like topology, they are all predicted to be capable of serving as scaffolding proteins in the baseplate. In fact, it has been shown through fluorescence microscopy studies that CheV2, which does not normally integrate into arrays in *V. cholerae* under standard growth conditions, increasingly localizes with the F6 arrays in the absence of CheA (102). Thus, in arrays with a high degree of variability in the baseplate, mutations can be easily overcome by substitution. In contrast, overexpressing either CheW or deletion of CheA in *E. coli*, where there is little variability in the baseplate, severely impairs array assembly (266). In short, it is not feasible to identify some components in the baseplate by mapping the missing density in different STA maps.

Would it be possible to distinguish the baseplate components exclusively through *in silico* analyses, namely based on the classification during the STA analysis (**Chapter 4**)? The cellular tomographic image provides unprecedented structural information that is unfortunately accompanied by an enormous amount of noise. This low signal to noise ratio impedes a reliable interpretation of the structure of interest in the tomographic data directly. Low signal to noise ratio also hinders the accuracy of defocus determination and the precision of subunit position and orientation in the STA alignment, which eventually limits the attainable resolution in final EM maps. The implementation of dose-symmetric tilt scheme and accurate 3D contrast transfer function correction will be an essential step to an overall improvement of attainable resolution in the STA reconstruction (267, 268). This will be true for various samples including chemosensory arrays. Additionally, using a more sophisticated classification algorithm will also improve the achievable resolution. For example, a new algorithm has recently been developed that has been tailored to distinguish the structural differences of 3D maps derived from STA analysis (269, 270). With those technical developments, identifying structures from cryo-ET data *in silico* is becoming more realistic (271-274). However, the successful applications of such analyses are still rather rare and limited to protein complexes with the size and abundance at a similar level of ribosomes. In contrast, distinguishing the proteins located in the baseplate of *V. cholerae*, such as CheV (36kDa) and ParP (42kDa), from CheW (18kDa) would be a formidable task due to their small and similar size. Not only do the sizes of the CheV and ParP present a challenge for analysis, but in addition both proteins are also extremely sparse in the arrays. It is difficult to predict what amount of tomographic data would be required to provide sufficient repeats so that the classification results hold fidelity. The sparseness of such proteins poses a difficulty for applying the correlative light electron microscope approach, given that it would be a challenge for reaching both the fluorescent detection level and the resolution required for the localization accuracy. Altogether, although cryo-ET and STA are progressing towards a molecule-based cellular landscape of macromolecular complexes with their native spatial coordinates, directly identifying chemotaxis proteins *in silico* for the baseplate is unlikely to be feasible in the foreseeable future.

Last but not least, although all biological subjects are inherently dynamic, the sample preparation of cryo-ET captures only a single time point of any given biological process. In other words, cryo-ET fundamentally acquires static 3D snapshots instead of recording biological events in time. In cases where the biological processes of interest occur slowly, the different specimens frozen at the same time point could readily be captured in different stages of such a biological process. By imaging a sufficient amount of different specimens, it is feasible to eventually assembly all the snapshots along the timeline. This would allow for the description of the entire biological process

of interest even though the observation is not carried out strictly on a single specimen. However, the heterogeneities among the specimens could also bring ambiguity into the interpretation of the cryo-ET observation. The bacterial flagellar motors can be used as an example for such a case. In stationary phase cells of gamma-proteobacteria, cryo-ET of the cells reveals incomplete motor structures called 'relics' that are embedded in the cell envelopes. When judged solely from the tomographic data, it is impossible to distinguish whether a relic is an intermediate structure before a flagellar motor is fully assembled or the remaining structure after the flagella has been ejected from the motor (20, 275).

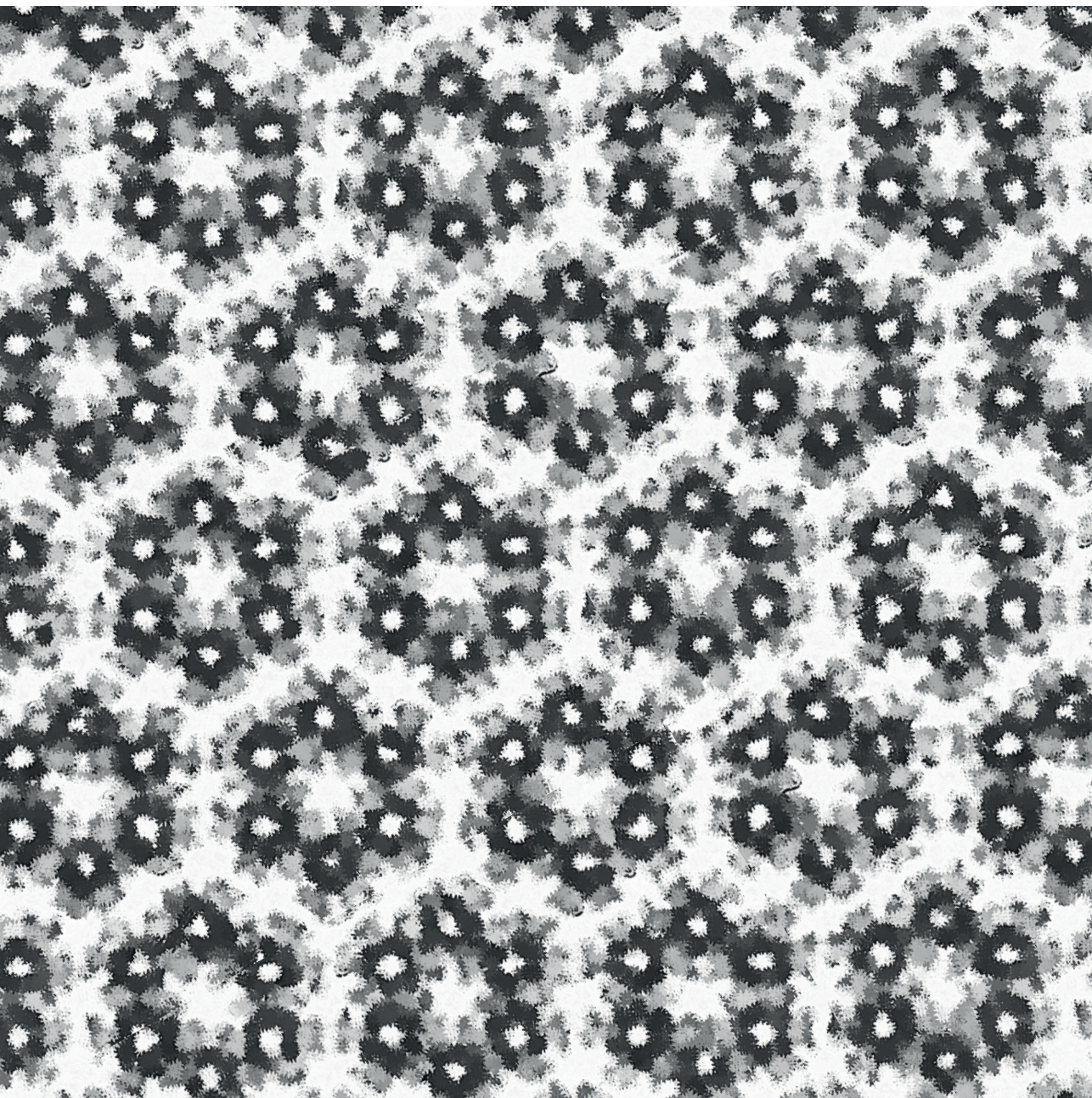
This time-course related ambiguity also affects both structural and functional studies of the chemosensory arrays by cryo-ET. The cell lysis treatment, which was intended to facilitate the higher-resolution imaging by flattening the cells, resulted in a high degree of heterogeneity among specimens that were frozen and imaged at a random point during lysis of the cells (**Chapter 3 & 4**). Although most of the receptor arrays in *V. cholerae* were found completely disordered, there were indeed rare cases in which the hexagonal packing order was retained in lysed *V. cholerae* cells. One could easily suspect that the lattice order was preserved because this cell was frozen the moment it was lysed so there was not enough time for the baseplate to disassociate. Alternatively, it could also be the case that the array patch retaining order upon lysis happens to have a high CheA occupancy so that the baseplate structure is more resilient to the lysis process and may hold up to the structural integrity particularly well. Due to the lack of time-course information, we could not depict how the chemosensory array structure changes during the cell lysis process and characterize it in greater detail to see how resilient the different baseplate structures may be. Compared to a gradual event such as lysis, the switching between different signaling states of the chemosensory complexes within the arrays is thought to be inherently dynamic on a much faster time scale. As a result, such functional and conformational dynamics cannot simply be captured by freezing at different time points before and after exposing chemosensory arrays to the target compounds (57). Instead, mutations of either the receptor or the kinase are required to strongly bias the signaling states of the complexes (**Chapter 5**). Only combined with extensive biochemistry characterization of the kinase activity of such mutants, structural information derived from cryo-ET data can be conclusive for illustrating the conformational dynamics related to the signaling process.

With its unparalleled advantages for visualizing arrays *in situ*, cryo-ET will certainly remain the best tool to explore the structural diversity of chemosensory arrays (**Chapter 2**). As insights into this diversity accumulate, interest will increase for understanding the physiological relevance of different types of chemosensory arrays. Cryo-ET will continue to be an essential tool to carry out the most direct and conclusive assessment

on whether any type of chemosensory array is assembled at a given culturing condition, as well as in any chemotaxis protein mutant strain. Moreover, observing the appearance and the occurrence of the arrays can help to reveal the strategies bacteria have evolved for dealing with complex environmental inputs. Cryo-ET may also assist in understanding the possible benefits of the crosstalk among different arrays or the necessity of segregation among different chemosensory pathways. For bacteria, both phenomena are essential for maintaining an efficient and accurate perception of the immediate chemical environment and thus is essential for their survival. In the case of *V. cholerae*, the chemosensory system is capable of converting signal inputs from 32 different 40H chemoreceptors into the net flux of phosphor-CheY to bias its swimming direction (278). Still, much is yet to be learned about how this sophisticated sensory system sorts and simplifies information.

Although it is developing faster than ever, cryo-ET has not yet advanced to a point where we can unambiguously determine individual chemotaxis protein structure directly in the native cellular context. To interpret the structural description of the arrays made by cryo-ET, we often require other lines of evidence and analysis derived from other characterization methods. Given that cryo-ET is very costly, time consuming, and not readily accessible outside highly specialized labs, the samples need to first be finely engineered or characterized through molecular biology and biochemistry studies. In addition, computational methods such as proteomics analysis on chemoreceptors and other chemotaxis proteins can shed insights into what the composition of the arrays might be. Moreover, compared to any other method, genomics-based bioinformatics analysis can most efficiently compare various chemosensory systems on a broad spectrum and make a commonly applicable prediction of the functional specificities of chemosensory arrays. Lastly, genetics analysis has contributed greatly to predicting the functionality of chemotaxis proteins and how they might selectively interact with chemoreceptors. In combination with genetics analysis, cryo-ET will remain as an essential tool to solve the open questions in understanding bacterial chemotaxis.

nederlandse Samenvatting



Alle vormen van leven zoeken altijd naar de beste omgevingsomstandigheden. De beweeglijke bacteriën zijn in staat om de chemische stoffen in hun directe omgeving te detecteren en hun beweging daarop aan te passen. Dit gedrag, dat chemotaxis genoemd wordt, wordt in gang gezet door één bijzondere macromoleculaire structuur: de chemosensorische arrays. Dit proefschrift brengt meerdere studies bijeen waarin ik gebruik heb gemaakt van cryo-elektronentomografie (cryo-ET) om een meer inzicht te krijgen in twee vragen: A) hoe zien bacteriële chemosensorische arrays eruit, en B) hoe werken signaaltransductie en kinasecontrole in de chemosensorische arrays op moleculair niveau.

Hoofdstuk 1 bevat een korte samenvatting van de geschiedenis van hoe bacteriële chemotaxis in de vorige eeuw werd ontdekt, en hoe de chemotaxis array-structuur in *Escherichia coli* (*E. coli*) werd ontdekt door gebruik te maken van cryo-ET. **Hoofdstuk 2** biedt een diepgaande beschouwing van de basis van chemotaxis-gedrag, het chemotaxis-signaleringspad, de chemotaxis-proteïnen, en de manier waarop ze in chemotaxische arrays zijn gerangschikt. Substantiële aandacht wordt besteed aan het feit dat chemosensorische arrays een ingenieuze structuur vormen die zeer conservatieve structuurkenmerken vertonen, maar tegelijkertijd een grote tolerantie voor compositionele diversiteit. Het meest opmerkelijk daarbij is wel dat de chemoreceptor arrays die tot dusver geobserveerd zijn, zelfs op een verre evolutionaire afstand, hexagonaal gestructureerde trimeren-van-dimeren met een constante roosterafstand zijn. Desalniettemin bestaat er een grote variëteit in chemosensorische arrays in termen van de exacte proteïnecompositie en stoichiometrie, de moleculaire architectuur in de grondplaat (waarde receptoren de kinase-CheA en de koppelproteïnen verbinden), de cellulaire localisatie, en de fysiologische relevantie. Belangrijker nog, zo wordt in deze bespreking naar voren gebracht, is dat er zo weinig bekend is over zulke gediversifieerde systemen buiten het modelorganisme *E. coli*, dat slechts één gesimplificeerd chemotaxis-pad heeft. Ondanks de overvloed aan informatie waar we tegenwoordig over beschikken, blijven er nog diverse vragen te beantwoorden met betrekking tot de structuur en functie van chemosensorische arrays.

Om inzicht te krijgen in de architectuur van chemosensorische arrays in verschillende bacteriën wordt in **Hoofdstuk 3** een studie beschreven naar de compositionele variabiliteit van chemosensorische arrays in *Vibrio cholerae* (*V. cholerae*). Arrays in *V. cholerae* hebben de mogelijkheid om hun chemoreceptorische compositie aan te passen om zo meer verschillende doelen te kunnen waarnemen. De chemotaxis-proteïnen in de grondplaat vertonen een hoge graad van compositionele variabiliteit, hetgeen potentieel de incorporatie van nieuwe receptoren in de reeds bestaande chemosensorische array faciliteert. Deze hoge variabiliteit van chemosensorische arrays wordt voorgesteld voor bacteriën met een groter repertoire aan chemoreceptoren,

meer extensieve hulp-chemotaxis-proteïnen, en diverse (signalerings) paden. Deze attributen wijken op kenmerkende wijze af van het chemotaxisparadigma in de studies over *E. coli*.

Behalve naar de compositionele variabiliteit, die is uitgewerkt in **Hoofdstuk 3**, heb ik ook onderzoek gedaan naar de moleculaire architectuur van de chemosensorische array grondplaat in *V. cholerae*, beschreven in **Hoofdstuk 4**. De hexagonale structuur van de receptor trimeren-van-dimeren blijft intact bij verschillende soorten, zoals eerder vastgesteld, maar de moleculaire compositie en architecturale schikking van chemotaxis-proteïne in de grondplaat wordt nu ook soort-specifiek besproken. In *V. cholerae* laat de histidine CheA een gelijkmatige verdeling over de grondplaat zien, maar zonder een bepaalde volgorde. Bij een dergelijke kinase-distributie zou je verwachten dat deze de rigiditeit van de arrays vermindert en een meer dynamische variabiliteit van chemoreceptoren en grondplaatcomponenten faciliteert. Het roept ook intrigerende vragen op over hoe een goede functionaliteit van arrays en een hoge mate van samenwerking bereikt kan worden als veel van de receptor trimeren-van-dimeren-eenheden niet in direct contact zijn met de kinase.

In **Hoofdstuk 5** wordt een studie gepresenteerd die is uitgevoerd met het modelorganisme *E. coli*. Ik heb hiervoor onderzoek gedaan naar het moleculaire mechanisme van chemotaxis binnen chemosensorische signaalkerneenheden, de minimale structurele en functionele herhalingen van de arrays. Met behulp van zorgvuldig ontwerp en engineering werden gemodificeerde signaalkerneenheden gemanipuleerd naar ofwel een kinase-ON- of een kinase-OFF-signalerings-eindstaat. De conformatiedynamiek van de serie-chemoreceptoren zou gevisualiseerd kunnen worden en inzicht geven in hoe chemoreceptoren kinasecontrole bereiken. Door de compactheid van de structuur te veranderen op het niveau van de trimeren-van-dimeren, kunnen overeenkomstige conformationele veranderingen worden waargenomen. Dit resultaat is in overeenstemming met klassieke theorieën die zijn voorgesteld om het signaleringsmechanisme in chemoreceptoren te beschrijven. Voorts suggereren de resultaten waarom de trimeren-van-dimeren-schikking van de receptoren noodzakelijk zou kunnen zijn om zijn taak te kunnen uitvoeren in de chemosensorische arrays.

De bovengenoemde hoofdstukken zijn samengesteld met een focus op het wetenschappelijke onderwerp van dit proefschrift: de structurele en functionele studies naar chemosensorische arrays. In **Hoofdstuk 6** verschuift de focus naar de primaire wetenschappelijke techniek die bij al deze studies gebruikt is: cryo-ET. Dit is momenteel de enige methode waarmee hoge-resolutie structurele studies gedaan kunnen worden naar chemotaxis-arrays in een bijna-natuurlijke staat. Dit hoofdstuk

biedt een overzicht van hoe cryo-ET kan worden gebruikt om chemosensorische arrays *in situ* te visualiseren door gebruik te maken van transmissie-elektronenmicroscopie in cryogene omstandigheden. In dit hoofdstuk is een korte introductie van cryo-ET opgenomen, evenals een stap-voor-stap-beschrijving van het standaard werkproces met daarbij inbegrepen de cryo-specimen-preparatie; 2D tilt-seriebeeldvorming en 3D tomografische datareconstructie.

De voornaamste bevindingen in dit proefschrift en de implicaties ervan in een bredere context worden besproken in elk hoofdstuk. In **Hoofdstuk 7** wordt de cryo-elektronentomografie-techniek besproken, speciaal toegepast op de onderzoeken in dit proefschrift. Met name komen aan bod de specifieke beperkingen die deze techniek heeft als deze wordt toegepast bij studies van bacteriële chemosensorische arrays. En ook wordt uiteengezet hoe verbeteringen van deze techniek kunnen bijdragen aan een nog beter begrip van bacteriële chemotaxis.

References

1. Berg HC (1975) Chemotaxis in bacteria. *Annu Rev Biophys Bioeng* 4(00):119-136.
2. Adler J (1966) Chemotaxis in bacteria. *Science* 153(3737):708-716.
3. Adler J (1966) Effect of amino acids and oxygen on chemotaxis in *Escherichia coli*. *J Bacteriol* 92(1):121-129.
4. Adler J (1966) Chemotaxis in Bacteria. *Science* 153(3737):708-716.
5. Berg HC , Brown DA (1972) Chemotaxis in *Escherichia Coli* Analyzed by 3-Dimensional Tracking. *Nature* 239(5374):500-504.
6. Adler J (1969) Chemoreceptors in bacteria. *Science* 166(3913):1588-1597.
7. Adler J, Templeton B (1967) The effect of environmental conditions on the motility of *Escherichia coli*. *Microbiology* 46(2):175-184.
8. DePamphilis ML , Adler J (1971) Purification of intact flagella from *Escherichia coli* and *Bacillus subtilis*. *J Bacteriol* 105(1):376-383.
9. DePamphilis ML , Adler J (1971) Fine structure and isolation of the hook-basal body complex of flagella from *Escherichia coli* and *Bacillus subtilis*. *J Bacteriol* 105(1):384-395.
10. Thomas DR, Francis NR, Xu C, DeRosier DJ (2006) The three-dimensional structure of the flagellar rotor from a clockwise-locked mutant of *Salmonella enterica* serovar typhimurium. *J Bacteriol* 188(20):7039-7048.
11. Berg HC, Anderson RA (1973) Bacteria swim by rotating their flagellar filaments. *Nature* 245:380-382.
12. Abram D, Mitchen JR, Koffler H, Vatter AE (1970) Differentiation within bacterial flagellum and isolation of proximal hook. *J Bacteriol* 101(1):250-261.
13. Larsen SH, Reader RW, Kort EN, Tso W-W, Adler J (1974) Change in direction of flagellar rotation is the basis of the chemotactic response in *Escherichia coli*. *Nature* 249(5452):74-77.
14. Silverman M, Simon M (1974) Flagellar rotation and the mechanism of bacterial motility. *Nature* 249(452):73-74.
15. Berg HC (1974) Dynamic properties of bacterial flagellar motors. *Nature* 249(452):77-79.
16. Aizawa SI, Dean GE, Jones CJ, Macnab RM, Yamaguchi S (1985) Purification and characterization of the flagellar hook-basal body complex of *Salmonella typhimurium*. *J Bacteriol* 161(3):836-849.
17. Thomas D, Morgan DG, DeRosier DJ (2001) Structures of bacterial flagellar motors from two FlIF-FlIG gene fusion mutants. *J Bacteriol* 183(21):6404-6412.
18. Chen S, Beeby M, Murphy GE, Leadbetter JR, Hendrixson DR, Briegel A, Li Z, Shi J, Tocheva EI, Muller A, Dobro MJ, Jensen GJ (2011) Structural diversity of bacterial flagellar motors. *EMBO J* 30(14):2972-2981.
19. Kaplan M, Ghosal D, Subramanian P, Oikonomou CM, Kjaer A, Pirbadian S,

REFERENCES

- Ortega DR, Briegel A, El-Naggar MY, Jensen GJ (2019) The presence an absence of periplasmic rings in bacterial flagellar motors correlates with stator type. *Elife* 8:e43487.
20. Ferreira JL, Gao FZ, Rossmann FM, Nans A, Brenzinger S, Hosseini R, Wilson A, Briegel A, Thormann KM, Rosenthal PB, Beeby M (2019) γ -proteobacteria eject their polar flagella under nutrient depletion, retaining flagellar motor relic structures. *Plos Biology* 17(3):e3000165.
21. Sowa Y , Berry RM (2008) Bacterial flagellar motor. *Q Rev Biophys* 41(2):103-132.
22. Parkinson JS, Blair DF (1993) Does *E. coli* have a nose? *Science* 259(5102):1701-1702.
23. Maddock JR, Shapiro L (1993) Polar location of the chemoreceptor complex in the *Escherichia coli* cell. *Science* 259(5102):1717-1723.
24. Mesibov R, Adler J (1972) Chemotaxis toward amino-acids in *Escherichia Coli*. *J Bacteriol* 112(1):315-326.
25. Adler J, Hazelbauer GL, Dahl MM (1973) Chemotaxis toward Sugars in *Escherichia Coli*. *J Bacteriol* 115(3):824-847.
26. Tso WW, Adler J (1974) Negative chemotaxis in *Escherichia coli*. *J Bacteriol* 118(2):560-576.
27. Parkinson JS (1975) Genetics of chemotactic behavior in bacteria. *Cell* 4(3):183-188.
28. Parkinson JS (1976) cheA, cheB, and cheC genes of *Escherichia coli* and their role in chemotaxis. *J Bacteriol* 126(2):758-770.
29. Parkinson JS (1978) Complementation analysis and deletion mapping of *Escherichia coli* mutants defective in chemotaxis. *J Bacteriol* 135(1):45-53.
30. Silverman M, Simon M (1977) Chemotaxis in *Escherichia coli* : Methylation of che gene products. *Proc Natl Acad Sci USA* 74(8):3317-3321.
31. Springer MS, Goy MF, Adler J (1977) Sensory transduction in *Escherichia Coli* : 2 complementary pathways of information-processing that involve methylated proteins. *Proc Natl Acad Sci USA* 74(8):3312-3316.
32. Kort EN, Goy MF, Larsen SH, Adler J (1975) Methylation of a membrane protein involved in bacterial chemotaxis. *Proc Natl Acad Sci USA* 72(10):3939-3943.
33. Goy MF, Springer MS, Adler J (1977) Sensory transduction in *Escherichia coli*: role of a protein methylation reaction in sensory adaptation. *Proc Natl Acad Sci USA* 74(11):4964-4968.
34. Springer MS, Goy MF, Adler J (1977) Sensory transduction in *Escherichia Coli* : requirement for methionine in sensory adaptation. *Proc Natl Acad Sci USA* 74(1):183-187.
35. Hess JF, Oosawa K, Matsumura P, Simon MI (1987) Protein-phosphorylation Is involved in bacterial chemotaxis. *Proc Natl Acad Sci USA* 84(21):7609-7613.

36. Hess JF, Bourret RB, Simon MI (1988) Histidine phosphorylation and phosphoryl group transfer in bacterial chemotaxis. *Nature* 336(6195):139-143.
37. Borkovich KA, Kaplan N, Hess JF, Simon MI (1989) Transmembrane signal transduction in bacterial chemotaxis involves ligand-dependent activation of phosphate group transfer. *Proc Natl Acad Sci USA* 86(4):1208-1212.
38. Borkovich KA, Simon MI (1990) The dynamics of protein phosphorylation in bacterial chemotaxis. *Cell* 63(6):1339-1348.
39. Gegner JA, Graham DR, Roth AF, Dahlquist FW (1992) Assembly of an MCP receptor, CheW, and kinase CheA complex in the bacterial chemotaxis signal transduction pathway. *Cell* 70(6):975-982.
40. Liu Y, Levit M, Lurz R, Surette MG, Stock JB (1997) Receptor-mediated protein kinase activation and the mechanism of transmembrane signaling in bacterial chemotaxis. *EMBO J* 16(24):7231-7240.
41. Francis NR, Levit MN, Shaikh TR, Melanson LA, Stock JB, DeRosier DJ (2002) Subunit organization in a soluble complex of tar, CheW, and CheA by electron microscopy. *J Biol Chem* 277(39):36755-36759.
42. Zhang P, Khursigara CM, Hartnell LM, Subramaniam S (2007) Direct visualization of *Escherichia coli* chemotaxis receptor arrays using cryo-electron microscopy. *Proc Natl Acad Sci USA* 104(10):3777-3781.
43. Briegel A, Li X, Bilwes AM, Hughes KT, Jensen GJ, Crane BR (2012) Bacterial chemoreceptor arrays are hexagonally packed trimers of receptor dimers networked by rings of kinase and coupling proteins. *Proc Natl Acad Sci USA* 109(10):3766-3771.
44. Liu J, Hu B, Morado DR, Jani S, Manson MD, Margolin W (2012) Molecular architecture of chemoreceptor arrays revealed by cryoelectron tomography of *Escherichia coli* minicells. *Proc Natl Acad Sci USA* 109(23):E1481-1488.
45. Cassidy CK, Himes BA, Alvarez FJ, Ma J, Zhao G, Perilla JR, Schulten K, Zhang P (2015) CryoEM and computer simulations reveal a novel kinase conformational switch in bacterial chemotaxis signaling. *Elife* 4:e08419.
46. Kim KK, Yokota H, Kim SH (1999) Four-helical-bundle structure of the cytoplasmic domain of a serine chemotaxis receptor. *Nature* 400(6746):787-792.
47. Bilwes AM, Alex LA, Crane BR, Simon MI (1999) Structure of CheA, a signal-transducing histidine kinase. *Cell* 96(1):131-141.
48. Park S-Y, Borbat PP, Gonzalez-Bonet G, Bhatnagar J, Pollard AM, Freed JH, Bilwes AM, Crane BR (2006) Reconstruction of the chemotaxis receptor-kinase assembly. *Nat Struct Mol Biol* 13(5):400-407.
49. Francis NR, Wolanin PM, Stock JB, Derosier DJ, Thomas DR (2004) Three-dimensional structure and organization of a receptor/signaling complex. *Proc Natl Acad Sci USA* 101(50):17480-17485.
50. Briegel A (2005) Strukturuntersuchungen an Prokaryonten mit Kryo-

REFERENCES

- Elektronentomographie.
51. Briegel A, Ortega DR, Tocheva EI, Wuichet K, Li Z, Chen S, Muller A, Iancu CV, Murphy GE, Dobro MJ, Zhulin IB, Jensen GJ (2009) Universal architecture of bacterial chemoreceptor arrays. *Proc Natl Acad Sci USA* 106(40):17181-17186.
 52. Briegel A, Chen S, Koster AJ, Plitzko JM, Schwartz CL, Jensen GJ (2010) Correlated light and electron cryo-microscopy. *Method Enzymol* 481:317-341.
 53. Li M, Hazelbauer GL (2011) Core unit of chemotaxis signaling complexes. *Proc Natl Acad Sci USA* 108(23):9390-9395.
 54. Briegel A, Ames P, Gumbart JC, Oikonomou CM, Parkinson JS, Jensen GJ (2013) The mobility of two kinase domains in the *Escherichia coli* chemoreceptor array varies with signalling state. *Mol Microbiol* 89(5):831-841.
 55. Briegel A, Ortega DR, Huang AN, Oikonomou CM, Gunsalus RP, Jensen GJ (2015) Structural conservation of chemotaxis machinery across Archaea and Bacteria. *Environ Microbiol Rep* 7(3):414-419.
 56. Khursigara CM, Wu X, Zhang P, Lefman J, Subramaniam S (2008) Role of HAMP domains in chemotaxis signaling by bacterial chemoreceptors. *Proc Natl Acad Sci USA* 105(43):16555-16560.
 57. Briegel A, Beeby M, Thanbichler M, Jensen GJ (2011) Activated chemoreceptor arrays remain intact and hexagonally packed. *Mol Microbiol* 82(3):748-757.
 58. Briegel A, Wong ML, Hodges HL, Oikonomou CM, Piasta KN, Harris MJ, Fowler DJ, Thompson LK, Falke JJ, Kiessling LL, Jensen GJ (2014) New insights into bacterial chemoreceptor array structure and assembly from electron cryotomography. *Biochemistry* 53(10):1575-1585.
 59. Yang W, Cassidy CK, Ames P, Diebold CA, Schulten K, Luthey-Schulten Z, Parkinson JS, Briegel A (2019) *In situ* conformational changes of the *Escherichia coli* serine chemoreceptor in different signaling states. *mBio* 10(4):e00973-19.
 60. Briegel A, Jensen G (2017) Progress and potential of electron cryotomography as illustrated by its application to bacterial chemoreceptor arrays. *Annu Rev Biophys* 46:1-21.
 61. Wadhams GH, Armitage JP (2004) Making sense of it all: bacterial chemotaxis. *Nat Rev Mol Cell Biol* 5(12):1024-1037.
 62. Adler J (1965) Chemotaxis in *Escherichia coli*. *Cold Spring Harb Symp Quant Biol* 30:289-292.
 63. Hazelbauer GL, Falke JJ, Parkinson JS (2008) Bacterial chemoreceptors: high-performance signaling in networked arrays. *Trends Biochem Sci* 33(1):9-19.
 64. Parkinson JS, Hazelbauer GL, Falke JJ (2015) Signaling and sensory adaptation in *Escherichia coli* chemoreceptors: 2015 update. *Trends Microbiol* 23(5):257-266.
 65. Turner L, Ryu WS, Berg HC (2000) Real-time imaging of fluorescent flagellar filaments. *J Bacteriol* 182(10):2793-2801.

66. Berg HC (2003) The rotary motor of bacterial flagella. *Annu Rev Biochem* 72:19-54.
67. Milburn MV, Prive GG, Milligan DL, Scott WG, Yeh J, Jancarik J, Koshland DE, Kim SH (1991) 3-dimensional structures of the ligand-binding domain of the bacterial aspartate receptor with and without a ligand. *Science* 254(5036):1342-1347.
68. Tam R, Saier MH, Jr. (1993) Structural, functional, and evolutionary relationships among extracellular solute-binding receptors of bacteria. *Microbiol Rev* 57(2):320-346.
69. Berg HC, Tedesco PM (1975) Transient response to chemotactic stimuli in *Escherichia coli*. *Proc Natl Acad Sci USA* 72:3235-3239.
70. Wuichet K, Zhulin IB (2010) Origins and diversification of a complex signal transduction system in prokaryotes. *Sci Signal* 3(128):ra50.
71. He K, Bauer CE (2014) Chemosensory signaling systems that control bacterial survival. *Trends Microbiol* 22(7):389-398.
72. Xu H, Sultan S, Yerge A, Moon KH, Wooten RM, Motaleb MA (2017) *Borrelia burgdorferi* CheY2 is dispensable for chemotaxis or motility but crucial for the infectious life cycle of the spirochete. *Infect Immun* 85(1):e00264-00216.
73. Novak EA, Sekar P, Xu H, Moon KH, Manne A, Wooten RM, Motaleb MA (2016) The *Borrelia burgdorferi* CheY3 response regulator is essential for chemotaxis and completion of its natural infection cycle. *Cell Microbiol* 18(12):1782-1799.
74. Huang JY, Sweeney EG, Sigal M, Zhang HC, Remington SJ, Cantrell MA, Kuo CJ, Guillemin K, Amieva MR (2015) Chemodetection and destruction of host urea allows *Helicobacter pylori* to locate the epithelium. *Cell Host Microbe* 18(2):147-156.
75. Li Z, Lou H, Ojcius DM, Sun A, Sun D, Zhao J, Lin X, Yan J (2014) Methyl-accepting chemotaxis proteins 3 and 4 are responsible for *Campylobacter jejuni* chemotaxis and jejuna colonization in mice in response to sodium deoxycholate. *J Med Microbiol* 63(Pt 3):343-354.
76. Millet YA, Alvarez D, Ringgaard S, von Andrian UH, Davis BM, Waldor MK (2014) Insights into *Vibrio cholerae* intestinal colonization from monitoring fluorescently labeled bacteria. *PLoS pathogens* 10(10):e1004405.
77. Francis VI, Stevenson EC, Porter SL (2017) Two-component systems required for virulence in *Pseudomonas aeruginosa*. *FEMS Microbiol Lett* 364(11).
78. Johnson KS, Ottemann KM (2018) Colonization, localization, and inflammation: the roles of *H. pylori* chemotaxis *in vivo*. *Curr Opin Microbiol* 41:51-57.
79. Heering J, Ringgaard S (2016) Differential localization of chemotactic signaling arrays during the lifecycle of *Vibrio parahaemolyticus*. *Front Microbiol* 7:1767.
80. Ringgaard S, Hubbard T, Mandlik A, Davis BM, Waldor MK (2015) RpoS and quorum sensing control expression and polar localization of *Vibrio cholerae* chemotaxis cluster III proteins *in vitro* and *in vivo*. *Mol Microbiol* 97(4):660-675.

REFERENCES

81. Guvener ZT, Tifrea DF, Harwood CS (2006) Two different *Pseudomonas aeruginosa* chemosensory signal transduction complexes localize to cell poles and form and remould in stationary phase. *Mol Microbiol* 61(1):106-118.
82. Gosink KK, Kobayashi R, Kawagishi I, Hase CC (2002) Analyses of the roles of the three cheA homologs in chemotaxis of *Vibrio cholerae*. *J Bacteriol* 184(6):1767-1771.
83. Brenzinger S, van der Aart LT, van Wezel GP, Lacroix J-M, Glatter T, Briegel A (2019) Structural and proteomic changes in viable but non-culturable *Vibrio cholerae*. *Front Microbiol* 10:793.
84. Colin R, Sourjik V (2017) Emergent properties of bacterial chemotaxis pathway. *Curr Opin Microbiol* 39:24-33.
85. Bardy SL, Briegel A, Rainville S, Krell T (2017) Recent advances and future prospects in bacterial and archaeal locomotion and signal transduction. *J Bacteriol* 199(18):e00203-00217.
86. Lacal J, Garcia-Fontana C, Munoz-Martinez F, Ramos JL, Krell T (2010) Sensing of environmental signals: classification of chemoreceptors according to the size of their ligand binding regions. *Environ Microbiol* 12(11):2873-2884.
87. Ulrich LE, Zhulin IB (2010) The MiST2 database: a comprehensive genomics resource on microbial signal transduction. *Nucleic Acids Res* 38(Database issue):D401-407.
88. Philippe N, Wu LF (2010) An MCP-like protein interacts with the MamK cytoskeleton and is involved in magnetotaxis in *Magnetospirillum magneticum* AMB-1. *J Mol Biol* 400(3):309-322.
89. Ortega Á, Zhulin IB, Krell T (2017) Sensory repertoire of bacterial chemoreceptors. *Microbiol Mol Biol Rev* 81(4):e00033-00017.
90. Matilla MA, Krell T (2017) Chemoreceptor-based signal sensing. *Curr Opin Biotechnol* 45:8-14.
91. Alexander RP, Zhulin IB (2007) Evolutionary genomics reveals conserved structural determinants of signaling and adaptation in microbial chemoreceptors. *Proc Natl Acad Sci USA* 104(8):2885-2890.
92. Pinas GE, Frank V, Vaknin A, Parkinson JS (2016) The source of high signal cooperativity in bacterial chemosensory arrays. *Proc Natl Acad Sci USA* 113(12):3335-3340.
93. Li M, Hazelbauer GL (2014) Selective allosteric coupling in core chemotaxis signaling complexes. *Proc Natl Acad Sci USA* 111(45):15940-15945.
94. Li M, Hazelbauer GL (2004) Cellular stoichiometry of the components of the chemotaxis signaling complex. *J Bacteriol* 186(12):3687-3694.
95. Erbse AH, Falke JJ (2009) The core signaling proteins of bacterial chemotaxis assemble to form an ultrastable complex. *Biochemistry* 48(29):6975-6987.
96. Studdert CA, Parkinson JS (2004) Crosslinking snapshots of bacterial

- chemoreceptor squads. *Proc Natl Acad Sci USA* 101(7):2117-2122.
97. Wang X, Vu A, Lee K, Dahlquist FW (2012) CheA-receptor interaction sites in bacterial chemotaxis. *J Mol Biol* 422(2):282-290.
 98. Bass RB, Falke JJ (1998) Detection of a conserved alpha-helix in the kinase-docking region of the aspartate receptor by cysteine and disulfide scanning. *J Biol Chem* 273(39):25006-25014.
 99. Piasta KN, Ulliman CJ, Slivka PF, Crane BR, Falke JJ (2013) Defining a key receptor-CheA kinase contact and elucidating its function in the membrane-bound bacterial chemosensory array: a disulfide mapping and TAM-IDS Study. *Biochemistry* 52(22):3866-3880.
 100. Li X, Fleetwood AD, Bayas C, Bilwes AM, Ortega DR, Falke JJ, Zhulin IB, Crane BR (2013) The 3.2 Å resolution structure of a receptor: CheA:CheW signaling complex defines overlapping binding sites and key residue interactions within bacterial chemosensory arrays. *Biochemistry* 52(22):3852-3865.
 101. Natale AM, Duplantis JL, Piasta KN, Falke JJ (2013) Structure, function, and on-off switching of a core unit contact between CheA kinase and CheW adaptor protein in the bacterial chemosensory array: A disulfide mapping and mutagenesis study. *Biochemistry* 52(44):7753-7765.
 102. Yang W, Alvarado A, Glatter T, Ringgaard S, Briegel A (2018) Baseplate variability of *Vibrio cholerae* chemoreceptor arrays. *Proc Natl Acad Sci USA* 115(52):13365-13370.
 103. Haglin ER, Yang W, Briegel A, Thompson LK (2017) His-tag-mediated dimerization of chemoreceptors leads to assembly of functional nanoarrays. *Biochemistry* 56(44):5874-5885.
 104. Briegel A, Ortega DR, Mann P, Kjaer A, Ringgaard S, Jensen GJ (2016) Chemotaxis cluster 1 proteins form cytoplasmic arrays in *Vibrio cholerae* and are stabilized by a double signaling domain receptor DosM. *Proc Natl Acad Sci USA* 113(37):10412-10417.
 105. Briegel A, Ladinsky MS, Oikonomou C, Jones CW, Harris MJ, Fowler DJ, Chang YW, Thompson LK, Armitage JP, Jensen GJ (2014) Structure of bacterial cytoplasmic chemoreceptor arrays and implications for chemotactic signaling. *Elife* 3:e02151.
 106. Collins KD, Lacal J, Ottemann KM (2014) Internal sense of direction: sensing and signaling from cytoplasmic chemoreceptors. *Microbiol Mol Biol R* 78(4):672-684.
 107. Huang Z, Pan X, Xu N, Guo M (2019) Bacterial chemotaxis coupling protein: Structure, function and diversity. *Microbiol Res* 219:40-48.
 108. Alexander RP, Lowenthal AC, Harshey RM, Ottemann KM (2010) CheV: CheW-like coupling proteins at the core of the chemotaxis signaling network. *Trends Microbiol* 18(11):494-503.
 109. Karatan E, Saulmon MM, Bunn MW, Ordal GW (2001) Phosphorylation of the

REFERENCES

- response regulator CheV is required for adaptation to attractants during *Bacillus subtilis* chemotaxis. *J Biol Chem* 276(47):43618-43626.
110. Ortega DR, Zhulin IB (2016) Evolutionary genomics suggests that CheV is an additional adaptor for accommodating specific chemoreceptors within the chemotaxis signaling complex. *PLoS Comput Biol* 12(2):e1004723.
111. Hartley-Tassell LE, Shewell LK, Day CJ, Wilson JC, Sandhu R, Ketley JM, Korolik V (2010) Identification and characterization of the aspartate chemosensory receptor of *Campylobacter jejuni*. *Mol Microbiol* 75(3):710-730.
112. Alvarado A, Kjær A, Yang W, Mann P, Briegel A, Waldor MK, Ringgaard S (2017) Coupling chemosensory array formation and localization. *ELife* 6:e31058.
113. Yamaichi Y, Bruckner R, Ringgaard S, Möll A, Cameron DE, Briegel A, Jensen GJ, Davis BM, Waldor MK (2012) A multidomain hub anchors the chromosome segregation and chemotactic machinery to the bacterial pole. *Genes Dev* 26(20):2348-2360.
114. Jones CW, Armitage JP (2015) Positioning of bacterial chemoreceptors. *Trends Microbiol* 23(5):247-256.
115. Cannistraro VJ, Glekas GD, Rao CV, Ordal GW (2011) Cellular stoichiometry of the chemotaxis proteins in *Bacillus subtilis*. *J Bacteriol* 193(13):3220-3227.
116. Mauriello EMF, Jones C, Moine A, Armitage JP (2018) Cellular targeting and segregation of bacterial chemosensory systems. *FEMS Microbiol Rev* 42(4):462-476.
117. Kentner D, Sourjik V (2006) Spatial organization of the bacterial chemotaxis system. *Curr Opin Microbiol* 9(6):619-624.
118. Moglich A, Ayers RA, Moffat K (2009) Structure and signaling mechanism of Per-ARNT-Sim domains. *Structure* 17(10):1282-1294.
119. Parkinson JS (2010) Signaling mechanisms of HAMP domains in chemoreceptors and sensor kinases. *Annu Rev Microbiol* 64:101-122.
120. Airola MV, Huh D, Sukomon N, Widom J, Sircar R, Borbat PP, Freed JH, Watts KJ, Crane BR (2013) Architecture of the soluble receptor Aer2 indicates an in-line mechanism for PAS and HAMP domain signaling. *J Mol Biol* 425(5):886-901.
121. Herrera Seitz MK, Frank V, Massazza DA, Vaknin A, Studdert CA (2014) Bacterial chemoreceptors of different length classes signal independently. *Mol Microbiol* 93(4):814-822.
122. Ortega DR, Yang W, Subramanian P, Mann P, Kjær A, Chen S, Watts KJ, Pirbadian S, Collins DA, Kooger R, Kalyuzhnaya MG, Ringgaard S, Briegel A, Jensen GJ. (2020) Repurposing a chemosensory macromolecular machine. *Nat Commun* 11:2041
123. Huang Z, Wang Y-H, Zhu H-Z, Andrianova EP, Jiang CY, Li D, Ma L, Feng J, Liu ZP, Xiang H, Zhulin IB, Liu SJ (2019) Crosstalk between chemosensory pathways that modulate chemotaxis and biofilm formation. *mBio* 10(1):e02876-02818.

124. Guo ML, Huang ZW, Yang J (2017) Is there any crosstalk between the chemotaxis and virulence induction signaling in *Agrobacterium tumefaciens*? *Biotechnol Adv* 35(4):505-511.
125. Persat A, Inclan YF, Engel JN, Stone HA, Gitai Z (2015) Type IV pili mechanoechemically regulate virulence factors in *Pseudomonas aeruginosa*. *Proc Natl Acad Sci USA* 112(24):7563-7568.
126. Scott KA, Porter SL, Bagg EA, Hamer R, Hill JL, Wilkinson DA, Armitage JP (2010) Specificity of localization and phosphotransfer in the CheA proteins of *Rhodobacter sphaeroides*. *Mol Microbiol* 76(2):318-330.
127. Moine A, Agrebi R, Espinosa L, Kirby JR, Zusman DR, Mignot T, Mauriello EM (2014) Functional organization of a multimodular bacterial chemosensory apparatus. *PLoS Genet* 10(3):e1004164.
128. Martin-Mora D, Fernandez M, Velando F, Ortega A, Gavira JA, Matilla MA, Krell T (2018) Functional annotation of bacterial signal transduction systems: Progress and challenges. *Int J Mol Sci* 19(12):3755.
129. Ortega DR, Fleetwood AD, Krell T, Harwood CS, Jensen GJ, Zhulin IB (2017) Assigning chemoreceptors to chemosensory pathways in *Pseudomonas aeruginosa*. *Proc Natl Acad Sci USA* 114(48):12809-12814.
130. Sampedro I, Parales RE, Krell T, Hill JE (2015) *Pseudomonas* chemotaxis. *FEMS Microbiol Rev* 39(1):17-46.
131. Cassidy CK, Himes BA, Luthey-Schulten Z, Zhang P (2018) CryoEM-based hybrid modeling approaches for structure determination. *Curr Opin Microbiol* 43:14-23.
132. Briegel A, Jensen G (2017) Progress and potential of electron cryotomography as illustrated by its application to bacterial chemoreceptor Arrays. *Annu Rev Biophys* 46:1-21.
133. Greenfield D, McEvoy AL, Shroff H, Crooks GE, Wingreen NS, Betzig E, Liphardt J (2009) Self-organization of the *Escherichia coli* chemotaxis network imaged with super-resolution light microscopy. *PLoS Biol* 7(6):e1000137.
134. Wang L, Bateman B, Zanetti-Domingues LC, Moores AN, Astbury S, Spindloe C, Darrow MC, Romano M, Needham SR, Beis K, Rolfe DJ, Clarke DT, Martin-Fernandez ML (2019) Solid immersion microscopy images cells under cryogenic conditions with 12 nm resolution. *Commun Biol* 2(1):74.
135. Tuijtel MW, Koster AJ, Jakobs S, Faas FGA, Sharp TH (2019) Correlative cryo super-resolution light and electron microscopy on mammalian cells using fluorescent proteins. *Sci Rep* 9(1):1369.
136. Kaufmann R, Schellenberger P, Seiradake E, Dobbie IM, Jones EY, Davis I, Hagen C, Grunewald K (2014) Super-resolution microscopy using standard fluorescent proteins in intact cells under cryo-conditions. *Nano Lett* 14(7):4171-4175.
137. Chang YW, Chen S, Tocheva EI, Treuner-Lange A, Lobach S, Sogaard-Andersen L, Jensen GJ (2014) Correlated cryogenic photoactivated localization microscopy

REFERENCES

- and cryo-electron tomography. *Nat Methods* 11(7):737-739.
138. Milburn MV, Prive GG, Milligan DL, Scott WG, Yeh J, Jancarik J, Koshland DE, Jr., Kim SH (1991) Three-dimensional structures of the ligand-binding domain of the bacterial aspartate receptor with and without a ligand. *Science* 254(5036):1342-1347.
 139. Englert DL, Manson MD, Jayaraman A (2010) Investigation of bacterial chemotaxis in flow-based microfluidic devices. *Nat Protoc* 5(5):864-872.
 140. Stock J, Da Re S (2000) Signal transduction: response regulators on and off. *Curr Biol* 10(11):R420-424.
 141. Cassidy CK, Himes BA, Alvarez FJ, Ma J, Zhao G, Perilla JR, Schulten K, Zhang P (2015) CryoEM and computer simulations reveal a novel kinase conformational switch in bacterial chemotaxis signaling. *Elife* 4:e08419
 142. Fu X, Himes BA, Ke D, Rice WJ, Ning J, Zhang P (2014) Controlled bacterial lysis for electron tomography of native cell membranes. *Structure* 22(12):1875-1882.
 143. Kan B, Habibi H, Schmid M, Liang W, Wang R, Wang D, Jungblut PR (2004) Proteome comparison of *Vibrio cholerae* cultured in aerobic and anaerobic conditions. *Proteomics* 4(10):3061-3067.
 144. Hiremath G, Hyakutake A, Yamamoto K, Ebisawa T, Nakamura T, Nishiyama S, Homma M, Kawagishi I (2015) Hypoxia-induced localization of chemotaxis-related signaling proteins in *Vibrio cholerae*. *Mol Microbiol* 95(5):780-790.
 145. Ringgaard S, Yang W, Alvarado A, Schirner K, Briegel A (2018) Chemotaxis arrays in *Vibrio* species and their intracellular positioning by the ParC/ParP system. *J Bacteriol.* 200(15):e00793-17.
 146. Ringgaard S, Zepeda-Rivera M, Wu X, Schirner K, Davis BM, Waldor MK (2014) ParP prevents dissociation of CheA from chemotactic signaling arrays and tethers them to a polar anchor. *Proc Natl Acad Sci USA* 111(2):e255-264.
 147. Kentner D, Thiem S, Hildenbeutel M, Sourjik V (2006) Determinants of chemoreceptor cluster formation in *Escherichia coli*. *Mol Microbiol* 61(2):407-417.
 148. Ringgaard S, Schirner K, Davis BM, Waldor MK (2011) A family of ParA-like ATPases promotes cell pole maturation by facilitating polar localization of chemotaxis proteins. *Genes Dev* 25(14):1544-1555.
 149. Wiseman HM, Milburn GJ (1991) Noise reduction in a laser by nonlinear damping. *Phys Rev A* 44(11):7815-7819.
 150. Weis RM, Hirai T, Chalah A, Kessel M, Peters PJ, Subramaniam S (2003) Electron microscopic analysis of membrane assemblies formed by the bacterial chemotaxis receptor Tsr. *J Bacteriol* 185(12):3636-3643.
 151. Szurmant H, Ordal GW (2004) Diversity in chemotaxis mechanisms among the bacteria and archaea. *Microbiol Mol Biol Rev* 68(2):301-319.

152. Levit MN, Grebe TW, Stock JB (2002) Organization of the receptor-kinase signaling array that regulates *Escherichia coli* chemotaxis. *J Biol Chem* 277(39):36748-36754.
153. Yuan J, Jin F, Glatter T, Sourjik V (2017) Osmosensing by the bacterial PhoQ/PhoP two-component system. *Proc Natl Acad Sci USA* 114(50):e10792-10798.
154. Glatter T, Ahrne E, Schmidt A (2015) Comparison of different sample preparation protocols reveals lysis buffer-specific extraction biases in gram-negative bacteria and human cells. *J Proteome Res* 14(11):4472-4485.
155. MacLean B, Tomazela DM, Shulman N, Chambers M, Finney GL, Frewen B, Kern R, Tabb DL, Liebler DC, MacCoss MJ (2010) Skyline: an open source document editor for creating and analyzing targeted proteomics experiments. *Bioinformatics* 26(7):966-968.
156. Mastronarde DN (1997) Dual-axis tomography: an approach with alignment methods that preserve resolution. *J Struct Biol* 120(3):343-352.
157. Xiong Q, Morpew MK, Schwartz CL, Hoenger AH, Mastronarde DN (2009) CTF determination and correction for low dose tomographic tilt series. *J Struct Biol* 168(3):378-387.
158. Castano-Diez D, Kudryashev M, Arheit M, Stahlberg H (2012) Dynamo: a flexible, user-friendly development tool for subtomogram averaging of cryo-EM data in high-performance computing environments. *J Struct Biol* 178(2):139-151.
159. Castano-Diez D, Kudryashev M, Stahlberg H (2017) Dynamo Catalogue: Geometrical tools and data management for particle picking in subtomogram averaging of cryo-electron tomograms. *J Struct Biol* 197(2):135-144.
160. Conner JG, Teschler JK, Jones CJ, Yildiz FH (2016) Staying alive: *Vibrio cholerae*'s cycle of environmental survival, transmission, and dissemination. *Microbiol Spectr* 4(2):10.
161. Lutz C, Erken M, Noorian P, Sun SY, McDougald D (2013) Environmental reservoirs and mechanisms of persistence of *Vibrio cholerae*. *Front Microbiol* 4:375.
162. Meibom KL, Li XBB, Nielsen AT, Wu CY, Roseman S, Schoolnik GK (2004) The *Vibrio cholerae* chitin utilization program. *P Natl Acad Sci USA* 101(8):2524-2529.
163. Kirn TJ, Jude BA, Taylor RK (2005) A colonization factor links *Vibrio cholerae* environmental survival and human infection. *Nature* 438(7069):863-866.
164. Costerton JW, Lewandowski Z, Caldwell DE, Korber DR, Lappinscott HM (1995) Microbial biofilms. *Annu Rev Microbiol* 49:711-745.
165. Hall-Stoodley L, Costerton JW, Stoodley P (2004) Bacterial biofilms: From the natural environment to infectious diseases. *Nat Rev Microbiol* 2(2):95-108.
166. Kamp HD, Patimalla-Dipali B, Lazinski DW, Wallace-Gadsden F, Camilli A (2013) Gene fitness landscapes of *Vibrio cholerae* at important stages of its life cycle. *Plos Pathog* 9(12):e1003800.

REFERENCES

167. Butler SM, Camilli A (2004) Both chemotaxis and net motility greatly influence the infectivity of *Vibrio cholerae*. *Proc Natl Acad Sci USA* 101(14):5018-5023.
168. Lee SH, Butler SM, Camilli A (2001) Selection for *in vivo* regulators of bacterial virulence. *Proc Natl Acad Sci USA* 98(12):6889-6894.
169. O'Toole R, Milton DL, Wolf-Watz H (1996) Chemotactic motility is required for invasion of the host by the fish pathogen *Vibrio anguillarum*. *Mol Microbiol* 19(3):625-637.
170. Butler SM, Camilli A (2005) Going against the grain: chemotaxis and infection in *Vibrio cholerae*. *Nat Rev Microbiol* 3(8):611-620.
171. Freter R, O'Brien PCM (1981) Role of chemotaxis in the association of motile bacteria with intestinal-mucosa: Chemotactic responses of *Vibrio Cholerae* and description of motile non-chemotactic mutants. *Infect Immun* 34(1):215-221.
172. Larsen MH, Larsen JL, Olsen JE (2001) Chemotaxis of *Vibrio anguillarum* to fish mucus: role of the origin of the fish mucus, the fish species and the serogroup of the pathogen. *FEMS Microbiol Ecol* 38(1):77-80.
173. Heidelberg JF, Eisen JA, Nelson WC, Clayton RA, Gwinn ML, Dodson RJ, Haft DH, Hickey EK, Peterson JD, Umayam L, Gill SR, Nelson KE, Read TD, Tettelin H, Richardson D, Ermolaeva MD, Vamathevan J, Bass S, Qin HY, Dragoi I, Sellers P, McDonald L, Utterback T, Fleishmann RD, Nierman WC, White O, Salzberg SL, Smith HO, Colwell RR, Mekalanos JJ, Venter JC, Fraser CM (2000) DNA sequence of both chromosomes of the cholera pathogen *Vibrio cholerae*. *Nature* 406(6795):477-483.
174. Hyakutake A, Homma M, Austin MJ, Boin MA, Hase CC, Kawagishi I (2005) Only one of the five CheY homologs in *Vibrio cholerae* directly switches flagellar rotation. *J Bacteriol* 187(24):8403-8410.
175. Galli E, Poidevin M, Le Bars R, Desfontaines JM, Muresan L, Paly E, Yamaichi Y, Barre FX (2016) Cell division licensing in the multi-chromosomal *Vibrio cholerae* bacterium. *Nat Microbiol* 1(9):16094.
176. Deboer PAJ, Crossley RE, Rothfield LI (1989) A division inhibitor and a topological specificity factor coded for by the minicell locus determine proper placement of the division septum in *Escherichia Coli*. *Cell* 56(4):641-649.
177. Burt A, Cassidy CK, Ames P, Bacia-Verloop M, Baulard M, Huard K, Luthey-Schulten Z, Desfosses A, Stansfeld PJ, Margolin W (2020) Complete structure of the chemosensory array core signalling unit in an *E. coli* minicell strain. *Nat Commun* 11(1):1-9.
178. Schorb M, Haberbosch I, Hagen WJH, Schwab Y, Mastronarde DN (2019) Software tools for automated transmission electron microscopy. *Nat Methods* 16(6):471-477.
179. Kremer JR, Mastronarde DN, McIntosh JR (1996) Computer visualization of three-dimensional image data using IMOD. *J Struct Biol* 116(1):71-76.
180. Castano-Diez D (2017) The Dynamo package for tomography and

- subtomogram averaging: components for MATLAB, GPU computing and EC2 Amazon Web Services. *Acta Crystallogr D Struct Biol* 73(Pt 6):478-487.
181. Falke JJ, Piasta KN (2014) Architecture and signal transduction mechanism of the bacterial chemosensory array: progress, controversies, and challenges. *Curr Opin Struct Biol* 29:85-94.
 182. Frank V, Pinas GE, Cohen H, Parkinson JS, Vaknin A (2016) Networked chemoreceptors benefit bacterial chemotaxis performance. *mBio* 7(6):e01824-16.
 183. Sourjik V, Wingreen NS (2012) Responding to chemical gradients: bacterial chemotaxis. *Curr Opin Cell Biol* 24(2):262-268.
 184. Ames P, Studdert CA, Reiser RH, Parkinson JS (2002) Collaborative signaling by mixed chemoreceptor teams in *Escherichia coli*. *Proc Natl Acad Sci USA* 99(10):7060-7065.
 185. Sourjik V, Berg HC (2004) Functional interactions between receptors in bacterial chemotaxis. *Nature* 428(6981):437-441.
 186. Kitanovic S, Ames P, Parkinson JS (2015) A trigger residue for transmembrane signaling in the *Escherichia coli* serine chemoreceptor. *J Bacteriol* 197(15):2568-2579.
 187. Kitanovic S, Ames P, Parkinson JS (2011) Mutational analysis of the control cable that mediates transmembrane signaling in the *Escherichia coli* serine chemoreceptor. *J Bacteriol* 193(19):5062-5072.
 188. Ames P, Zhou Q, Parkinson JS (2014) HAMP domain structural determinants for signalling and sensory adaptation in Tsr, the *Escherichia coli* serine chemoreceptor. *Mol Microbiol* 91(5):875-886.
 189. Coleman MD, Bass RB, Mehan RS, Falke JJ (2005) Conserved glycine residues in the cytoplasmic domain of the aspartate receptor play essential roles in kinase coupling and on-off switching. *Biochemistry* 44(21):7687-7695.
 190. Akkaladevi N, Bunyak F, Stalla D, White TA, Hazelbauer GL (2018) Flexible hinges in bacterial chemoreceptors. *J Bacteriol* 200(5):e00593-17.
 191. Pedetta A, Parkinson JS, Studdert CA (2014) Signalling-dependent interactions between the kinase-coupling protein CheW and chemoreceptors in living cells. *Mol Microbiol* 93(6):1144-1155.
 192. Vu A, Wang XQ, Zhou HJ, Dahlquist FW (2012) The receptor-CheW binding interface in bacterial chemotaxis. *J Mol Biol* 415(4):759-767.
 193. Han XS, Parkinson JS (2014) An unorthodox sensory adaptation site in the *Escherichia coli* serine chemoreceptor. *J Bacteriol* 196(3):641-649.
 194. Tajima H, Imada K, Sakuma M, Hattori F, Nara T, Kamo N, Homma M, Kawagishi I (2011) Ligand specificity determined by differentially arranged common ligand-binding residues in bacterial amino acid chemoreceptors Tsr and Tar. *J Biol Chem* 286(49):42200-42210.

REFERENCES

195. Ferris HU, Zeth K, Hulko M, Dunin-Horkawicz S, Lupas AN (2014) Axial helix rotation as a mechanism for signal regulation inferred from the crystallographic analysis of the *E. coli* serine chemoreceptor. *J Struct Biol* 186(3):349-356.
196. Pollard AM, Bilwes AM, Crane BR (2009) The structure of a soluble chemoreceptor suggests a mechanism for propagating conformational signals. *Biochemistry* 48(9):1936-1944.
197. Zhou Q, Ames P, Parkinson JS (2011) Biphasic control logic of HAMP domain signalling in the *Escherichia coli* serine chemoreceptor. *Mol Microbiol* 80(3):596-611.
198. Zhou Q, Ames P, Parkinson JS (2009) Mutational analyses of HAMP helices suggest a dynamic bundle model of input-output signalling in chemoreceptors. *Mol Microbiol* 73(5):801-814.
199. Swain KE, Gonzalez MA, Falke JJ (2009) Engineered socket study of signaling through a four-helix bundle: evidence for a yin-yang mechanism in the kinase control module of the aspartate receptor. *Biochemistry* 48(39):9266-9277.
200. Ortega DR, Yang C, Ames P, Baudry J, Parkinson JS, Zhulin IB (2013) A phenylalanine rotameric switch for signal-state control in bacterial chemoreceptors. *Nat Commun* 4:2881.
201. Pinas GE, DeSantis MD, Parkinson JS (2018) Noncritical signaling role of a kinase-receptor interaction surface in the *Escherichia coli* chemosensory core complex. *J Mol Biol* 430(7):1051-1064.
202. Slivka PF, Falke JJ (2012) Isolated bacterial chemosensory array possesses quasi- and ultrastable components: functional links between array stability, cooperativity, and order. *Biochemistry* 51(51):10218-10228.
203. Chevance FFV, Hughes KT (2008) Coordinating assembly of a bacterial macromolecular machine. *Nat Rev Microbiol* 6(6):455-465.
204. Briegel A, Pilhofer M, Mastronarde DN, Jensen GJ (2013) The challenge of determining handedness in electron tomography and the use of DNA origami gold nanoparticle helices as molecular standards. *J Struct Biol* 183(1):95-98.
205. Greenswag AR, Li X, Borbat PP, Samanta D, Watts KJ, Freed JH, Crane BR (2015) Preformed soluble chemoreceptor trimers that mimic cellular assembly states and activate CheA autophosphorylation. *Biochemistry* 54(22):3454-3468.
206. McGreevy R, Teo I, Singharoy A, Schulten K (2016) Advances in the molecular dynamics flexible fitting method for cryo-EM modeling. *Methods* 100:50-60.
207. Strelkov SV, Burkhard P (2002) Analysis of alpha-helical coiled coils with the program TWISTER reveals a structural mechanism for stutter compensation. *J Struct Biol* 137(1-2):54-64.
208. Starrett DJ, Falke JJ (2005) Adaptation mechanism of the aspartate receptor: electrostatics of the adaptation subdomain play a key role in modulating kinase activity. *Biochemistry* 44(5):1550-1560.
209. Pedetta A, Massazza DA, Herrera Seitz MK, Studdert CA (2017) Mutational

- replacements at the “glycine hinge” of the *Escherichia coli* chemoreceptor Tsr support a signaling role for the C-Helix residue. *Biochemistry* 56(29):3850-3862.
210. Hall BA, Armitage JP, Sansom MS (2012) Mechanism of bacterial signal transduction revealed by molecular dynamics of Tsr dimers and trimers of dimers in lipid vesicles. *PLoS Comput Biol* 8(9):e1002685.
 211. Wang X, Wu C, Vu A, Shea JE, Dahlquist FW (2012) Computational and experimental analyses reveal the essential roles of interdomain linkers in the biological function of chemotaxis histidine kinase CheA. *J Am Chem Soc* 134(39):16107-16110.
 212. Wang XQ, Vallurupalli P, Vu A, Lee K, Sun S, Bai WJ, Wu C, Zhou HJ, Shea JE, Kay LE, Dahlquist FW (2014) The linker between the dimerization and catalytic domains of the CheA histidine kinase propagates changes in structure and dynamics that are important for enzymatic activity. *Biochemistry* 53(5):855-861.
 213. Ding XY, He Q, Shen FL, Dahlquist FW, Wang XQ (2018) Regulatory role of an interdomain linker in the bacterial chemotaxis histidine kinase CheA. *J Bacteriol* 200(10).
 214. Parkinson JS, Houts SE (1982) Isolation and behavior of *Escherichia coli* deletion mutants lacking chemotaxis functions. *J Bacteriol* 151(1):106-113.
 215. Zheng SQ, Kesztelyi B, Branlund E, Lyle JM, Braunfeld MB, Sedat JW, Agard DA (2007) UCSF tomography: an integrated software suite for real-time electron microscopic tomographic data collection, alignment, and reconstruction. *J Struct Biol* 157(1):138-147.
 216. Mastronarde DN (2008) Correction for non-perpendicularity of beam and tilt axis in tomographic reconstructions with the IMOD package. *J Microsc* 230(Pt 2):212-217.
 217. Tang G, Peng L, Baldwin PR, Mann DS, Jiang W, Rees I, Ludtke SJ (2007) EMAN2: An extensible image processing suite for electron microscopy. *J Struct Biol* 157(1):38-46.
 218. Goddard TD, Huang CC, Ferrin TE (2007) Visualizing density maps with UCSF Chimera. *J Struct Biol* 157(1):281-287.
 219. Goddard TD, Huang CC, Ferrin TE (2005) Software extensions to UCSF Chimera for interactive visualization of large molecular assemblies. *Structure* 13(3):473-482.
 220. Pettersen EF, Goddard TD, Huang CC, Couch GS, Greenblatt DM, Meng EC, Ferrin TE (2004) UCSF Chimera--a visualization system for exploratory research and analysis. *J Comput Chem* 25(13):1605-1612.
 221. Phillips JC, Braun R, Wang W, Gumbart J, Tajkhorshid E, Villa E, Chipot C, Skeel RD, Kale L, Schulten K (2005) Scalable molecular dynamics with NAMD. *J Comput Chem* 26(16):1781-1802.
 222. Huang J, MacKerell AD, Jr. (2013) CHARMM36 all-atom additive protein

REFERENCES

- force field: validation based on comparison to NMR data. *J Comput Chem* 34(25):2135-2145.
223. Gan L, Jensen GJ (2012) Electron tomography of cells. *Q Rev Biophys* 45(1):27-56.
224. Koning RI, Koster AJ (2009) Cryo-electron tomography in biology and medicine. *Ann Anat* 191(5):427-445.
225. Briegel A, Ding HJ, Li Z, Werner J, Gitai Z, Dias DP, Jensen RB, Jensen GJ (2008) Location and architecture of the *Caulobacter crescentus* chemoreceptor array. *Mol Microbiol* 69(1):30-41.
226. Fernandez-Leiro R, Scheres SHW (2016) Unravelling biological macromolecules with cryo-electron microscopy. *Nature* 537(7620):339-346.
227. Dubochet J, Adrian M, Chang J-J, Homo J-C, Lepault J, McDowell AW, Schultz P (1988) Cryo-electron microscopy of vitrified specimens. *Q Rev Biophys* 21(2):129-228.
228. Tocheva EI, Li Z, Jensen GJ (2010) Electron cryotomography. *Cold Spring Harb Perspect Biol* 2(6):a003442.
229. Radermacher M, Wagenknecht T, Verschoor A, Frank J (1986) A new 3-D reconstruction scheme applied to the 50S ribosomal subunit of *E. coli*. *J Microsc* 141(1).
230. Steven A, Belnap D (2005) Electron microscopy and image processing: an essential tool for structural analysis of macromolecules. *Curr Protoc Protein Sci*:17.12. 11-17.12. 39.
231. Frank J (1992) Principles of electron tomography. *Electron Tomography: Three-Dimensional Imaging with the Transmission Electron Microscope*, ed Frank J (Springer US, Boston, MA), pp 1-13.
232. Comolli LR, Downing KH (2005) Dose tolerance at helium and nitrogen temperatures for whole cell electron tomography. *J Struct Biol* 152(3):149-156.
233. Koster AJ, Grimm R, Typke D, Hegerl R, Stoschek A, Walz J, Baumeister W (1997) Perspectives of molecular and cellular electron tomography. *J Struct Biol* 120(3):276-308.
234. Diebold CA, Koster AJ, Koning RI (2012) Pushing the resolution limits in cryo electron tomography of biological structures. *J Microsc* 248(1):1-5.
235. Lawrence MC (1992) Least-squares method of alignment using markers. *Electron Tomography: Three-Dimensional Imaging with the Transmission Electron Microscope*, ed Frank J (Springer US, Boston, MA), pp 197-204.
236. Penczek P, Radermacher M, Frank J (1992) Three-dimensional reconstruction of single particles embedded in ice. *Ultramicroscopy* 40(1):33-53.
237. Andersen AH, Kak AC (1984) Simultaneous algebraic reconstruction technique (SART): a superior implementation of the art algorithm. *Ultrason Imaging* 6(1):81-94.

238. Fernandez JJ, Li S, Crowther RA (2006) CTF determination and correction in electron cryotomography. *Ultramicroscopy* 106(7):587-596.
239. Walz J, Typke D, Nitsch M, Koster AJ, Hegerl R, Baumeister W (1997) Electron tomography of single ice-embedded macromolecules: Three-dimensional alignment and classification. *J Struct Biol* 120(3):387-395.
240. Nicastro D, Schwartz C, Pierson J, Gaudette R, Porter ME, McIntosh JR (2006) The molecular architecture of axonemes revealed by cryoelectron tomography. *Science* 313(5789):944-948.
241. Grassucci RA, Taylor DJ, Frank J (2007) Preparation of macromolecular complexes for cryo-electron microscopy. *Nat. Protoc* 2(12):3239-3246.
242. Dobro MJ, Melanson LA, Jensen GJ, McDowell AW (2010) Chapter three: Plunge freezing for electron cryomicroscopy. *Method Enzymol* 481:63-82.
243. Iancu CV, Tivol WF, Schooler JB, Dias DP, Henderson GP, Murphy GE, Wright ER, Li Z, Yu Z, Briegel A, Gan L, He Y, Jensen GJ (2006) Electron cryotomography sample preparation using the Vitrobot. *Nat Protoc* 1(6):2813-2819.
244. Chen S, McDowell A, Dobro MJ, Briegel A, Ladinsky M, Shi J, Tocheva EI, Beeby M, Pilhofer M, Ding HJ, Li Z, Gan L, Morris DM, Jensen GJ (2010) Electron cryotomography of bacterial cells. *J Vis Exp* (39).
245. Glaeser RM (2016) How good can cryo-EM become? *Nat methods* 13(1):28-32.
246. Mastronarde DN (2005) Automated electron microscope tomography using robust prediction of specimen movements. *J Struct Biol* 152(1):36-51.
247. Nickell S, Forster F, Linaroudis A, Net WD, Beck F, Hegerl R, Baumeister W, Plitzko JM (2005) TOM software toolbox: acquisition and analysis for electron tomography. *J Struct Biol* 149(3):227-234.
248. Frank J, Radermacher M, Penczek P, Zhu J, Li Y, Ladjadj M, Leith A (1996) SPIDER and WEB: processing and visualization of images in 3D electron microscopy and related fields. *J Struct Biol* 116(1):190-199.
249. Heymann JB, Cardone G, Winkler DC, Steven AC (2008) Computational resources for cryo-electron tomography in Bsoft. *J Struct Biol* 161(3):232-242.
250. Winkler H (2007) 3D reconstruction and processing of volumetric data in cryo-electron tomography. *J Struct Biol* 157(1):126-137.
251. Briegel A, Ortega DR, Tocheva EI, Wuichet K, Li Z, Chen S, Müller A, Iancu CV, Murphy GE, Dobro MJ (2009) Universal architecture of bacterial chemoreceptor arrays. *Proc Natl Acad Sci USA* 106(40):17181-17186.
252. Oikonomou CM, Swilius MT, Briegel A, Beeby M, Yao Q, Chang YW, Jensen GJ (2016) Electron cryotomography. *Method Microbiol* 43:115-139.
253. Oikonomou CM, Jensen GJ (2017) A new view into prokaryotic cell biology from electron cryotomography. *Nat Rev Microbiol* 15(2):128.
254. Hart RG (1968) Electron microscopy of unstained biological material: Polytopic montage. *Science* 159(3822):1464-&.

REFERENCES

255. Hoppe W, Langer R, Knesch G, Poppe C (1968) Protein-kristallstrukturanalyse mit elektronenstrahlen. *Naturwissenschaften* 55:333-336.
256. De Rosier D, Klug A (1968) Reconstruction of three dimensional structures from electron micrographs. *Nature* 217(5124):130.
257. Muok AR, Briegel A, Crane BR (2019) Regulation of the chemotaxis histidine kinase CheA: A structural perspective. *Biochim Biophys Acta Biomembr* 1862(1):183030.
258. Ortega DR, Oikonomou CM, Ding HJ, Rees-Lee P, Alexandria, Jensen GJ (2019) ETDB-Caltech: A blockchain-based distributed public database for electron tomography. *PLoS One* 14(4):e0215531.
259. Rosario MML, Fredrick KL, Ordal GW, Helmann JD (1994) Chemotaxis in *Bacillus subtilis* requires either of 2 functionally redundant chew homologs. *J Bacteriol* 176(9):2736-2739.
260. Dons L, Eriksson E, Jin YX, Rottenberg ME, Kristensson K, Larsen CN, Bresciani J, Olsen JE (2004) Role of flagellin and the two-component CheA/CheY system of *Listeria monocytogenes* in host cell invasion and virulence. *Infect Immun* 72(6):3237-3244.
261. Mercogliano CP, DeRosier DJ (2007) Concatenated metallothionein as a clonable gold label for electron microscopy. *J Struct Biol* 160(1):70-82.
262. Diestra E, Fontana J, Guichard P, Marco S, Risco C (2009) Visualization of proteins in intact cells with a clonable tag for electron microscopy. *J Struct Biol* 165(3):157-168.
263. Wang Q, Mercogliano CP, Lowe J (2011) A ferritin-based label for cellular electron cryotomography. *Structure* 19(2):147-154.
264. Chang YW, Rettberg LA, Treuner-Lange A, Iwasa J, Sogaard-Andersen L, Jensen GJ (2016) Architecture of the type IVa pilus machine. *Science* 351(6278):aad2001.
265. Hu B, Lara-Tejero M, Kong Q, Galan JE, Liu J (2017) *In situ* molecular architecture of the *Salmonella* Type III secretion machine. *Cell* 168(6):1065-1074 e1010.
266. Cardozo MJ, Massazza DA, Parkinson JS, Studdert CA (2010) Disruption of chemoreceptor signalling arrays by high levels of CheW, the receptor-kinase coupling protein. *Mol Microbiol* 75(5):1171-1181.
267. Hagen WJH, Wan W, Briggs JAG (2017) Implementation of a cryo-electron tomography tilt-scheme optimized for high resolution subtomogram averaging. *J Struct Biol* 197(2):191-198.
268. Turoňová B, Hagen WJH, Obr M, Mosalaganti S, Beugelink JW, Zimmerli CE, Kräusslich H-G, Beck M (2020) Benchmarking tomographic acquisition schemes for high-resolution structural biology. *Nat Commun* 11(1):876.
269. Himes BA, Zhang PJ (2018) emClarity: software for high-resolution cryo-electron tomography and subtomogram averaging. *Nat Methods* 15(11):955.
270. Zhang P (2019) Advances in cryo-electron tomography and subtomogram

- averaging and classification. *Curr Opin Struct Biol* 58:249-258.
271. Beck M, Malmstrom JA, Lange V, Schmidt A, Deutsch EW, Aebersold R (2009) Visual proteomics of the human pathogen *Leptospira interrogans*. *Nat Methods* 6(11):817-855.
 272. Mahamid J, Pfeffer S, Schaffer M, Villa E, Danev R, Kuhn Cuellar L, Förster F, Hyman AA, Plitzko JM, Baumeister W (2016) Visualizing the molecular sociology at the HeLa cell nuclear periphery. *Science* 351(6276):969-972.
 273. Guo Q, Lehmer C, Martinez-Sanchez A, Rudack T, Beck F, Hartmann H, Perez-Berlanga M, Frotin F, Hipp MS, Hartl FU, Edbauer D, Baumeister W, Fernandez-Busnadiego R (2018) *In situ* structure of neuronal C9orf72 Poly-GA aggregates reveals proteasome recruitment. *Cell* 172(4):696-705.e12.
 274. Xu M, Singla J, Tocheva EI, Chang YW, Stevens RC, Jensen GJ, Alber F (2019) *De Novo* structural pattern mining in cellular electron cryotomograms. *Structure* 27(4):679.
 275. Kaplan M, Subramanian P, Ghosal D, Oikonomou CM, Pirbadian S, Starwalt-Lee R, Mageswaran SK, Ortega DR, Gralnick JA, El-Naggar MY, Jensen GJ (2019) *In situ* imaging of the bacterial flagellar motor disassembly and assembly processes. *EMBO J* 38:e100957.
 276. Briegel A, Ortega DR, Mann P, Kjaer A, Ringgaard S, Jensen GJ (2016) Chemotaxis cluster 1 proteins form cytoplasmic arrays in *Vibrio cholerae* and are stabilized by a double signaling domain receptor DosM. *Proc Natl Acad Sci USA* 113(37):10412-10417.
 277. Guzman LM, Belin D, Carson MJ, Beckwith J (1995) Tight regulation, modulation, and high-level expression by vectors containing the arabinose P-Bad promoter. *J Bacteriol* 177(14):4121-4130.
 278. Ortega, DR, Kjaer, A, Briegel, A (2020) The chemosensory systems of *Vibrio cholerae*. *Mol Microbiol* 00:1-10.

CURRICULUM VITAE

Wen Yang was born on 11 April 1987 in Fuzhou, the capital city of Fujian province on the southeast coast of China. In 2009, she obtained a bachelor's degree of science at Sichuan University. In 2011, she completed a Master's program in Biomedical Engineering at the University of Melbourne, Australia. From 2012 to 2016, she worked full-time as an assistant researcher under the supervision of Dr. Sarah Perrett at the Institute of Biophysics of the Chinese Academy of Science in Beijing, China. During this period, she carried out a research project characterizing a functional amyloid protein in *Streptomyces coelicolor*. This project was in collaboration with Bio21 Molecular Science & Biotechnology Institute in Melbourne, Australia and the Institute of Biology at Leiden University in Leiden, the Netherlands. The latter collaboration eventually lead her towards a PhD program at Leiden University starting in June 2016.

This thesis covers her work as a PhD candidate under the supervision of Prof. Ariane Briegel. Since February 2020, Wen has been working as a staff scientist in the Netherlands Centre of Electron Nanoscopy.

Yang W, Briegel A (2020) Diversity of bacterial chemosensory arrays. *Trends Microbiol* 28(1):68-80.

Yang W, Cassidy CK, Ames P, Diebold CA, Schulten K, Luthey-Schulten Z, Parkinson JS, Briegel A (2019) *In situ* conformational changes of the *Escherichia coli* serine chemoreceptor in different signaling states. *mBio* 10(4):e00973-19.

Yang W, Alvarado A, Glatter T, Ringgaard S, Briegel A (2018) Baseplate variability of *Vibrio cholerae* chemoreceptor arrays. *P Natl Acad Sci USA* 115(52):13365-13370.

Yang W, Briegel A (2018) Use of cryo-EM to study the structure of chemoreceptor arrays *in vivo*. *Methods Mol Biol* 1729:173-185.

Yang W, Willemse J, Sawyer EB, Lou F, Gong W, Zhang H, Gras SL, Claessen D, Perrett S (2017) The propensity of the bacterial rodlin protein RdlB to form amyloid fibrils determines its function in *Streptomyces coelicolor*. *Sci Rep* 7:42867.

Ortega DR, Yang W, Subramanian P, Mann P, Kjær A, Chen S, Watts KJ, Pirbadian S, Collins DA, Kooger R, Kalyuzhnaya MG, Ringgaard S, Briegel A, Jensen GJ (2020) Repurposing a chemosensory macromolecular machine. *Nat Commun* 11(1):2041.

Ringgaard S, Yang W, Alvarado A, Schirner K, Briegel A (2018) Chemotaxis arrays in *Vibrio* species and their intracellular positioning by the ParC/ParP system. *J Bacteriol* 200(15):e00793-00717.

Haglin ER, Yang W, Briegel A, Thompson LK (2017) His-tag-mediated dimerization of chemoreceptors leads to assembly of functional nanoarrays. *Biochemistry* 56(44):5874-5885.

Depelteau JS, Koning G, Yang W, Briegel A (2020) An economical, portable manual cryogenic plunge freezer for the preparation of vitrified biological samples for cryogenic electron microscopy. *Microsc Microanal* 26(3):413-418.

Ultee E, Schenkel F, Yang W, Brenzinger S, Depelteau JS, Briegel A (2018) An open-source storage solution for cryo-electron microscopy samples. *Microsc Microanal* 24(1):60-63.

Alvarado A, Kjær A, Yang W, Mann P, Briegel A, Waldor MK, Ringgaard S (2017) Coupling chemosensory array formation and localization. *eLife* 6:e31058.

Muok AR, Ortega DR, Kurniyati K, Yang W, Mabrouk AS, Li C, Crane BR, Briegel A

PUBLICATIONS

(2020) Spirochetes produce ordered chemoreceptor arrays of unusual composition, arrangement, and symmetry to compensate for a highly curved membrane. *bioRxiv*:2020.2003.2011.986844.

Muok AR, Chua TK, Srivastava M, Yang W, Maschmann Z, Borbat PP, Chong J, Zhang S, Freed JH, Briegel A, Crane BR (2020) Engineered chemotaxis core signaling units indicate a constrained kinase-off state. *bioRxiv*:2020.2003.2027.011866.

